CORA Cork Open Research Archive
Cartlann Taighde Oscailte Chorcaí

Title	Modelling and analysis of hydrogenated and dilute nitride semiconductors
Authors	Arkani, Reza
Publication date	2021-07-01
Original Citation	Arkani, R. 2021. Modelling and analysis of hydrogenated and dilute nitride semiconductors. PhD Thesis, University College Cork.
Type of publication	Doctoral thesis
Rights	© 2021, Reza Arkani. - https://creativecommons.org/licenses/by-nc-nd/4.0/
Download date	2026-11-07 10:34:08
Item downloaded from	https://hdl.handle.net/10468/11885



UCC
University College Cork, Ireland
Coláiste na hOllscoile Corcaigh

Modelling and Analysis of Hydrogenated and Dilute Nitride Semiconductors

Reza Arkani



Thesis submitted in partial fulfilment of the requirements
of the degree of Doctor of Philosophy

at the
Department of Physics,
University College Cork,
National University of Ireland

Supervisor: Prof. Eoin P. O'Reilly
Head of Department: Prof. John G. McInerney

July 2021

Contents

Declaration of Authorship vii

Dedication viii

Acknowledgements ix

Abstract x

List of Publications xii

1 Introduction and overview 1
- 1.1 Overview of importance of semiconductors for applications in optoelectronic devices . . . 1
- 1.2 Structure of the thesis . . . 2

2 Theoretical methodology 7
- 2.1 Electronic band structure . . . 7
- 2.2 One-band **k.p** model for zinc-blende semiconductors . . . 9
- 2.3 Elasticity and strain-induced piezoelectricity . . . 11
  - 2.3.1 Elasticity theory . . . 12
  - 2.3.2 The piezoelectric effect . . . 14
- 2.4 Electronic structure of dilute nitride semiconductors . . . 15
  - 2.4.1 Conduction band anti-crossing in dilute nitride semiconductors . . . 15
  - 2.4.2 10-band band-anticrossing Hamiltonian . . . 16
- 2.5 Spontaneous emission in a quantum well heterostructure . . . 21
- 2.6 Conclusion . . . 26

3 Design and optimisation of metamorphic InAsSb/AlInAs mid-infrared 3.3 μm quantum well light emitting diodes 27
- 3.1 Introduction and Motivation . . . 28
- 3.2 Theory and experiment for 3.3 μm structures . . . 29
  - 3.2.1 Growth and characterisation . . . 30
  - 3.2.2 Electronic and optical properties . . . 32
- 3.3 Strain-balanced structures: design procedure . . . 41
- 3.4 Optimisation of InAsSb/AlInAs quantum wells for 3.3 μm emission . . . 42
  - 3.4.1 Electronic properties . . . 44
  - 3.4.2 Optical properties . . . 46

3.5 Conclusions . . . 48

4 Design and optimisation of dilute nitride metamorphic mid-infrared quantum well light emitting diodes 51
4.1 Routes toward achieving emission beyond 4 μm . . . 52
4.2 Design procedure for strain-balanced InNAsSb/AlInAs quantum wells . . . 53
4.3 Design and optimisation of InNAsSb/AlInAs quantum wells for 4.2 μm emission 54
4.3.1 Fixed thickness, variable in-plane strain . . . 55
4.3.2 Fixed in-plane strain, variable thickness . . . 57
4.4 Possibility of using a different metamorphic buffer layer . . . 60
4.4.1 Fixed thickness, variable in-plane strain . . . 61
4.4.2 Fixed in-plane strain, variable thickness . . . 63
4.5 Design criteria for optimum quantum well light emitting diode emitting at 4.2 μm 65
4.6 Summary and conclusions . . . 66

5 Band structure engineering of type-II $GaAs_{1-x}Sb_x$/GaAs quantum rings for intermediate band solar cells 69
5.1 Intermediate band solar cells . . . 70
5.2 Eigenstates of an infinite quantum ring . . . 73
5.3 Numerical results: strain, band offsets, and carrier localisation . . . 76
5.3.1 Strained quantum ring . . . 78
5.3.2 The strain-induced piezoelectric potential . . . 80
5.3.3 Carrier localisation . . . 81
5.4 Intermediate band gap engineering in type-II quantum rings . . . 83
5.5 Summary and conclusions . . . 85

6 Electronic properties of hydrogenated InGaAsN/GaAs dilute nitride nanostructures for single photon emission 89
6.1 Introduction and motivation . . . 90
6.2 Nanostructure formation . . . 91
6.3 Finite element simulations of selective hydrogen diffusion . . . 92
6.4 Theory and experiment for InGaAsN:H quantum dots . . . 94
6.4.1 Strain distribution . . . 95
6.4.2 Band structure calculations . . . 97
6.5 Template model for single photon sources emitting at telecommunication wavelengths . . . 99
6.6 Summary and conclusions . . . 100

7 Summary, conclusions and outlook 103
7.1 Summary and conclusions . . . 103
7.2 Outlook . . . 106

A Material parameters 107
A.1 Overview of material parameters for nitrogen-free alloys . . . 107
A.2 Overview of dilute nitride material parameters . . . 109

B Short guide to running S/PHI/nX 111

Bibliography **117**

Declaration

I, Reza Arkani (student no. 115220557), hereby declare that, unless otherwise stated, this work is my own, and that it has not been submitted for another degree, either at University College Cork or elsewhere.



Signed: _____

To Elaheh, Nika, and my parents

Acknowledgements

First of all, I would like to thank the members of the Photonics Theory Group (PTG) at Tyndall National Institute, University College Cork. It has been a pleasure to work with all of them, and I have benefited from discussing aspects of my research with many of them at various stages. I wish all of them the best of luck in their future endeavours. Of my colleagues in the PTG, I would like in particular to thank two of them for their contributions to the work that appears in this thesis. I thank Dr. Christopher Broderick, with whom I collaborated on most parts of my PhD studies. I would also like to thank Dr. Stefan Schulz for introducing me to the basics of electronic band structure calculations and helping me to start working with S/PHI/nX software package. I wish Chris and Stefan all the best as they continue their research in PTG.

I thank my collaborators on the PROMIS project. I thank the European Commission (PROMIS Initiative Training Network Scholarship no. 641899) and Science Foundation Ireland (SFI; project no. 15/IA/3082) for providing the funding that supported my research.

I thank the member of my thesis committee, Dr. Aidan Quinn, for his efforts in reviewing my progress throughout my studies and for providing helpful feedback on my work at various stages. Similarly, I thank my examiners, both internal and external, for taking time out of their busy agenda to read and examine this thesis.

Thanks are also due to my family, for their support and encouragement. I thank my father, Mohammad, and my mother, Houriyeh, for always supporting me and for teaching me the value of perseverance and hard work. I thank my wife, Elaheh, for her priceless emotional support and for being there no matter what the circumstances are. Special thanks also go to my little bundle of joy, Nika, whose birth shortly before finishing my PhD studies was a big boost in my research.

Finally, I would like to express sincere thanks to my supervisor, Prof. Eoin O'Reilly, for offering me this fabulous opportunity to be able to work in such a unique scientific atmosphere. I thank him for his great support and kind advice throughout the duration of my research over the past four years. It was indeed a real privilege and an honour to work with Eoin, both directly through his exceptional scientific knowledge and indirectly through his influence. I wish him every success in his future research in PTG.

Abstract

Dilute nitride alloys, containing small fractions of nitrogen (N), have recently attracted research interest due to their potential for application in a range of semiconductor optoelectronic devices (e.g. lasers, light emitting diodes and single photon sources). Experiments have revealed that dilute nitride alloys such as $GaAs_{1-x}N_x$, in which a small fraction x of the arsenic (As) atoms in the III-V semiconductor GaAs are replaced by N, exhibit a number of unusual properties. For example, the band gap energy decreases rapidly with increasing N composition x, by up to 150 meV per % N replacing As in the alloy. This provides an electronic band structure condition which is indeed promising for the development of highly efficient and temperature stable semiconductor optoelectronic devices based on GaAs.

We develop a fundamental understanding of this unusual class of semiconductor alloys and identify general material properties which are promising for application in light sources such as light emitting diodes and single photon sources. By performing detailed **k**·**p** calculations, we investigate the electronic band structure of nitrogen-free and dilute nitride III-V semiconductors. We reinforce our theoretical investigations by comparing our calculations to the results of experimental measurements.

We first analyse the optical properties of type-I $InAs_{1-x}Sb_x/Al_yIn_{1-y}As$ quantum wells (QWs) grown on relaxed $Al_yIn_{1-y}As$ metamorphic buffer layers (MBLs) using GaAs substrates, using a theoretical model based on an eight-band **k**·**p** Hamiltonian. The theoretical calculations, which are in good agreement with experiment, identify that the observed enhancement in PL intensity with increasing wavelength is associated with the impact of compressive strain on the QW valence band structure. Via a systematic analysis of strain-balanced quantum well structures we predict that growth of narrow ($\approx$ 4-5 nm) strained wells could lead to a further doubling in optical efficiency for devices designed to emit at 3.3 μm. Analysing the properties and performance of strain-balanced structures designed to emit at longer wavelengths, we recommend the incorporation of dilute concentrations of nitrogen (N) to achieve emission beyond 4 μm. We confirm the benefits of growth on relaxed $Al_yIn_{1-y}As$ MBLs, with an Al composition $y = 12\%$ providing significantly improved band offsets and optical characterisics compared to a MBL with $y = 6\%$.

In the next part of the thesis, we investigate the design of type-II GaAsSb/GaAs quantum ring-based (QR) intermediate band solar cells. We present an analytical solution of Schrödinger's equation for a cylindrical QR of infinite potential depth to describe the evolution of the QR ground state with QR morphology, and then undertake 8-band **k**·**p** calculations for more detailed analysis. The calculated electronic properties demonstrate several benefits, including (i) large hole ionisation energies, mitigating thermionic emission from the intermediate band, and

(ii) electron-hole spatial overlaps exceeding those in conventional $GaAs_{1-x}Sb_x$/GaAs quantum dots.

Finally, we turn our attention to modelling hydrogenated InGaAsN/GaAs nanostructures for application as single photon sources at telecommunication wavelengths. The longest wavelength emission achieved to date from such structures is at 1.2 μm. By analysing their electronic band structure and comparing with existing literature data for InGaAsN/GaAs QW structures, we identify a range of QW compositions and well widths for which it should be possible to achieve hydrogenated InGaAsN/GaAs nanostructures emitting at 1.31 μm.

Publications

The following is a list of published work in which aspects of the research presented in this thesis have featured.

1. Refereed journal articles

- "Electronic properties of type-II $GaAs_{1-x}Sb_x$/GaAs quantum rings for applications in intermediate band solar cells", R.Arkani, C. A. Broderick, and E. P. O'Reilly, *Optic. and Quant. Elec.* **52(470)**, (2020).
- "Optical properties of metamorphic type-I $InAs_{1-x}Sb_x/Al_yIn_{1-y}As$ quantum wells grown on GaAs for the mid-infrared spectral range", E. Repiso, C. A. Broderick, M. De La Mata, R. Arkani, Q. Lu, A. R. Marshall, S. I. Molina, E. P. O'Reilly, P. J. Carrington, A. Krier, *Journ. of Phys. D: Appl. Phys.* **52(46)**, 465102 (2019).
- "Theory and design of type-I In(N)AsSb/AlInAs metamorphic quantum wells for applications in mid-infrared light-emitting diodes", R.Arkani, C. A. Broderick, and E. P. O'Reilly, (under preparation).

2. Book chapter

- "Mid-infrared Optoelectronics, Materials, Devices, and Applications" 1st Edition, chapter 2, pp. 59-90, ed. Eric Tournié and Laurent Cerutti, A. Krier, E. Repiso, P. J. Carrington, A. R. Marshall, L.Qi, S. E. Krier, K. J. Lulla, M. Steer, C. MacGregor, R. Arkani, C.A. Broderick, E. P. O'Reilly, M. Sorel, S. I. Molina, M. De La Mata, *Woodhead Publishing* (2019) ISBN: 9780081027097 eBook ISBN: 9780081027387.

3. Conference proceedings

- "Computational design of metamorphic In (N) AsSb mid-infrared light-emitting diodes", R. Arkani, C. A. Broderick, and E. P. O'Reilly, in *Proceedings of the IEEE 18th International Conference on Nanotechnology* (IEEE-NANO), Cork, Ireland (2018).
- "Design of 3.3 and 4.2 μm mid-infrared metamorphic quantum well light-emitting diodes", R. Arkani, C. A. Broderick, and E. P. O'Reilly, in *Proceedings of the International Conference on Numerical Simulation of Optoelectronic Devices* (NUSOD), Hong Kong, China (2018).

- "Band structure engineering of type-II GaSb/GaAs quantum rings for intermediate band solar cells", R. Arkani, C. A. Broderick, and E. P. O'Reilly, in *Proceedings of the International Conference on Numerical Simulation of Optoelectronic Devices* (NUSOD), Ottawa, Canada (2019).

4. Conference talks

During the course of my doctoral research I have personally presented the following conference talks:

- "Design of 3.3 and 4.2 μm mid-infrared metamorphic quantum well light-emitting diodes", R. Arkani, C. A. Broderick, and E. P. O'Reilly, in *the International Conference on Numerical Simulation of Optoelectronic Devices* (NUSOD), Hong Kong, China (2018).
- "Computational design of metamorphic In (N) AsSb mid-infrared light-emitting diodes", R. Arkani, C. A. Broderick, and E. P. O'Reilly, in *the IEEE 18th International Conference on Nanotechnology* (IEEE-NANO), Cork, Ireland (2018).
- "Theory and Design of Metamorphic Quantum Well Light Emitting Diodes for Mid-Infrared Applications", R. Arkani, C. A. Broderick, and E. P. O'Reilly, in *Photonics by the Lake*, Windermere, England (2018).
- "Theory of strain-balanced In(N)AsSb/AlInAs metamorphic quantum wells for mid-infrared applications", R. Arkani, C. A. Broderick, E. Repiso, P. J. Carrington, A. Krier, and E. P. O'Reilly, in *Semiconductors and Integrated Optoelectronics* (SIOE), Cardiff, Wales (2018).

In addition to these talks I have also contributed to, and have had aspects of my work presented in, the following conference talks, which were presented by my colleagues and collaborators:

- "Band structure engineering of type-II GaSb/GaAs quantum rings for intermediate band solar cells", R. Arkani, C. A. Broderick, and E. P. O'Reilly, in *the International Conference on Numerical Simulation of Optoelectronic Devices* (NUSOD), Ottawa, Canada (2019).
- "Design of metamorphic In(N)AsSb/AlInAs mid-infrared light emitting diodes", C. A. Broderick, R. Arkani, E. Repiso, P. J. Carrington, A. Krier, and E. P. O'Reilly, in *Institute of Physics* (IOP Photon), Birmingham, England (2018).
- "Efficient mid-infrared electroluminescence from Sb based quantum well light emitting diodes grown on GaAs substrates", A. Krier, E. Repiso,P. J. Carrington, K. J. Lulla, A. R.

J. Marshall, L. Qi, M. Steer, C. MacGregor, C. A. Broderick, R. Arkani, E. P. O'Reilly, M. Sorel, S. I. Molina, and M. De La Mata, and A. Krier,, in *The 14th International Conference on Mid-IR Optoelectronics: Materials and Devices* (MIOMD) (2018).

- "Optical properties of type-II GaSb/GaAs quantum rings", S. Gandan, D. M. Cardenes, R. Arkani, J. S. D. Morales, A. Marshall, J. P. Carrington, C. A. Broderick, A. Krier, E. P. O'Reilly, and T. J Ochalski, in *Photonics Ireland*, Cork, Ireland (2018).

- "GaAs-based metamorphic quantum well light emitting diodes for the mid-infrared spectral range", E. Repiso, C. A. Broderick, M. De La Mata, R. Arkani, Q. Lu, A. R. J. Marshall, S. I. Molina, E. P. O'Reilly, P. J. Carrington, and A. Krier, in *Photonics by the Lake*, Windermere, England (2018).

- "InAsSb/InAlAs quantum wells on GaAs substrates for the mid-infrared spectral range", E. Repiso, C. A. Broderick, M. De La Mata, R. Arkani, Q. Lu, A. R. J. Marshall, S. I. Molina, E. P. O'Reilly, P. J. Carrington, and A. Krier, in *Compound Semiconductors Week* (CSW), Boston, United States of America (2018).

- "Design and optimisation of GaAs-based metamorphic heterostructures for applications in mid-infrared light-emitting diodes and semiconductor lasers", C. A. Broderick, R. Arkani, and E. P. O'Reilly, in *Photonics West*, San Francisco, United States of America (2020), acepted for oral presentation.

5. Conference posters

During the course of my doctoral research I have personally presented the following conference poster:

- "Theory and design of metamorphic quantum well light emitting diodes operating at mid-infrared wavelengths", R. Arkani, C. A. Broderick, and E. P. O'Reilly, in *Photonics Ireland*, Cork, Ireland (2018).

In addition to these posters I have also contributed to, and have had aspects of my work presented in, the following conference poster, which was presented by my colleagues and collaborators:

- "InAsSb/AlInAs metamorphic heterostructures on GaAs: Designing Quantum Wells for Mid-infrared Applications", R. Arkani, C. A. Broderick, S. Schulz, and E. P. O'Reilly, *Photonics Ireland*, Galway, Ireland (2017).

Chapter 1

Introduction and overview

In this introductory chapter we begin with Section 1.1, where we present the motivation for the research in this thesis. Here we include an overview of the progress made in the development of semiconductors for applications in optoelectronic devices. Then in Sec. 1.2 we outline the structure of this thesis.

1.1 Overview of importance of semiconductors for applications in optoelectronic devices

According to the general theory of photon-electron interactions, semiconductors absorb and emit photons by undergoing transitions between different allowed energy levels [1]. The use of semiconductors as the most technologically important materials in widespread use is an evidence for the reliability of using these materials in optoelectronic devices. Modern computers with their microprocessors constituted mainly of silicon, and using light (e.g. laser emitters) produced by the semiconductor compounds based on GaAs and GaN for reading and recording of data onto CDs, DVDs, and Blu-Rays are only two examples of the importance of semiconductor materials in optoelectronics. The huge impact of optoelectronic devices on human society is a testament to the power of scientific research in this era [2–4].

Our fundamental understanding of the electronic band structure of semiconductor materials along with the precision with which semiconductor structures can now be formed using epitaxial growth techniques have made groundbreaking developments. This fundamental understanding, combined with advanced experimental techniques, has driven worldwide research efforts to engineer the electronic band structure of semiconductor materials, including the use of alloys, heterostructures, quantum confinement, and strain [5–7].

When two semiconductors are joined – forming a heterostructure – it is not clear in advance how the different bands in the two materials will line up in energy with one another, and there remain materials for which the offset is still uncertain. Heterostructures in general have many uses. They can be used for advanced electronic devices (e.g. resonant tunneling devices, modulation-doped field-effect transistors, heterojunction bipolar transistors [8, 9]), optical components (e.g. waveguides, mirrors, microresonators [1, 10]), and optoelectronic devices and structures (e.g. laser diodes, photodetectors, quantum well and superlattice optical and optoelectronic devices [1, 11–14]). Although heterostructures may be useful in electronics, they are crucial in many optoelectronic devices (e.g. lasers [15, 16]). Their most important technological aspect is indeed that they can be used for all of these electronic, optical, and optoelectronic purposes, and hence may allow the integration of all of these [7].

Using different semiconductor materials in heterostructures increases their versatility and enables tunability of their electronic and optical properties. A basic, but very important class of semiconductor heterostructures is a quantum well (QW), which is indeed the backbone of modern optoelectronics. QW structures consist of a thin layer of one semiconductor compound sandwiched between thicker layers of another. Typical QW thicknesses are very small (only a few nanometers), with their physical properties depending very sensitively on the layer thickness. By confining charge carriers on these length scales, one enters the quantum mechanical regime. This link between quantum mechanics and real-world observable properties, e.g. emission wavelength, provides a fascinating and important topic not only for basic scientific research but also for designing novel and energy-efficient devices [7, 15].

Quantum dots (QDs) – as heterostructures with confinement in three directions – are tiny semiconductor particles (a few nanometres in size) having optical and electronic properties that differ from larger particles due to quantum mechanical confinement effects [17]. Over the last two decades semiconductor QD structures have attracted considerable research interest due to a variety of reasons [18–21]. Semiconductor QDs are fascinating physical subjects exhibiting electronic properties close to hydrogen in a dielectric cage, thus merging semiconductor physics with atomic physics. Their electronic properties are strongly geometry dependent. Varying QD size, shape and composition are attractive in order to vary their electronic and optical properties and performance, opening a fascinating window towards designing novel and efficient optoelectronic devices [18–20].

1.2 Structure of the thesis

The research outlined in this thesis can be divided into two main parts. In the first part of the research, presented in Chapters 3 and 4, we perform an analysis and design of QW-based In(N)AsSb/AlInAs light emitting diode (LED) structures grown on a metamorphic buffer layer

(MBL) to emit at mid-infrared wavelength region. In the second part of the research, presented in Chapters 5 and 6, we turn our attention to more complex semiconductor heterostructures. First, in Chapter 5, we analyse the electronic band structure of GaAsSb/GaAs quantum ring (QR) structures in order to design efficient intermediate band solar cells (IBSCs). Then, in Chapter 6, we study the electronic band structure of hydrogenated InGaAsN QD-based heterostructures for application as single photon emitters operating at the telecommunication wavelength $\lambda \approx 1.31$ μm.

We begin in Chapter 2 by presenting the theoretical methods we use to calculate the electronic and optical properties of zinc-blende semiconductors and heterostructures. We review the theory of electronic band structure in a solid by first solving a one-dimensional Schrödinger equation for a simple one-electron system with a periodic potential. Then we study the one-band **k.p** model for zinc-blende semiconductors, defined using Bloch's theorem. We proceed to elasticity and piezoelectricity theory in crystals, where we overview the general intrinsic strain field in a heterostructure and the resultant built-in potential due to the piezoelectric effect. We then review the conduction band anti-crossing in dilute nitride semiconductors. We show that the introduction of a resonant nitrogen level in these materials leads to an anticrossing interaction with the host matrix conduction band edge and a resultant reduction in energy gap. We describe a 10-band band-anticrossing Hamiltonian – including the effect of strain and built-in piezoelectric potential – to investigate the electronic band structure of III-V dilute nitride semiconductors. Finally, we present a model to calculate the spontaneous emission rate and radiative current density in QW LED structures, prior to using the model in Chapters 3 and 4.

In Chapter 3 we investigate the electronic and optical properties of nitrogen-free InAsSb/AlInAs QW-based LED structures grown on an AlInAs MBL with the aim of designing efficient strain-balanced QW LED structures emitting at 3.3 μm. We begin by presenting an introduction and a review of past related works. We benchmark our theoretical model versus experimental data, analysing nitrogen-free $InAs_{1-x}Sb_x/Al_{0.125}In_{0.875}As$ QW LED structures. After benchmarking our calculations against experimental data provided by University of Lancaster and University of Cadiz, and identifying suitable material parameters to use for our modelling, we investigate the electronic and optical properties of these structures. We discuss how our calculations compare to experimental photoluminescence (PL) data provided by University of Lancaster. We highlight the importance of strain-balancing in QW LED structures before explaining the design procedure we use in our specific calculations. Then we investigate the routes towards designing optimised metamorphic strain-balanced $InAs_{1-x}Sb_x/Al_yIn_{1-y}As$ QW structures in order to provide a design template for efficient QW LEDs operating at 3.3 μm. We quantify the electronic and optical properties of these structures by analysing their in-plane strain, carrier confinement factor, optical transition strength, spontaneous emission rate, and radiative current density. Finally, we compare the optical properties of these strain-balanced structures to the

existing structures grown by University of Lancaster and University of Cadiz to justify the benefits of using strain-balanced structures.

In Chapter 4 we investigate the electronic and optical properties of InNAsSb/AlInAs QW-based LED structures grown on an AlInAs MBL with the aim of designing efficient strain-balanced QW LED structures emitting at 4.2 μm. We begin by discussing the possibility of using metamorphic $InN_y(As_{1-x}Sb_x)_{1-y}/Al_zIn_{1-z}As$ QW structures to emit at $\lambda \geq 4$ μm by studying the bulk-like composition space map of this material platform. Then we present the design procedure for strain-balanced QW structures containing quaternary semiconductors to emit at a desired wavelength. We show that using quaternary alloys opens up a new degree of freedom to design QW LED structures: (i) with a fixed well width, and variable in-plane strain, and (ii) with a fixed in-plane strain, and variable well width. We design strain-balanced $InN_y(As_{1-x}Sb_x)_{1-y}/Al_zIn_{1-z}As$ QW structures grown on an $Al_{0.125}In_{0.875}As$ MBL emitting at $\lambda = 4.2$ μm. We then analyse the electronic and optical properties of these devices by analysing their compositions, band offsets, spontaneous emission spectra, and radiative recombination coefficient B. We seek the possibility of using a different MBL with reduced Al composition to investigate the effect of the MBL composition on the electronic and optical properties of $InN_y(As_{1-x}Sb_x)_{1-y}/Al_zIn_{1-z}As$ QW LED structures emitting at $\lambda = 4.2$ μm. Finally, we discuss the pros and cons of using different MBLs, and provide a design template for efficient mid-infrared QW LEDs emitting at $\lambda = 4.2$ μm.

In Chapter 5 we investigate the electronic properties of $GaAs_{1-x}Sb_x/GaAs$ QR structures for application in the design of efficient IBSCs. We begin with an introduction and an overview of past related works. Using an analytical analysis – based on a solution of the time-independent Schrödinger equation for a cylindrical QR of infinite potential depth – we highlight that the QR geometry offers significant flexibility, compared to a conventional QD geometry, to engineer the valence band structure of $GaAs_{1-x}Sb_x/GaAs$ structures for IBSC applications. Our numerical calculations – based on a multi-band $\mathbf{k}\cdot\mathbf{p}$ Hamiltonian, and including full strain and piezoelectric effects – corroborate this finding. We highlight that type-II $GaAs_{1-x}Sb_x/GaAs$ QRs are well suited to IBSC applications, not only because of their intrinsically large radiative lifetimes, but also due to their large valence band offsets, which can be expected to mitigate thermionic emission of holes from the intermediate band (IB). We undertake a numerical optimisation of the QR morphology, by varying the QR dimensions and alloy composition, to identify structures which allow to achieve optimum IB energy so as to maximise IBSC efficiency. Finally, we conclude that our results confirm the potential of $GaAs_{1-x}Sb_x/GaAs$ QR structures for IBSC applications, and provide guidelines for the growth of suitable structures for prototype IBSCs.

In Chapter 6 we perform an analysis of the electronic properties of hydrogenated InGaAsN QD-based heterostructures for application in single photon emission operating at $\lambda \approx 1.31$ μm. We begin by describing the applications and importance of single photon emitters operating

at telecommunication frequencies, and take a look at the literature to review related past works in this field. Then we give an overview of the structural properties of the existing InGaAsN:H nanostructures that were prepared by Sapienza University of Rome, and investigate the electronic properties of these structures. Having analysed the electronic structure of strained InGaAsN-based QDs, we benchmark the accuracy of our theoretical method by comparing the ground state transition energy with the measured PL energies. Having found good agreement between our theoretical model and experimental data, we evaluate the feasibility of designing single photon sources emitting at $\lambda \approx 1.31$ μm using the same material platform. We provide a design template for $In_yGa_{1-y}As_{1-x}N_x$/GaAs nanostructures emitting at $\lambda \approx 1.31$ μm by varying the material composition – x and y – and the height of the QW.

Finally, we conclude and summarise our analysis in Chapter 7, where we also discuss some directions for further research studies.

Chapter 2

Theoretical methodology

In this chapter we outline the theoretical methods we use to calculate the electronic and optical properties of zinc-blende semiconductors and heterostructures. We start by reviewing the theory of electronic band structure in a solid in Section 2.1, where we solve a one-dimensional Schrödinger equation for a simple one-electron system with a periodic potential. Then in Section 2.2 we study the one-band **k.p** model for zinc-blende semiconductors according to Bloch's theorem.

In Section 2.3 we turn our attention to the elasticity and piezoelectricity theory in crystals, where we represent a general intrinsic strain in a heterostructure and the resultant built-in potential due to the piezoelectric effect.

In Section 2.4 we review the conduction band anti-crossing in dilute nitride semiconductors. We show that the introduction of a resonant nitrogen level in these materials leads to an anticrossing interaction with the host matrix conduction band edge and a consequent reduction in energy gap. We propose a 10-band band-anticrossing Hamiltonian to investigate the electronic band structure of III-V dilute nitride semiconductors. Then, in Section 2.5 we derive a model to calculate the spontaneous emission rate and radiative current density in quantum well light emitting diodes. Finally, we conclude in Section 2.6.

2.1 Electronic band structure

We start by considering a solid with a periodic potential $V(\mathbf{r}+\mathbf{R}) = V(\mathbf{r})$, where $\mathbf{R}$ is a lattice vector. When studying the energy levels of a single electron with mass m_0 in this periodic potential, the system involving the contribution of the kinetic energy and the potential energy can be described by the one-electron Hamiltonian [7, 15]

$$H = -\frac{\hbar^2}{2m_0}\nabla^2 + V(\mathbf{r}). \tag{2.1}$$

Bloch's theorem states that the corresponding wave functions can be chosen to have the form

$$\psi_{n\mathbf{k}}(\mathbf{r}) = e^{i\mathbf{k}.\mathbf{r}} u_{n\mathbf{k}}(\mathbf{r}), \tag{2.2}$$

where $u_{n\mathbf{k}}(\mathbf{r}+\mathbf{R}) = u_{n\mathbf{k}}(\mathbf{r})$. The subscript n denotes the n-th state with wave vector $\mathbf{k}$. We can therefore write

$$\psi_{n\mathbf{k}}(\mathbf{r}+\mathbf{R}) = e^{i\mathbf{k}.\mathbf{R}} \psi_{n\mathbf{k}}(\mathbf{r}). \tag{2.3}$$

According to Bloch's theorem, we can associate a wave vector $\mathbf{k}$ with each energy state $\mathrm{E}_n(\mathbf{k})$ in a periodic solid. Thus, it is useful to display the energies $\mathrm{E}_n(\mathbf{k})$ as a function of the wave vector $\mathbf{k}$. In free space, the corresponding wave function of such a state can be expressed as a plane wave and the resulting $\mathrm{E}(\mathbf{k})$ can be described by the parabola:

$$E = \frac{\hbar^2 k^2}{2m_0}. \tag{2.4}$$

In a periodic solid, the free electron band structure is modified due to the presence of the potential $\mathrm{V}(\mathbf{r})$. Also, the wave vector $\mathbf{k}$ associated with a given energy state is no longer uniquely defined. To illustrate this in more detail, we consider a unit cell of length L as a one-dimensional periodic structure. In this case, we can write the wave function for the n-th state with wave number $\mathbf{k}$ as:

$$\psi_{nk}(x) = e^{ikx} u_{nk}(x). \tag{2.5}$$

Here we have a plane wave e^{ikx} of wave number $\mathbf{k}$. We also note that $u_{nk}(x)$ is a periodic function, with $u_{nk}(x) = u_{nk}(x+L)$. In order to show that the wave number $\mathbf{k}$ in this case is not uniquely defined, we multiply Eq. 2.2 by a plane wave with the periodicity of the lattice, $e^{i2\pi mx/L}$, and by its complex conjugate, $e^{-i2\pi mx/L}$, where m is an integer. This yields:

$$\psi_{nk}(x) = e^{i(k+2m\pi/L)x} \left(e^{-i2\pi mx/L} u_{nk}(x) \right), \tag{2.6}$$

where $e^{i(k+2m\pi/L)x}$ is a plane wave but a different one compared to the original choice. The term $e^{-i2\pi mx/L} u_{nk}(x)$ is still a periodic function with period L. Introducing the notation

$G_m = 2\pi m/L$ that we refer to as a "reciprocal lattice vector", we observe that the wave number $\mathbf{k}$ is then equivalent to the wave vector $k + G_m$ in the given 1D periodic system [7].

2.2 One-band k.p model for zinc-blende semiconductors

Due to its simplicity and flexibility, the $\mathbf{k}\cdot\mathbf{p}$ method is a popular approach to the study of the electronic and optical properties of semiconductor materials and heterostructures [22, 23]. As a starting point for the development of the $\mathbf{k}\cdot\mathbf{p}$ theory, we use Bloch's theorem to obtain the Schrödinger equation describing the cell-periodic part of the extended crystal eigenstates. Substituting Eq. (2.2) into the single particle Schrödinger equation:

$$\widehat{H}\psi_{n\mathbf{k}}(\mathbf{r}) = E_n(\mathbf{k})\psi_{n\mathbf{k}}(\mathbf{r})\,, \tag{2.7}$$

we obtain

$$\left(-\frac{\hbar^2}{2m_0}\nabla^2 + V(\mathbf{r})\right)\left(e^{i\mathbf{k}\cdot\mathbf{r}}u_{n\mathbf{k}}(\mathbf{r})\right) = E_n(\mathbf{k})\left(e^{i\mathbf{k}\cdot\mathbf{r}}u_{n\mathbf{k}}(\mathbf{r})\right)\,. \tag{2.8}$$

We are mainly interested in wave vectors $\mathbf{k}$ close to the reference wave vector $\mathbf{k}_0$. Therefore, we can rewrite Eq. (2.7) as:

$$-\frac{\hbar^2}{2m_0}\nabla^2\left(e^{i(\mathbf{k}-\mathbf{k}_0)\cdot\mathbf{r}}e^{i\mathbf{k}_0\cdot\mathbf{r}}u_{n\mathbf{k}}(\mathbf{r})\right)+V(\mathbf{r})e^{i(\mathbf{k}-\mathbf{k}_0)\cdot\mathbf{r}}e^{i\mathbf{k}_0\cdot\mathbf{r}}u_{n\mathbf{k}}(\mathbf{r}) = E_n(\mathbf{k})e^{i(\mathbf{k}-\mathbf{k}_0)\cdot\mathbf{r}}\left(e^{i\mathbf{k}_0\cdot\mathbf{r}}u_{n\mathbf{k}}(\mathbf{r})\right)\,. \tag{2.9}$$

Evaluating the Laplacian and recalling that $\mathbf{p} = -i\hbar\nabla$, we see that this is equivalent to

$$\widehat{H}(\mathbf{k})u_{n\mathbf{k}}(\mathbf{r}) = \left(E_n(\mathbf{k}) - \frac{\hbar^2(\mathbf{k}-\mathbf{k}_0)^2}{2m_0}\right)u_{n\mathbf{k}}(\mathbf{r})\,, \tag{2.10}$$

which can be regarded as the Schrödinger equation for the cell-periodic part $u_{n\mathbf{k}}(\mathbf{r})$ of the Bloch function $\psi_{n\mathbf{k}}(\mathbf{r})$. The $\mathbf{k}$-dependent Hamiltonian is given by $\widehat{H}(\mathbf{k}) = \widehat{H}_0 + \widehat{H}'(\mathbf{k})$ where

$$\widehat{H}_0 = -\frac{\hbar^2}{2m_0}\nabla^2 + V(\mathbf{r})\,, \tag{2.11}$$

$$\widehat{H}'(\mathbf{k}) = \frac{\hbar}{m_0}(\mathbf{k}-\mathbf{k}_0)\cdot\mathbf{p}\,. \tag{2.12}$$

$\widehat{H}_0$ and $\widehat{H}'(\mathbf{k})$ describe, respectively, the unperturbed crystal Hamiltonian at $\mathbf{k} = \mathbf{k}_0$ and the perturbation to $\widehat{H}_0$ at wave vector $\mathbf{k}$ (close to $\mathbf{k}_0$).

We wish to solve Eq. (2.10) perturbatively about some point $\mathbf{k}_0$ in the Brillouin zone, at which the eigenstates $u_{n\mathbf{k}_0}(\mathbf{r})$ of the crystal Hamiltonian are assumed to have known energies, $E_n(\mathbf{k}_0)$. From the perspective of optoelectronic device applications we are typically concerned only with some small subset of the electronic states at wave vectors $\mathbf{k}$ close to the energy gap at the Γ-point, since it is the electron and hole states at the band edges that largely determine the electronic and optical properties of the device [24]. In order to demonstrate the main principles of the $\mathbf{k}\cdot\mathbf{p}$ method we illustrate a 1-band model of the conduction band (CB), in the vicinity of the Γ-point ($\mathbf{k}_0 = 0$). Assuming that the eigenstates of this 1-band Hamiltonian are known, the band dispersion can be calculated to second order in $k = |\mathbf{k}|$ by treating $\widehat{H}'(\mathbf{k})$ perturbatively using the standard time-independent approach [25–27]. We can write:

$$E_n(\mathbf{k}) = E_n(0) + \frac{\hbar^2 k^2}{2m_0} + \frac{\hbar}{m_0}\mathbf{k}\cdot\mathbf{p}_{nn} + \frac{\hbar^2}{m_0^2}\sum_{j\neq n}\frac{|\mathbf{k}\cdot\mathbf{p}_{nj}|^2}{E_n(0) - E_j(0)}\,. \tag{2.13}$$

We note that $E_n(0) = E_{\mathrm{CB}}$ is the energy of the CB at the Γ-point, and n represents the CB state while all other states are labelled by j. The matrix elements $\mathbf{p}_{mn}$ of the momentum operator are defined in terms of the cell-periodic parts of the crystal eigenstates at $\mathbf{k}_0$ by

$$\mathbf{p}_{mn} \equiv \langle u_{m\mathbf{k}_0}|\,\widehat{\mathbf{p}}\,|u_{n\mathbf{k}_0}\rangle = -i\hbar\int_\Omega u^*_{m\mathbf{k}_0}(\mathbf{r})\,\nabla\,u_{n\mathbf{k}_0}(\mathbf{r})\,\mathrm{d}\mathbf{r}\,, \tag{2.14}$$

where Ω denotes integration over the volume of the primitive unit cell. The matrix elements $\mathbf{p}_{mn}$ can be assumed to be zero when $m = n$, so that the CB dispersion can be written as:

$$E_{\mathrm{CB}}(\mathbf{k}) = E_{\mathrm{CB}} + \frac{\hbar^2 k^2}{2m_0} + \frac{\hbar^2}{m_0^2}\sum_{j\neq n}\frac{|\mathbf{k}\cdot\mathbf{p}_{nj}|^2}{E_n(0) - E_j(0)}\,. \tag{2.15}$$

The band dispersion has been obtained perturbatively to second order in $|\mathbf{k} - \mathbf{k}_0|$. Therefore, $\mathbf{k}_0$ is an extremum of $E_n(\mathbf{k})$, and $E_n(\mathbf{k})$ depends quadratically on $|\mathbf{k} - \mathbf{k}_0|$ in the vicinity of $\mathbf{k}_0$. In addition, the band dispersion in (2.15) is described by the free electron dispersion (the first two terms on the right-hand side) and the effect of energetically remote states in the remaining terms (the third term on the right-hand side); which indeed distinguishes the band dispersion from that of a free electron since the contributions from energetically remote states at Γ include the effects of the periodic crystal potential $V(\mathbf{r})$ through the symmetries of the basis states $|u_{n\mathbf{k}_0}\rangle$ which determine the matrix elements $\mathbf{p}_{mn}$.

The band dispersion is generally quadratic in $|\mathbf{k}-\mathbf{k}_0|$. Hence, we can write Eq. (2.15) in an effective mass approximation by combining the individual contributions from free particle and crystal potential terms. We can write [4]

$$E_{\mathrm{CB}}(\mathbf{k}) = E_{\mathrm{CB}}(0) + \sum_{\alpha,\beta} D_{\alpha\beta} k_\alpha k_\beta \,, \tag{2.16}$$

where

$$D_{\alpha\beta} = \frac{\hbar^2}{2m_0}\left(\delta_{\alpha\beta} + \frac{2}{m_0}\sum_{j\neq n}\frac{p_{nj}^{(\alpha)} p_{jn}^{(\beta)}}{E_n(0)-E_j(0)}\right) , \tag{2.17}$$

and $\alpha,\beta = x,y,z$. Here, $p_{mn}^{(\alpha)}$ is the component of the momentum matrix element $\mathbf{p}_{mn}$ along the α-direction. The first and second terms describe free particle and remote state contributions to the band dispersion, respectively. Therefore, the components of the effective mass tensor are related directly to $D_{\alpha\beta}$ as

$$\left(\frac{1}{m^*}\right)_{\alpha\beta} \equiv \frac{\partial^2 E_{\mathrm{CB}}(\mathbf{k})}{\partial k_\alpha \partial k_\beta} = \frac{2}{\hbar^2} D_{\alpha\beta} \,, \tag{2.18}$$

and are treated as adjustable parameters in the model [4, 27]. The symmetry of the effective mass tensor is fully determined by that of the basis states $|u_{n\mathbf{k}_0}\rangle$, via the matrix elements $p_{nn'}^{(\alpha)}$ appearing in $D_{\alpha\beta}$. Equation (2.15) and subsequent equations describe how the **k.p** method can be used to derive a one-band Hamiltonian to describe the conduction band dispersion. We use multi-and **k.p** method in this thesis, as described in more detail in Sec 2.4.2. The derivation of a multi(N)-band **k.p** model closely follows the 1-band case described here, treating interactions between the N bands directly, while treating interactions with often, remote, bands in the same manner as described here for the 1-band case.

2.3 Elasticity and strain-induced piezoelectricity

A mechanical force acting on a crystal lattice changes the relative positions of the lattice points (sites) i.e. the positions of the atoms forming the crystal structure. Knowing the relative displacements of each lattice site, the state of the crystal deformation is described by strain components [6]. The physical deformation of the crystal leads to a distortion of the atomic locations, which in turn affects the energy levels of the carriers [28]. In order to describe this physical deformation of the crystals, we give an overview of elasticity theory in Section 2.3.1. We

will use elasticity theory to obtain the strain values in quantum heterostructures grown in the (001)-direction. Then, we will outline the piezoelectric effect in semiconductors in Section 2.3.2.

2.3.1 Elasticity theory

Here we provide expressions for the elastic tensor and the elastic energy in (001)-oriented zinc-blende systems. In semiconductor heterostructures, the lattice constant is position dependent. We use a continuum-based approach for calculating the strain field in semiconductor heterostructures [29]. The total elastic energy of the system is given for uniform strain in a second-order continuum elasticity formulation by:

$$F = \frac{V}{2} \sum_{i,j,k,l} C_{\mathrm{ijkl}} \epsilon_{\mathrm{ij}} \epsilon_{\mathrm{kl}}, \tag{2.19}$$

where V is the total volume of the system, ϵ_{ij} denotes the different components of the strain tensor, while C_{ijkl} are the components of the stiffness tensor. The indices i, j, k, l run over the spatial coordinates x, y, and z. Note that $\epsilon_{\mathrm{ij}}(r)$ and $C_{\mathrm{ijkl}}(r)$ are coordinate dependent for heterostructures, and that F is found by integrating over volume for non-uniform strain and/or position-dependent elasticity constants. The strain tensor components ϵ_{ij} are commonly written as [30, 31]:

$$\epsilon_{\mathrm{ij}}(r) = \epsilon^{\mathrm{u}}_{\mathrm{ij}}(r) + \epsilon^{0}_{\mathrm{ij}}(r), \tag{2.20}$$

where $\epsilon^{0}_{\mathrm{ij}}(r)$ is the local intrinsic strain and $\epsilon^{\mathrm{u}}_{\mathrm{ij}}(r)$ denotes local strain arising from the displacement field $\mathbf{u(r)}$. The local strain tensor components $\epsilon^{\mathrm{u}}_{\mathrm{ij}}(r)$ are defined by:

$$\epsilon^{\mathrm{u}}_{\mathrm{ij}}(r) = \frac{1}{2} \left(\frac{\partial u_{\mathrm{i}}(r)}{\partial x_{\mathrm{j}}} + \frac{\partial u_{\mathrm{j}}(r)}{\partial x_{\mathrm{i}}} \right). \tag{2.21}$$

For a given structure, the elastic energy F is minimised with respect to the displacement vector field $\mathbf{u}$. Once the displacement field is known at each point, the position dependent strain field can be obtained from Eq. (2.21).

In (001)-oriented zinc-blende structures we are left with only three independent elastic constants, which are given in Voigt notation as $C_{1111} = C_{11}$, $C_{1122} = C_{12}$, and $C_{1212} = C_{44}$.Therefore, the elasticity tensor $C_{(001)}$ takes the form

$$C_{(001)} = \begin{pmatrix} C_{11} & C_{12} & C_{12} & 0 & 0 & 0 \\ C_{12} & C_{11} & C_{12} & 0 & 0 & 0 \\ C_{12} & C_{12} & C_{11} & 0 & 0 & 0 \\ 0 & 0 & 0 & C_{44} & 0 & 0 \\ 0 & 0 & 0 & 0 & C_{44} & 0 \\ 0 & 0 & 0 & 0 & 0 & C_{44} \end{pmatrix}, \tag{2.22}$$

According to Eq. (2.23) the elastic energy $F^{(001)}$ in a zinc-blende structure using the standard coordinate system then reads [21]:

$$F^{(001)} = \frac{V}{2} \left[C_{11} \left(\epsilon_{11}^2 + \epsilon_{22}^2 + \epsilon_{33}^2 \right) + 2C_{12} \left(\epsilon_{11}\epsilon_{22} + \epsilon_{11}\epsilon_{33} + \epsilon_{22}\epsilon_{33} \right) + C_{44} \left(\epsilon_{12}^2 + \epsilon_{13}^2 + \epsilon_{23}^2 \right) \right], \tag{2.23}$$

while the intrinsic strain ϵ_{ij}^0 in a heterostructure is given by

$$\epsilon_{\mathrm{ij}}^0 = \delta_{\mathrm{ij}} \left[\frac{a_0 - a(r)}{a(r)} \right]. \tag{2.24}$$

Here, a_0 is the lattice constant of the barrier material. The position dependent lattice constant **a(r)** is the lattice constant of the nanostructure material if **r** lies inside the nanostructure, otherwise $a(r) = a_0$. The minimisation of the elastic energy **F**, Eq. (2.23), with respect to the displacement field **u** can be written as a set of partial differential equation as [30, 32]:

$$\frac{\delta F\left(u_x, u_y, u_z\right)}{\delta u_j} = \frac{\partial}{\partial r_i} \left(C_{ijkl} \left(\frac{\partial u_k}{\partial r_l} + \epsilon_{kl}^0 \right) \right) = 0, \quad j = x, y, z. \tag{2.25}$$

Using the generated displacements, one can obtain the strain field in Eq. (2.24) which will be used as input into the Hamiltonian which will be discussed in Sec. 2.4.2.

Eq. (2.24) is a general representation of intrinsic strain in a heterostructure, and can be simplified for QW structures grown along the (001)-direction as [6]:

$$\epsilon_{||} = \epsilon_{\mathrm{xx}} = \epsilon_{\mathrm{yy}} = \left(\frac{a_0 - a_{\mathrm{l}}}{a_{\mathrm{l}}} \right), \tag{2.26}$$

$$\epsilon_{\mathrm{zz}} = -2 \frac{C_{12}}{C_{11}} \epsilon_{||}. \tag{2.27}$$

where $a_{\rm l}$ denotes the lattice constant of the epitaxial layer grown on a substrate with the lattice constant a_0, and the value of ϵ_{zz} is determined by minimising the elastic energy expression, Eq. (2.23).

2.3.2 The piezoelectric effect

Certain types of crystal materials exhibit a behaviour such that under stress, an extra electric charge gathers on their surfaces. The effect is called 'piezoelectricity' and is defined as the generation of electric polarisation by the application of stress to a crystal lacking a centre of symmetry; the zinc-blende structure is one of the simplest examples of such a lattice. This strain-induced polarisation, referred to as the piezoelectric polarisation, is described in general by the first-order piezoelectric tensor $e_{\rm ijk}$ (linear regime) plus possible higher-order terms, e.g., quadratic contributions $B_{\rm ijklm}$, which are connected to the polarisation vector $P_{\rm pz}$ via the strain state of the system [33]:

$$P_{\rm pz,i} = \sum_{jk} e_{\rm ijk}\epsilon_{\rm jk} + \frac{1}{2}\sum_{jklm} B_{\rm ijklm}\epsilon_{\rm jk}\epsilon_{\rm lm} + ... \tag{2.28}$$

The strength of the resulting polarisation in a zinc-blende structure is described by only one parameter, e_{14}, for the linear case resulting in a polarisation $\mathbf{P}_1$, and three parameters B_{114} , B_{124} and B_{156}, for the quadratic case resulting in a polarisation $\mathbf{P}_2$. These polarisations can be calculated as

$$\mathbf{P}_1 = 2e_{14}\begin{pmatrix}\epsilon_{\rm yz}\\ \epsilon_{\rm xz}\\ \epsilon_{\rm xy}\end{pmatrix}, \tag{2.29}$$

$$\mathbf{P}_2 = 2B_{114}\begin{pmatrix}\epsilon_{\rm xx}\epsilon_{\rm yz}\\ \epsilon_{\rm yy}\epsilon_{\rm xz}\\ \epsilon_{\rm zz}\epsilon_{\rm xy}\end{pmatrix} + 2B_{124}\begin{pmatrix}\epsilon_{\rm yz}\left(\epsilon_{\rm yy}+\epsilon_{\rm zz}\right)\\ \epsilon_{\rm xz}\left(\epsilon_{\rm xx}+\epsilon_{\rm zz}\right)\\ \epsilon_{\rm xy}\left(\epsilon_{\rm xx}+\epsilon_{\rm yy}\right)\end{pmatrix} + 4B_{156}\begin{pmatrix}\epsilon_{\rm xz}\epsilon_{\rm xy}\\ \epsilon_{\rm yz}\epsilon_{\rm xy}\\ \epsilon_{\rm yz}\epsilon_{\rm xz}\end{pmatrix}. \tag{2.30}$$

The importance of second-order term $\mathbf{P}_2$ has been pointed out in Refs. [20, 34, 35] making it necessary to consider while investigating strain distribution and electronic band structure of semiconductor heterostructures. These polarisations will lead to a piezoelectric charge density, $\rho_{\rm piezo}$, which is given by [20]:

$$\rho_{\rm piezo}(r) = -\bigtriangledown.\mathbf{P}_{\rm tot}, \tag{2.31}$$

where

$$\mathbf{P}_{\text{tot}} = \mathbf{P}_1 + \mathbf{P}_2. \tag{2.32}$$

By solving Poisson's equation the resulting piezoelectric potential can be calculated, though the material dependence of the static dielectric constant, $\epsilon_{\text{s}}(r)$, should be taken into account. Therfore, we can write:

$$\rho_{\text{piezo}}(r) = \epsilon_0 \bigtriangledown . [\epsilon_{\text{s}}(r) \bigtriangledown V_{\text{p}}(r)] \ , \tag{2.33}$$

$$\Delta V_{\text{p}}(r) = \frac{\rho_{\text{piezo}}(r)}{\epsilon_0 \epsilon_{\text{s}}(r)} - \frac{1}{\epsilon_{\text{s}}(r)} \bigtriangledown V_{\text{p}}(r). \bigtriangledown \epsilon_{\text{s}}(r). \tag{2.34}$$

The first term on the right hand side of Eq. (2.34) indicates the true three-dimensional charge density, and the second term is the contribution of polarisation interface charge densities due to a discontinuous $\epsilon_{\text{s}}(r)$ across heterointerfaces.

Even though the piezoelectric potential is zero by symmetry in the heterostructures grown along the (001)-direction considered in Chapters 3 and 4, but can have an influence on carrier energies and wavefunctions in quantum dot structures such as type-II GaSb/GaAs quantum rings discussed in Chapter 5.

2.4 Electronic structure of dilute nitride semiconductors

In this section, we present a review of the theory and modeling of the electronic structure of dilute nitride alloys. We highlight key results from the literature, following a path that enables us to build towards a quantitative description of the properties of real, disordered dilute nitride alloys. The models reviewed in this section will underpin our discussions of the theory and simulation of dilute nitride materials and devices throughout the remainder of this thesis.

2.4.1 Conduction band anti-crossing in dilute nitride semiconductors

When a single N atom replaces an As atom in InAs or GaAs, it forms a resonant defect level above the conduction band edge (CBE) of the host material [36]. This defect level arises because of the large difference in electronegativity and atomic size between N and As. The band-anticrossing (BAC) model explains the extreme composition-dependent band-gap bowing observed in dilute nitride semiconductors in terms of an interaction between two levels, one

at energy E_N associated with these localised N impurity states ψ_N and the other at energy E_c associated with the extended CBE state ψ_{c0} of the host matrix, with the two states linked by a matrix element V_{Nc} describing the interaction between them [37]. The CB dispersion near the band edge in a dilute nitride semiconductor is then given in the BAC model by the lower eigenvalue of the determinant

$$\begin{vmatrix} E_N - E & V_{Nc} \\ V_{Nc} & E_c + \frac{\hbar^2 k^2}{2m_c} - E \end{vmatrix} , \tag{2.35}$$

where m_c is the band-edge effective mass of the the host matrix material, and $V_{Nc} = \beta \sqrt{x}$, the N concentration, x, and β describes the strength of the BAC interaction. From Eq. 2.35 we can obtain the CBE energy, E_-, as:

$$E_- = \frac{E_N + E_c}{2} - \sqrt{\left(\frac{E_N - E_c}{2}\right) + V_{Nc}^2} , \tag{2.36}$$

and the alloy CBE wavefunction ψ_- is given as:

$$\psi_- = \alpha_c \psi_{c0} + \alpha_N \psi_N , \tag{2.37}$$

where $\alpha_c^2 + \alpha_N^2 = 1$ [12]. A resonant feature associated with the upper eigenvalue, E_+, has also been observed in photoreflectance measurements [36], appearing in $GaAs_{1-x}N_x$ for $x >\sim 0.2$ % and remaining a relatively clear feature until $x \sim 3$ % [38]. Fig. 2.1 shows the calculated CB dispersion of $GaAs_{0.99}N_{0.01}$ using the BAC parameters $E_N = 1.63$ eV and $\beta = 2.0$ eV. The BAC interaction leads the CB to split into two separate bands E_+ and E_- leading to a downward shift of the CB minimum. Photoreflectance measurements of GaAsN quantum well samples have also shown that strong band nonparabolicity is required to account for the quantum well excited state transition energies across a wide range of samples and as a function of hydrostatic pressure [12]. Although the BAC model describes well the dispersion of the lower (E_-) band in the immediate vicinity of the Γ band edge, it should be noted that it fails to give a proper physical dispersion for this band at large wavevector $\mathbf{k}$. Nevertheless, it provides a good description of the dispersion close to the band edge for the structures of interest in Chapters 4 and 6.

2.4.2 10-band band-anticrossing Hamiltonian

Here we describe the band structure in the vicinity of the conduction and valence band edges at the Γ-point in the Brillouin zone. The 8-band $\mathbf{k}\cdot\mathbf{p}$ Hamiltonian represents the band structure

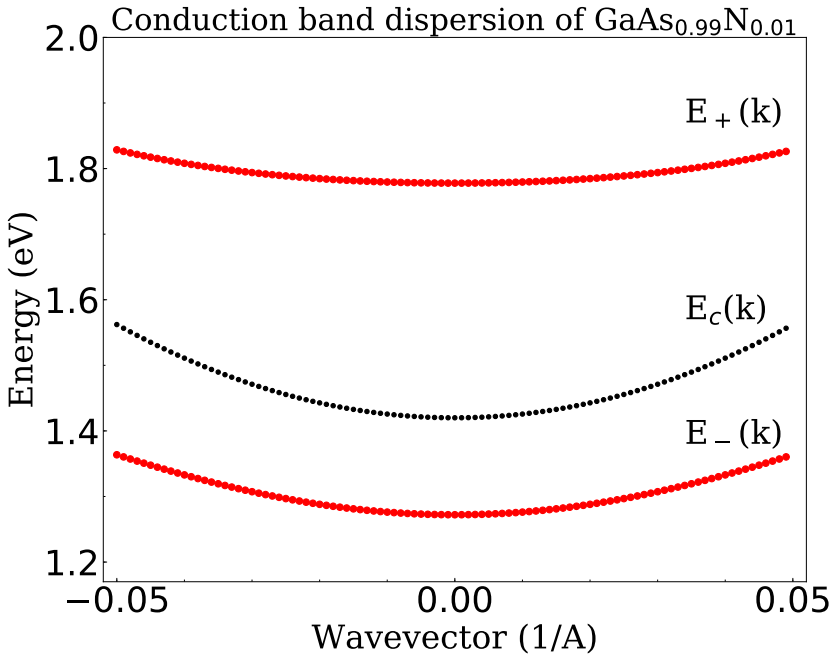


FIGURE 2.1: Calculated conduction band dispersion of $GaAs_{0.99}N_{0.01}$ using two-band BAC model. Black line indicates the conduction band dispersion of nitrogen-free host GaAs, while red lines show the conduction band dispersion of dilute nitride $GaAs_{0.99}N_{0.01}$.

of the lowest conduction band (CB), as well as the heavy-hole (HH), light-hole (LH) and spin-split-off (SO) valence bands [39–41]. This model includes the interactions between these spin-degenerate bands as outlined in Ref. [39]. Chao and Chuang have shown that disregarding the effect of SO band may result in a considerable inaccuracy in studying the band structure of zinc-blende semiconductors [42]. There are a considerable number of **k·p** models in the literature that differ from the 8-band model for the zinc blende crystal structure that we will discuss here. Refs. [22] and [23] provide a comprehensive exposition of the theory and applications of the **k·p** method.

As mentioned above, the strong interaction between the N resonant states and the CBE means that the conventional eight-band **k·p** method cannot be applied directly to dilute nitride heterostructures. Here we extend the conventional eight-band **k.p** Hamiltonian to a 10-band model to investigate the electronic structure of such alloys.

In order to describe the electronic structure of dilute nitride semiconductors, two spin-degenerate nitrogen-related bands are added to the usual two conduction and six valence bands in the conventional eight-band model. We define $\sigma = (\sigma_x, \sigma_y, \sigma_z)$ as the Pauli matrices

$$\sigma_x = \begin{pmatrix} 0 & 1 \\ 1 & 0 \end{pmatrix}, \qquad \sigma_y = \begin{pmatrix} 0 & -i \\ i & 0 \end{pmatrix}, \qquad \sigma_z = \begin{pmatrix} 1 & 0 \\ 0 & -1 \end{pmatrix}, \tag{2.38}$$

the actions of which on the eigenspinors $|\uparrow\rangle$ and $|\downarrow\rangle$ describing the z-component of the spin are given by

$$\sigma_x|\uparrow\rangle = |\downarrow\rangle\,, \qquad \sigma_x|\downarrow\rangle = |\uparrow\rangle\,, \tag{2.39}$$

$$\sigma_y|\uparrow\rangle = i|\downarrow\rangle\,, \qquad \sigma_y|\downarrow\rangle = -i|\uparrow\rangle\,, \tag{2.40}$$

$$\sigma_z|\uparrow\rangle = |\uparrow\rangle\,, \qquad \sigma_z|\downarrow\rangle = -|\downarrow\rangle\,, \tag{2.41}$$

from which we can see that the action of the σ_x and σ_y Pauli matrices is to flip the z-component of the spin [25, 26]. The zone centre eigenstates of the 10-band Hamiltonian H_k can then be written in the angular momentum Bloch basis as

$$|u_1\rangle = \left|\frac{1}{2},+\frac{1}{2}\right\rangle = |s_{\rm N};\uparrow\rangle, \tag{2.42}$$

$$|u_2\rangle = \left|\frac{1}{2},+\frac{1}{2}\right\rangle = |s_{\rm c};\uparrow\rangle, \tag{2.43}$$

$$|u_3\rangle = \left|\frac{3}{2},+\frac{3}{2}\right\rangle = \frac{i}{\sqrt{2}}|x;\uparrow\rangle - \frac{1}{\sqrt{2}}|y;\uparrow\rangle\,, \tag{2.44}$$

$$|u_4\rangle = \left|\frac{3}{2},+\frac{1}{2}\right\rangle = \frac{i}{\sqrt{6}}|x;\downarrow\rangle - \frac{1}{\sqrt{6}}|y;\downarrow\rangle - i\sqrt{\frac{2}{3}}|z;\uparrow\rangle\,, \tag{2.45}$$

$$|u_5\rangle = \left|\frac{1}{2},+\frac{1}{2}\right\rangle = \frac{i}{\sqrt{3}}|x;\downarrow\rangle - \frac{1}{\sqrt{3}}|y;\downarrow\rangle + \frac{i}{\sqrt{3}}|z;\uparrow\rangle\,. \tag{2.46}$$

The set of states $|u_6\rangle - |u_{10}\rangle$ are obtained by applying the time-reversal symmetry operator $\hat{T}_d$ = -$i\sigma_y\hat{C}\hat{J}$ for zinc-blende structures, where $\hat{C}$ is the complex conjugation operator, and $\hat{J}$ is the inversion about midpoint between nearest neighbors ($s \mapsto -s$, $p \mapsto -p$). Therefore, we can write:

$$|u_6\rangle = \left|\frac{1}{2},-\frac{1}{2}\right\rangle = -|s_{\rm N};\downarrow\rangle, \tag{2.47}$$

$$|u_7\rangle = \left|\frac{1}{2},-\frac{1}{2}\right\rangle = -|s_{\rm c};\downarrow\rangle, \tag{2.48}$$

$$|u_8\rangle = \left|\frac{3}{2},-\frac{3}{2}\right\rangle = -\frac{i}{\sqrt{2}}|x;\downarrow\rangle + \frac{1}{\sqrt{2}}|y;\downarrow\rangle\,, \tag{2.49}$$

$$|u_9\rangle = \left|\frac{3}{2},-\frac{1}{2}\right\rangle = \frac{i}{\sqrt{6}}|x;\uparrow\rangle + \frac{1}{\sqrt{6}}|y;\uparrow\rangle + i\sqrt{\frac{2}{3}}|z;\downarrow\rangle\,, \tag{2.50}$$

$$|u_{10}\rangle = \left|\frac{1}{2},-\frac{1}{2}\right\rangle = \frac{i}{\sqrt{3}}|x;\uparrow\rangle + \frac{1}{\sqrt{3}}|y;\uparrow\rangle - \frac{i}{\sqrt{3}}|z;\downarrow\rangle\,. \tag{2.51}$$

The 10-band **k.p** Hamiltonian for finite wavefunction **k** includes **k**-dependent diagonal and off-diagonal matrix elements, linking the nitrogen, conduction, and valence basis states:

$$H = \begin{pmatrix} E_{\mathrm{NB}} & V_{\mathrm{Nc}} & 0 & 0 & 0 & 0 & 0 & 0 & 0 & 0 \\ & E_{\mathrm{CB}} & -\sqrt{3}T & \sqrt{2}U & -U & 0 & 0 & 0 & -T^* & -\sqrt{2}T^* \\ & & E_{\mathrm{HH}} & \sqrt{S} & -S & 0 & 0 & 0 & -R & -\sqrt{2}R \\ & & & E_{\mathrm{LH}} & -\sqrt{2}Q & 0 & T^* & R & 0 & \sqrt{3}S \\ & & & & E_{\mathrm{SO}} & 0 & \sqrt{2}T^* & \sqrt{2}R & -\sqrt{3}S & 0 \\ & & & & & E_{\mathrm{NB}} & V_{\mathrm{Nc}} & 0 & 0 & 0 \\ & & & & & & E_{\mathrm{CB}} & -\sqrt{3}T^* & \sqrt{2}U & -U \\ & & & & & & & E_{\mathrm{HH}} & \sqrt{2}S^* & -S^* \\ & & & & & & & & E_{\mathrm{LH}} & -\sqrt{2}Q \\ & & & & & & & & & E_{\mathrm{SO}} \end{pmatrix} \begin{matrix} |u_1\rangle \\ |u_2\rangle \\ |u_3\rangle \\ |u_4\rangle \\ |u_5\rangle \\ |u_6\rangle \\ |u_7\rangle \\ |u_8\rangle \\ |u_9\rangle \\ |u_{10}\rangle \end{matrix} \tag{2.52}$$

where diagonal elements are defined as:

$$E_{\mathrm{NB}} = E_{\mathrm{N0}} + \left(\frac{\hbar^2}{2m_0}\right)\gamma_{\mathrm{N}}\left(k_x^2 + k_y^2 + k_z^2\right) + a_{\mathrm{N}}\left(\epsilon_{xx} + \epsilon_{yy} + \epsilon_{zz}\right) + V_{\mathrm{p}}, \tag{2.53}$$

$$E_{\mathrm{CB}} = E_{\mathrm{C0}} + \left(\frac{\hbar^2}{2m_0}\right)\gamma_{\mathrm{C}}\left(k_x^2 + k_y^2 + k_z^2\right) + a_{\mathrm{c}}\left(\epsilon_{xx} + \epsilon_{yy} + \epsilon_{zz}\right) + V_{\mathrm{p}}, \tag{2.54}$$

$$\begin{aligned} E_{\mathrm{HH}} = E_{\mathrm{V0}} &- \left(\frac{\hbar^2}{2m_0}\right)\left[\left(\gamma_1 + \gamma_2\right)\left(k_x^2 + k_y^2\right) + \left(\gamma_1 - 2\gamma_2\right)k_z^2\right] \\ &+ a_{\mathrm{v}}\left(\epsilon_{xx} + \epsilon_{yy} + \epsilon_{zz}\right) + \frac{b_v}{2}\left(\epsilon_{xx} + \epsilon_{yy} - 2\epsilon_{zz}\right) + V_{\mathrm{p}}, \end{aligned} \tag{2.55}$$

$$\begin{aligned} E_{\mathrm{LH}} = E_{\mathrm{V0}} &- \left(\frac{\hbar^2}{2m_0}\right)\left[\left(\gamma_1 - \gamma_2\right)\left(k_x^2 + k_y^2\right) + \left(\gamma_1 + 2\gamma_2\right)k_z^2\right] \\ &+ a_{\mathrm{v}}\left(\epsilon_{xx} + \epsilon_{yy} + \epsilon_{zz}\right) - \frac{b_v}{2}\left(\epsilon_{xx} + \epsilon_{yy} - 2\epsilon_{zz}\right) + V_{\mathrm{p}}, \end{aligned} \tag{2.56}$$

$$E_{\mathrm{SO}} = E_{\mathrm{V0}} - \Delta_{\mathrm{SO}} - \left(\frac{\hbar^2}{2m_0}\right)\gamma_1\left(k_x^2 + k_y^2 + k_z^2\right) + a_{\mathrm{v}}\left(\epsilon_{xx} + \epsilon_{yy} + \epsilon_{zz}\right) + V_{\mathrm{p}}. \tag{2.57}$$

Here, the subscripts NB, CB, HH, LH and SO stand for nitrogen resonant, conduction, heavy hole, light hole, and split-off band, respectively, and Δ_{SO} is the spin-orbital split-off energy. The unstrained nitrogen resonant (E_{N0}), conduction (E_{C0}), and valence (E_{V0}) band edges, are all aligned relative to the average valence band of the matrix material, respectively. The components of the wave vector along the crystallographic directions (100), (010) and (001) are denoted by k_x, k_y and k_z, respectively. The strain components ϵ_{xx}, ϵ_{yy} and ϵ_{zz} are calculated using equations (2.26) and (2.27), and are used to calculate the shift in band edges. a_{N} is the nitrogen resonant band hydrostatic deformation potential, a_c and a_v are the conduction

and valence band hydrostatic deformation potential of the host semiconductor, and b_v is the axial deformation potential along the (001) direction of the host material. $V_{\rm p}$ refers to the calculated built-in piezoelectric potential as outlined in 2.3.2. γ_1, γ_2 and γ_3 are modified Luttinger parameters related to the original Luttinger parameters (superscript L) and remote bands as

$$\gamma_c = \frac{1}{m_c^*} - \left(\frac{E_P}{3}\right) \times \left[\frac{2}{E_g} + \frac{1}{E_g} + \Delta_{so}\right] , \tag{2.58}$$

$$\gamma_1 = \gamma_1^L - \left(\frac{E_P}{3E_g + \Delta_{so}}\right) , \tag{2.59}$$

$$\gamma_{2,3} = \gamma_{2,3}^L - \left(\frac{E_P}{6E_g + 2\Delta_{so}}\right) , \tag{2.60}$$

where m_c^* is the electron effective mass of the semiconductor, and E_g is the band gap energy of the host material. E_P is calculated as $E_P{=}2m_0P_0^2/\hbar^2$, where P_0 is the Kane matrix element that couples the conduction band at Γ to the class A [1] valence bands. In the flat nitrogen resonant band approximation, most commonly used in the literature $\gamma_{\rm N} = 0$ [44]. The kinetic terms of the Hamiltonian are given by:

$$Q = \left(\frac{\hbar^2}{2m_0}\right)\gamma_2(k_x^2 + k_y^2 - 2k_z^2) - \frac{b_v}{2}\left(\epsilon_{xx} + \epsilon_{yy} - 2\epsilon_{zz}\right) , \tag{2.61}$$

$$R = \left(\frac{\hbar^2}{2m_0}\right)\sqrt{3}\left(\gamma_2(k_x^2 - k_y^2) - 2i\gamma_3 k_x k_y\right) - \frac{\sqrt{3}}{2}b_v(\epsilon_{xx} - \epsilon_{yy}) + id_v\epsilon_{xy} , \tag{2.62}$$

$$S = \left(\frac{\hbar^2}{2m_0}\right)\sqrt{6}\gamma_3(k_x - ik_y)k_z - \frac{d_v}{\sqrt{2}}(\epsilon_{xz} - i\epsilon_{yz}) , \tag{2.63}$$

$$T = \frac{P_0}{\sqrt{6}}\left((k_x + ik_y) + \sum_j(\epsilon_{xj} + i\epsilon_{yj})k_j\right) , \tag{2.64}$$

$$U = \frac{P_0}{\sqrt{3}}\left(k_z + \sum_j \epsilon_{zj}k_j\right) , \tag{2.65}$$

where d_v is the shear deformation potential along the (111) direction of the host matrix.

This model can be used to calculate the electronic band structure of any quantum heterostructure containing a direct-gap III-V dilute nitride semiconductor. This model can also be used to calculate the electronic band structure of conventional nitrogen-free III-V semiconductors by setting the nitrogen-related parameter β equal to zero, but an eight-band **k.p** model is more

[1] Using Löwdin's renormalisation [43], the main bands of interest are denoted as class A, and the interaction between them will be included explicitly in the Hamiltonian.

suitable for such material systems given the fact that diagonalising an 8×8 matrix is considerably easier than diagonalising a 10×10 matrix. Therefore, we will use a conventional 8-band **k.p** model to study the electronic band structure of nitrogen-free material systems throughout this thesis by simply omitting the first and fifth row and column of the Hamiltonian matrix described in Eq. (2.52).

As mentioened earlier, the **k.p** model described here makes use of Bloch's theorem which originates from crystal periodicity, due to which, **k** is a good quantum number in bulk binary systems. However, since quantum confinement breaks the translational symmetry in a heterostructure, this periodicity no longer exists in quantum heterostructures. In order to be able to use this method for describing the electronic structure of a heterostructure, we have to make changes to the developed formalism. The standard approach is to use the following substitutions when symmetry is broken in all three dimensions [6]:

$$k_x \rightarrow \hat{k_x} = -i\frac{\partial}{\partial x} \,, \tag{2.66}$$

$$k_y \rightarrow \hat{k_y} = -i\frac{\partial}{\partial y} \,, \tag{2.67}$$

$$k_z \rightarrow \hat{k_z} = -i\frac{\partial}{\partial z} \,. \tag{2.68}$$

We note that in heterostructures the material parameters become spatially dependent and vary throughout the structure. Therefore, we should be careful that operators are still Hermitian when introducing a substitution. In order to retain Hermiticity, symmetrisation of individual elements of the Hamiltonian matrix is performed as:

$$Tk_x \rightarrow \frac{1}{2}\left(T\hat{k_x} + \hat{k_x}T\right) \,, \tag{2.69}$$

$$Tk_xk_y \rightarrow \frac{1}{2}\left(\hat{k_x}T\hat{k_y} + \hat{k_y}T\hat{k_x}\right) \,, \tag{2.70}$$

where T represents any material parameter of the bulk **k.p** model. We then use the plane wave expansion method throughout this thesis to diagonalise and solve the Hamiltonian matrix as described in further detail in Refs. [23, 24, 45, 46].

2.5 Spontaneous emission in a quantum well heterostructure

Spontaneous emission in a semiconductor occurs when a photon is emitted associated with the transition of an electron from the conduction band to the valence band [15]. Hence, in

order to study spontaneous emission, we need to understand electron-photon interaction in the crystal. To examine this interaction, we represent the photon classically by an electromagnetic wave. The wave's interaction with the electron enters into the Schrödinger equation through the vector potential, which can be expressed as

$$A\left(\mathbf{r},t\right)=\frac{1}{2}\widehat{e}\left[A(\mathbf{r})e^{-i\omega t}+A^{*}(\mathbf{r})e^{i\omega t}\right]\,, \tag{2.71}$$

where $\widehat{e}$ is the polarisation vector in the direction of A, and ω is the angular frequency of the photon. The modified Schrödinger equation then reads

$$H \;=\; H_0+\left[H'(\mathbf{r})e^{-i\omega t}+h.c.\right]\,, H'(\mathbf{r})\equiv\frac{2}{m_0}A(\mathbf{r})\widehat{\mathbf{e}}.\mathbf{p}\,. \tag{2.72}$$

where the $h.c$ stands for Hermitian conjugate, and simply means that we take the complex conjugate of all terms except the Hamiltonian operator $\mathbf{p}$. The transition rate then can be derived according to Fermi's golden rule as described in quantum mechanics textbooks [15, 25, 26]:

$$W_{e\rightarrow h}=\frac{2\pi}{\hbar}\left(H'_{eh}\right)^{2}\delta\left(E_e-E_h-\hbar\omega\right)\,, \tag{2.73}$$

$$H'_{eh}=\int_V\psi_h^{*}H'(\mathbf{r})\psi_e d^3\mathbf{r}\,, \tag{2.74}$$

where V is the volume of the crystal, and

$$E_{e,h}=E_{c,v}\pm\frac{\hbar^2k^2}{2m_{c,v}}\,, \tag{2.75}$$

in which E_c and E_v, respectively, denote the conduction and valence band edge energy, and electron and hole effective masses are denoted as m_c and m_v, respectively. The delta function (which has units of energy) in Eq. (2.73) indicates that the difference between the initial and final energy (E_e-E_h) of the electron must be equal to the energy $\hbar\omega$ of the photon associated with the transition. Using an arbitrary set of expansion coefficients, A(k), one can express a spatially localised wavefunction as the sought-after envelope function approximation [45]

$$\psi=\int A(k)e^{ik.\mathbf{r}}u(k,\mathbf{r})d^3k\approx u(0,\mathbf{r})\int A(k)e^{ik.\mathbf{r}}d^3k\equiv F(\mathbf{r})u(\mathbf{r})\,. \tag{2.76}$$

We assume here that, within a given energy band, the Bloch function is a weak function of $\mathbf{k}$ (at least in the proximity of the band edge) and can thus be approximately represented by the band edge ($\mathbf{k} = 0$) Bloch function, $u(0, \mathbf{r}) \equiv u(\mathbf{r})$, i.e. we use a 1-band Hamiltonian for each band. Therefore, we can pull it out of the expansion and define an envelope function $F(\mathbf{r})$, whose Fourier spectrum is made up of the plane wave components. With this assumption, the generalised approximate solutions in a given energy band consist of the band edge Bloch function, multiplied by a slowly varying envelope function [15, 41].

Using the electron and hole wavefunctions defined in Eq. (2.76), the perturbation term defined in Eq. (2.72), and the fact that Bloch functions u repeat themselves in each unit cell, we can write Eq. (2.74) as

$$H'_{eh} = \frac{e}{2m_0} \langle u_v \mid \widehat{\mathbf{e}}.\mathbf{p} \mid u_c \rangle \int_V F_h^* A(\mathbf{r}) F_e d^3\mathbf{r} \,. \tag{2.77}$$

This envelope function overlap integral in Eq.(2.77) is general and can be applied to different types of problems. However, it is important to note that this rule only applies to transitions between two plane wave states (band-to-band transition). When the dimensions of the well are much smaller than the wavelength of light, the vector potential can be taken as a constant, A_0, across the region of the well. This case involves transitions between two localised states, both bound to a quantum well along the z direction. Therefore, we can write

$$\int_V F_h^* A(\mathbf{r}) F_e d^3\mathbf{r} \approx A_0 \int F_h^* F_e dz \equiv A_0 \langle F_h \mid F_e \rangle \,. \tag{2.78}$$

Substituting Eq. (2.78) into Eq. (2.77), we can write:

$$H'_{eh} = \left(\frac{eA_0}{2m_0} \right) \mid M_T \mid^2 , \tag{2.79}$$

where the transition matrix elements $\mid M_T \mid$ are defined as

$$\mid M_T \mid^2 \equiv \mid \langle u_v \mid \widehat{\mathbf{e}}.\mathbf{p} \mid u_c \rangle^2 \mid \langle F_h \mid F_e \rangle \mid^2 , \tag{2.80}$$

that arises in the study of the optical properties of quantum wells. Specifically, the probability of the occurrence of an interband optical transition between a conduction state and a valence state is proportional to the squared modulus of the momentum matrix element between them. For this reason, the momentum matrix element between a pair of eigenstates provides a useful measure of the optical transition strength. To include the spin degeneracy in evaluation of

$\mid M_T \mid^2$, we should sum over $u_c \to u_v$, $u_c \to \overline{u}_v$, $\overline{u}_c \to u_v$ and $\overline{u}_c \to \overline{u}_v$ transitions. Hence, for the transitions between two bulk plane wave states we can write[2]:

$$\mid M_T \mid^2 = \sum_{u_c,\overline{u}_c} \sum_{u_v,\overline{u}_v} \langle u_v \mid \widehat{\mathbf{e}}.\mathbf{p} \mid u_c \rangle^2 \ . \tag{2.81}$$

Using Szmulowicz formalism [45] we can write the momentum matrix element $P_{n_c,n_v}\left(\mathbf{k}_{\parallel}\right)$ in a QW heterostructure as:

$$P_{n_c,n_v}\left(\mathbf{k}_{\parallel}\right) = \frac{m_0}{\hbar} \sum_{b,b'} \sum_{m,m'} a^*_{n_v b' m'}\left(\mathbf{k}_{\parallel}\right) a_{n_c b m}\left(\mathbf{k}_{\parallel}\right) \left(\frac{\partial \widehat{H}_{b'b}}{\partial \mathbf{k}_{\parallel}} \cdot \widehat{e} \right)_{m'm} , \tag{2.82}$$

where n_c (n_v) indexes conduction (valence) band subbands, and $a_{nbm}\left(\mathbf{k}_{\parallel}\right)$ denotes the Fourier coefficients of the envelope functions. Eq. (2.82) represents an analytical expression to calculate the momentum matrix elements between QW eigenstates. In order to calculate the spontaneous emission rate, a large number of these matrix elements must be computed between carriers – with varying in-plane wave vectors and in different conduction and valence subbands – occupying a range of QW band states.

The total spontaneous emission rate per unit volume in a given energy range can be obtained by multiplying the downward transition rate per unit volume given in Eq. (2.73) by the number of optical modes in the energy range, $d(\hbar\omega)$, or

$$R_{sp}(\hbar\omega)d(\hbar\omega) \equiv W_{e\to h}\left[V \frac{1}{\pi^2} \frac{\overline{n}^2 \overline{n}_g}{(\hbar c)^3} (\hbar\omega)^2 d(\hbar\omega) \right] , \tag{2.83}$$

where c is the speed of light in free space, $\overline{n}$ is the index of refraction in the crystal, and $\overline{n}_g$ is the group index of refraction that is defined by

$$\overline{n}_g = \overline{n}_{eff} + \omega(d\overline{n}_{eff}/d\omega) \, , \tag{2.84}$$

in which $\overline{n}_{eff}$ is the effective index (phase velocity index) of the guided mode [47]. By relating the energy stored in the wave to the energy of a single photon, the wave vector potential A_0 can be written as

$$A_0 = \sqrt{\frac{2\hbar\omega}{\overline{n}^2 \epsilon_0 \omega V}} \, , \tag{2.85}$$

[2] In a system of units in which energies and lengths are given respectively in eV and Å, M_T can be expressed in eV.

where ϵ_0 is the vaccuum permittivity. We now define Fermi-Dirac distributions for electrons in the conduction band and holes in the valence band as

$$f_{c,v} = (1 + exp\left[E_{e,h} - E_{fc,fv}/k_B T\right])^{-1} \,, \tag{2.86}$$

where k_B is Boltzmann constant, T is the temperature, and $E_{fc,fv}$ are the nonequilibrium quasi-Fermi levels [4]. Substituting Eq. (2.85) into the expression for the transition rate in Eq. (2.79), and using that in Eq. (2.83), we can write (in units of $s^{-1}cm^{-3}eV^{-1}$)

$$R_{sp}(\hbar\omega) = \left(\frac{1}{\hbar\omega}\right) \frac{\pi e^2 \hbar}{3\overline{\mathrm{n}}^2 \epsilon_0 m_0^2} \sum_{polarisations} \mid M_T \mid^2 \frac{1}{\pi^2} \frac{\overline{\mathrm{n}}^2 \overline{\mathrm{n}}_g}{(\hbar c)^3} (\hbar\omega)^2 \delta\left(E_e - E_h - \hbar\omega\right) \times f_c\left(1 - f_v\right) \,. \tag{2.87}$$

In quantum well structures, the matrix element is enhanced for certain electric field polarisations and reduced for others [15]. For total spontaneous emission, we are interested in the total output of light (or total radiative recombination of carriers), and not which polarisations of light are being emitted spontaneously. Therefore, we take the average strength of the transition matrix element over all three polarisations. We note that Eq. (2.87) was derived assuming no mixing between different bands at finite $\mathbf{k}$. In practice, band mixing is generally found in a heterostructure when using an 8-band or 10-band **k.p** Hamiltonian, which modifies the form of the squad matrix element $|M_T|^2$ in Eq. (2.87). We take account of this band mixing explicitly in later chapters in this thesis. Details of the extension of Eq. (2.87) in the case of a multiband Hamiltonian can be found in Ref. [45].

To obtain the spontaneous emission at a given photon energy, we need to convolve R_{sp} with the lineshape function over E_{eh}. In our numerical calculations we use a hyperbolic secant lineshape

$$S(E) = (\pi\Gamma)^{-1} \,\mathrm{sech}\left(\frac{E}{\Gamma}\right) \,, \tag{2.88}$$

where $\Gamma = \frac{\hbar}{\tau}$ is the homogeneous linewidth [12]. The integrated spontaneous emission output is just equal to the total radiative recombination of carriers and is therefore equal to the radiative component of the volume current density required to achieve a given quasi-Fermi level separation. Therefore, we can write

$$j_{rad} = e \int_{\hbar\omega} R_{sp}(\hbar\omega) d(\hbar\omega) \,, \tag{2.89}$$

which is typically presented in units of $kA/(\mu m.cm^2)$.

2.6 Conclusion

In this chapter we have presented the theoretical background which will be relevant to the study of the electronic and optical properties of nitrogen-free and dilute nitride III-V semiconductor materials throughout the remainder of the thesis.

We have overviewed the theoretical methods to calculate the electronic and optical properties of zinc-blende semiconductors and heterostructures. By reviewing the theory of electronic band structure in a solid in Section 2.1, we solved a one-dimensional Schrödinger equation for a simple one-electron system with a periodic potential. In Section 2.2 we have reviewed the one-band **k.p** model for zinc-blende semiconductors, derived using Bloch's theorem.

We have summarised the elasticity and piezoelectricity theory in crystals in Section 2.3, where we represented a general intrinsic strain in a heterostructure as well as the built-in potential due to the piezoelectric effect. Then in Section 2.4 we presented the conduction band anti-crossing model in dilute nitride semiconductors, where we showed that a resonant nitrogen level in these materials leads to a downward shift of the conduction band edge energy. We introduced a 10-band band-anticrossing Hamiltonian to investigate the electronic band structure of III-V dilute nitride semiconductors. Finally, in Section 2.5 we have derived a model to calculate the spontaneous emission rate and radiative current density in quantum well structures. In Chapters 3 and 4 we will use this formalism to investigate and optimise quantum well light emitting diodes.

Chapter 3

Design and optimisation of metamorphic InAsSb/AlInAs mid-infrared 3.3 μm quantum well light emitting diodes

In this chapter we investigate the electronic and optical properties of InAsSb/AlInAs quantum well (QW)-based light emitting diode (LED) structures grown on an AlInAs metamorphic buffer layer (MBL) with the aim of designing efficient strain-balanced QW LED structures emitting at 3.3 μm.

We begin with an introduction and a review of past related works in Section 3.1. In Section 3.2 we benchmark our theoretical model versus experimental data, analysing nitrogen-free $InAs_{1-x}Sb_x/Al_{0.125}In_{0.875}As$ QW LED structures. After benchmarking our calculations against experimental data provided by University of Lancaster and University of Cadiz, and identifying suitable material parameters to use for our modelling, we investigate the electronic and optical properties of these structures. We discuss how our calculations are compared to the experimental PL data provided by University of Lancaster.

The design procedure for strain-balanced QW structures emitting at a desired wavelength is discussed in Section 3.3. We highlight the importance of strain-balancing in QW LED structures before explaining the design procedure we use in our specific calculations.

In Section 3.4, we investigate the routes towards designing optimised metamorphic strain-balanced $InAs_{1-x}Sb_x/Al_yIn_{1-y}As$ QW structures in order to provide a design template for efficient QW LEDs operating at 3.3 μm. We quantify the electronic and optical properties of these structures by analysing their in-plane strain, carrier confinement factor, optical transition

strength, spontaneous emission rate, and radiative current density. We compare the optical properties of these strain-balanced structures to the existing structures investigated in Section 3.2 to justify the benefits of using strain-balanced structures. Finally, in Section 3.5 we conclude.

3.1 Introduction and Motivation

Development of compact and inexpensive semiconductor light sources operating at mid-infrared wavelengths between 2 and 5 μm is of high interest because of their potential for a wide variety of sensing applications, including monitoring of atomospheric pollutants, chemical process control, and biological marker detection in non-invasive medical diagnostics, in addition to potential applications in free-space optical communications and active thermal imaging [48–51]. In particular, gas and biochemical sensing is a crucial component in environmental monitoring applications, with requirements for emissions monitoring in a range of different situations, for example, car exhausts, power stations, coal mines, landfill sites, oild rigs, toxic/volatile chemicals detection at production facilities or disaster zones, and constituent control in pharmaceutical processing. High-sensitivity optical gas detection requires reliable, cost-effective light emitting sources in the mid-infrared region tuned to the fundamental fingerprint absorptions of target gases, which conveniently lie in this technologically important spectral range.

Due to the presence of strong absorption features in the vibrational-rotational spectra of the important greenhouse gases methane (CH_4) and carbon dioxide (CO_2) at respective wavelengths of 3.3 and 4.2 μm, photonic devices operating at these wavelengths are of particular interest for application in environmental monitoring [50]. Quantum cascade lasers have been successfully developed to operate at mid-infrared region [52], but they are complex and expensive to implement. The design of alternating wells and barriers in quantum cascade lasers allows flexibility for a creative engineer to design and explore, but this comes with an expense of several hundred layers [53]. For many applications, mid-infrared LEDs are a far more attractive and cost-effective alternative especially for widespread distributed sensing applications requiring many point sensors. Compared with thermal sources, LEDs are more robust, can operate at high modulation rates, and provide low power consumption better suited to portable instruments [54].

The past decade has witnessed significant advances in the development of GaSb-based diode lasers and LEDs [55–57]. Primarily because of the cost and immature technology associated with the more exotic InAs and GaSb substrates, there has been significant interest in developing mid-infrared LEDs on GaAs substrates using different buffer layer schemes to accommodate the inherent large lattice mismatch with respect to alloys and heterostructures having mid-infrared bandgaps. This has now led to devices of some complexity ranging from LEDs with bulk active

regions in small arrays to multispectral mid-infrared multiple quantum well (MQW) emitters capable of integration [54]. In the 2 – 3 μm spectral range type-I InGaAsSb/AlGa(In)AsSb QWs have demonstrated impressive characteristics, but a combination of Auger recombination and thermal leakage of holes degrade the performance of these devices at and above room temperature for wavelengths $\lambda \gtrsim 3$ μm [58–60]. Further limitations to achieving $\lambda \gtrsim 3$ μm in GaSb-based heterostructures are associated with the presence of (i) a miscibility gap in In- and As-rich GaInAsSb alloys, leading to a reduction in material quality, and (ii) a band structure in which the valence band (VB) spin-orbit splitting energy is close in magnitude to the band gap energy, increasing the possibility of hot-hole producing (CHSH) Auger recombination and inter-valence band absorption [61].

Although inter- and intra-band cascade devices have become well established at wavelengths above 3 μm [62–67], these complicated structures require careful design and optimisation: a typical cascade active region consists of up to 100 layers with tight tolerances on thickness and composition, with the requirement for reproducibility then placing strong demands on epitaxial growth. Furthermore, due to the relative expense and technological immaturity of the GaSb and InAs platforms compared to the GaAs or InP platforms commonly employed in near-infrared optical communications, it is preferable to develop mid-infrared devices on either GaAs or InP substrates. Doing so opens up the potential to reduce fabrication costs, as well as to allow to take advantage of the existing array of high-performance GaAs- and InP-based passive photonic components and integrated circuitry.

3.2 Theory and experiment for 3.3 μm structures

In this section we present and analyse $InAs_{1-x}Sb_x/Al_yIn_{1-y}As$ QWs grown on GaAs substrates, where relaxed $Al_yIn_{1-y}As$ MBLs are used to facilitate growth of these lattice-mismatched heterostructures. The main reason we use this material platform is the fact that these QWs deliver deep type-I band offsets, providing good confinement of both electrons and holes, and thus maximising the electron-hole spatial overlap and minimising thermal carrier leakage.

In Section 3.2.1 we briefly describe the growth and characterisation of the metamorphic QW structures investigated, as well as the experimental measurements performed to analyse the optical properties. Then in Section 3.2.2 we analyse the electronic and optical properties of these devices by presenting the results of our combined experimental and theoretical investigation. We begin with a general analysis of the properties of metamorphic $InAs_{1-x}Sb_x/Al_yIn_{1-y}As$ QWs, before analysing the grown prototypical structures. We show that the prototypical structures we investigate demonstrate (i) strong room temperature PL out to $\lambda = 3.4$ μm, and (ii) a steady increase in peak PL intensity with increasing emission wavelength. Using theoretical calculations we identify and quantify the origin of this behaviour, mainly associated with

compressive stain. Moreover, we describe general trends in the electronic and optical properties of these novel heterostructures, and on this basis evaluate their potential for applications in mid-infrared LEDs. We show that the characteristics of these metamorphic QWs are promising for the development of LEDs operating in the 3 - 4 μm wavelength range, and in particular for sensing applications at wavelengths close to 3.3 μm.

3.2.1 Growth and characterisation

A schematic illustration of the molecular beam epitaxy (MBE) structures grown by University of Lancaster is shown in Fig. 3.1(a). Each structure consists of a 0.4 μm thick GaAs buffer layer, grown at 570° C. Also, a 2 μm thick relaxed $Al_{0.125}In_{0.875}As$ MBL was grown at 510° C on top of the GaAs buffer layer. The structures were cooled to 450° C for the growth of the five-period $InAs_{1-x}Sb_x/Al_{0.125}In_{0.875}As$ active multi-QW layers. The respective thicknesses of the $InAs_{1-x}Sb_x$ QW and $Al_{0.125}In_{0.875}As$ barrier layers were 10.5 and 20 nm. Finally, a 110 nm thick $Al_{0.125}In_{0.875}As$ cap layer was deposited at a temperature of 450° C.

The structures were characterised by a combination of double-crystal x-ray diffraction (DC-XRD), atomic force microscopy and transmission electron microscopy (TEM). Good overall correspondence between the measured and simulated rocking curves is observed, confirming in particular that the $Al_{0.125}In_{0.875}As$ MBL and $InAs_{1-x}Sb_x$ QWs are respectively fully relaxed and pseudomorphically strained (cf. Fig. 3.1(b)). For the four structures MQW1, MQW2, MQW3 and MQW4 grown, respective $x = 0$, 3, 6 and 10% QW Sb compositions were estimated.

Since the QWs in the structure MQW4 – which have the highest QW Sb composition x – are most prone to Sb segregation, TEM imaging was performed by University of Cadiz to evaluate the quality of this structure. The upper panels of Fig. 3.1 (c) indicate a cross-sectional dark-field TEM image of the $InAs_{0.9}Sb_{0.1}/In_{0.875}Al_{0.125}As$ QWs of structure MQW4 where, from left to right, the intensity of the yellow, red, green and blue colouration corresponds to the Al, In, As and Sb compositions in the various layers of the structure. The bottom panel of Fig. 3.1 (c) shows the spatial variations in alloy composition along the growth direction, extracted from energy-dispersive x-ray spectroscopy (EDX) analysis, where solid yellow, red, green and blue lines again denote the variation of the Al, In, As and Sb compositions, respectively. Examining the TEM image, we begin by noting the presence of uniform QW growth, with the structure displaying high crystalline and structural quality: the observed QW-barrier interfaces are sharp, and the QWs display only minor variations in thickness. Turning our attention to the EDX data for group-V atoms, we note firstly that the QW Sb composition x (solid blue line) tends to increase in each QW along the (001) growth direction: in the bottom QW we note an average Sb composition x $\approx$ 8%, which increases to an average value x $\approx$ 11% in the topmost. By contrast, for group-III atoms, the barrier Al composition y (solid yellow line) has a weaker variation across the $Al_yIn_{1-y}As$ layers of the structure, with a measured average value close to

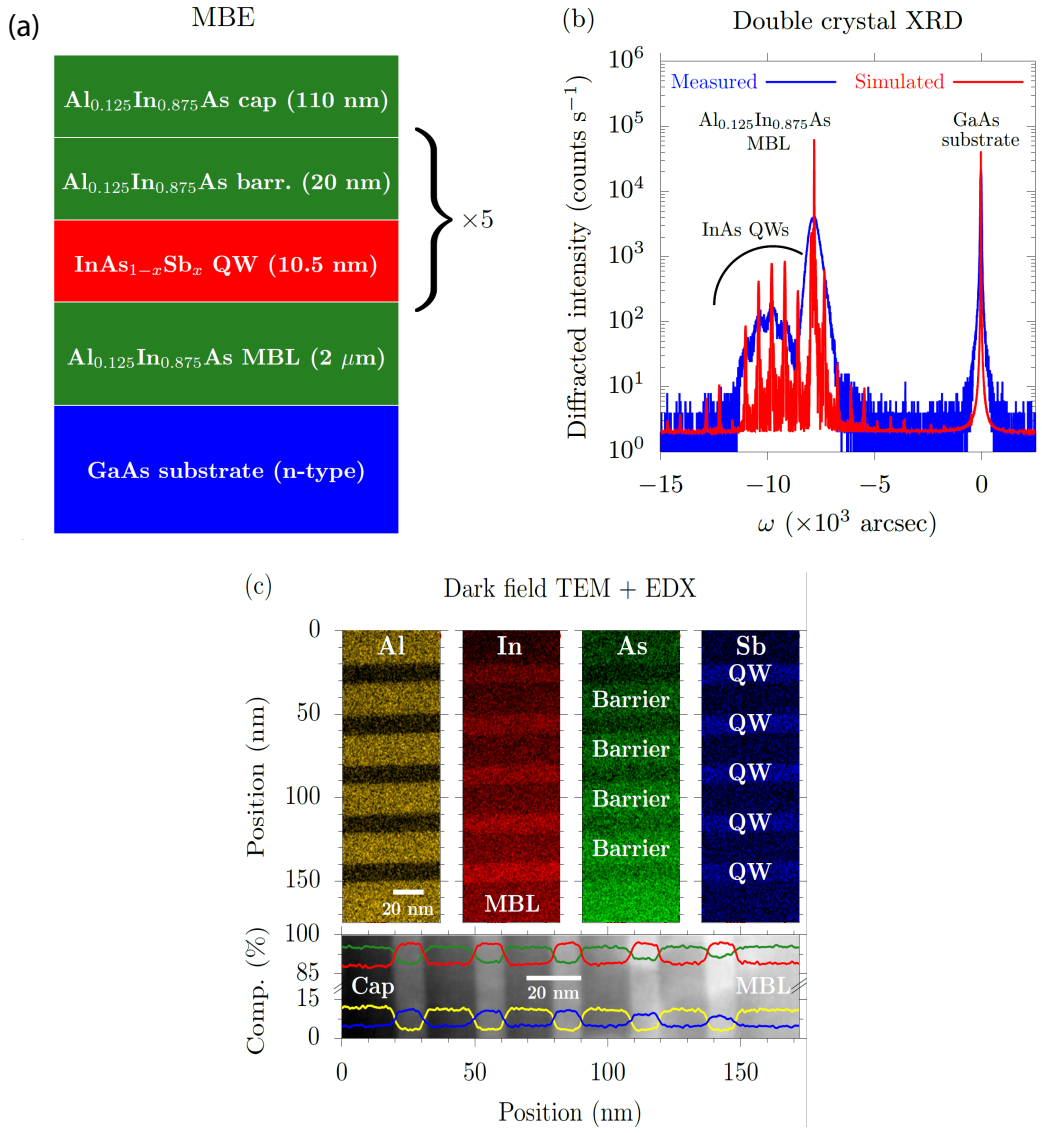


FIGURE 3.1: (a) Schematic illustration of the metamorphic multi-QW structures investigated. The structures consist of compressively strained $InAs_{1-x}Sb_x$ QWs grown between unstrained $Al_{0.125}In_{0.875}As$ barriers, with growth on GaAs facilitated via the use of an $Al_{0.125}In_{0.875}As$ MBL. (b) DC-XRD $\omega - 2\theta$ rocking curve for MQW1, measured (solid blue line) and simulated (solid red line) about the GaAs (004) reflection. (c) Upper panels: false-colour dark-field TEM images for MQW4, where the intensity of the yellow, red, green and blue colouration respectively describes the Al, In, As and Sb compositions in the QW and barrier layers. Lower panel: solid yellow, red, green and blue lines respectively denote the variation of the Al, In, As and Sb compositions along the (001) growth direction for MQW4, as inferred from EDX measurements. For illustrative purposes, the EDX data have been superimposed onto a dark-field TEM image of the structure.

y ≈ 11% in the barrier on the underside of the first QW and an average value y ≈ 12.5% in the barrier on the topside of the fifth QW (i.e. in the capping layer). Overall, we note some intermixing of Al and Sb atoms between the barrier and QW layers: while the Al composition profile extracted from the EDX data shows relative uniformity and sharp interfaces, we note that (i) these interfaces are not precisely step-like, and (ii) the corresponding Sb composition

profile displays both less sharp interfaces and non-zero values in the barrier layers. Overall, we conclude that Sb compositional variations are the most significant structural non-uniformity present in these MBE-grown structures.

3.2.2 Electronic and optical properties

Here we compare our theoretical calculations to PL data provided by Lancaster University. We show how increasing Sb composition x from 0 to 10 % will lead to achieving longer wavelengths. We also calculate the SE spectrum for the aforementioned structures, and benchmark them against PL spectra at $T = 4$ K and $T = 300$ K.

To analyse the optical properties of the structures described in Table 3.1 temperature-dependent PL measurements were performed. The PL measurements were carried out using a 785 nm diode-pumped solid state laser as the optical (excitation) source, with a continuous-wave output power of 200 mW, while the sample temperature was varied between T = 4 and 300 K by means of a closed-cycle He cryostat. The laser spot size was 1 mm^2, corresponding to a power density of 20 $W.cm^{-2}$ at the sample surface. The radiation emitted from the structures upon excitation was collected using CaF_2 lenses and focused onto a Fourier transform mid-infrared spectrometer. To facilitate comparison to experiment we perform SE calculations at a fixed carrier density $n_{3D} = 10^{15}$ cm^{-3}, a low value selected to replicate a typical carrier density associated with optical excitation in the PL measurements. Two-dimensional sheet carrier density is related to the three-dimensional carrier density as $n_{2D} = t_w.n_{3D}$ where t_w is the QW thickness. A 3D carrier density $n_{3D} = 10^{15}$ cm^{-3} is then equivalent to a 2D carrier density of 10^9 cm^{-2} in a QW which is 10 nm thick. Full details of the theoretical model used were presented in Chapter 2.

In order to benchmark our theoretical model as well as to establish a method to design efficient mid-infrared QW LED structures, we have undertaken electronic structure calculations using an 8-band **k.p** Hamiltonian, implemented for QW heterostructures via a numerically efficient reciprocal space (plane wave) method as described in Chapter 2. The temperature dependence of the $InAs_{1-x}Sb_x$ and $Al_yIn_{1-y}As$ band gaps is described via a conventional Varshni parametrisation with the functional form often fitted to the empirical Varshni form $E_g(T) = E_g(T = 0) - [(\alpha T^2)/(T + \beta)]$ where α and β are adjustable (Varshni) parameters [68]. According to Ref. [69], we have used $\alpha = 0.276$ meV/K and $\beta = 93$ K for InAs, and have used $\alpha = 0.32$ meV/K and $\beta = 170$ K for InSb. A linear interpolation has been used for determining these values for ternary $InAs_{1-x}Sb_x$ alloys. Fig. 3.2 shows how the calculated bulk band gap energy of $InAs_{1-x}Sb_x$ is varied as a function of the temperature. The smooth reduction of the bulk band gap energy as a consequence of increasing T should lead to an increase in the emitting wavelength with increasing temperature. The full numerical band structure calculations are required so that the confinement of the carriers can be taken into account. In this regard,

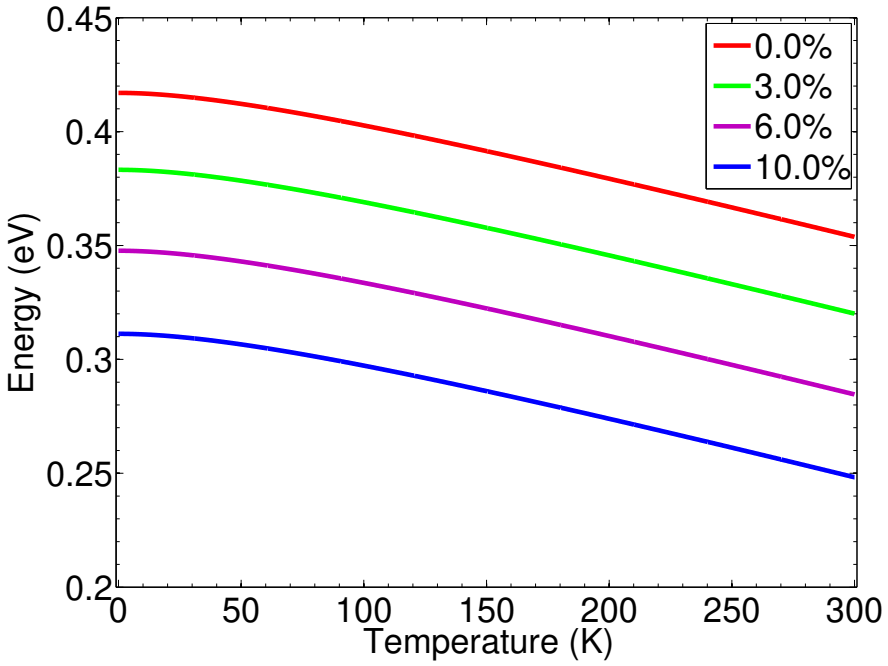


FIGURE 3.2: Calculated temperature dependence of the bulk band gap energy of $InAs_{1-x}Sb_x$ for $x = 0$, 3, 6 and 10%.

the band structure and eigenstates obtained via the multi-band **k.p** calculation for a given QW structure are used directly to compute SE spectra, under the assumption of quasi-equilibrium (thermal) carrier distributions.

MQW1 – MQW4 are assumed ideal, with compressively strained $InAs_{1-x}Sb_x$ QWs of thickness 10.5 nm, surrounded by unstrained $Al_{0.125}In_{0.875}As$ barriers. For these structures, the Sb composition x is treated as the sole free parameter in our calculations: its value is adjusted for each structure to match the measured room temperature PL peak energy. The Sb compositions obtained in this manner are given in parentheses in Table 3.1. The best-fit value of x is exactly the same in MQW1 and is close to the nominal Sb composition indicated by characterisation for MQW2, but is lower than the nominal value in MQW3 and MQW4. A number of factors may contribute to these discrepancies, including fluctuations in QW alloy composition and thickness, inter-diffusion of Al and Sb atoms between the QW and barrier layers, or residual strain in the nominally unstrained barrier layers resulting from incomplete relaxation of the MBL.

We begin our analysis by considering the calculated band structure of bulk-like $InAs_{1-x}Sb_x$ epitaxial layers grown on $Al_yIn_{1-y}As$ MBLs. Solid blue (dashed red) lines in Fig. 3.3(a) denote paths in the composition space along which the band gap E_g (in-plane strain ϵ_{xx}) is constant. The lattice constant of the $Al_yIn_{1-y}As$ MBL varies between that of InAs and AlAs, and is equal to that of InP at $y = 47.7\%$. The validity of our proposed material platform is certified

Structure	x (%)	ϵ_{xx} (%)	ΔE_{CB} (meV)	ΔE_{HH} (meV)	ΔE_{LH} (meV)
MQW1	0.0 (0.0)	−0.82	155	89	33
MQW2	3.0 (3.1)	−1.03	135	135	65
MQW3	6.0 (4.3)	−1.12	128	152	78
MQW4	10.0 (5.7)	−1.21	121	172	92

TABLE 3.1: Details of the MBE-grown $InAs_{1-x}Sb_x/Al_yIn_{1-y}As$ multi-QW structures studied, including the nominal QW Sb composition x, calculated in-plane strain ϵ_{xx}, and calculated CB, HH and LH type-I band offsets ΔE_{CB}, ΔE_{HH} and ΔE_{LH} at $T = 300$ K. Each structure contains five $InAs_{1-x}Sb_x$ QWs, of nominal thickness 10.5 nm. Sb compositions in parentheses are those determined using the theoretical model to fit to the measured PL peak energy at $T = 300$ K.

in Fig. 3.3(a) which suggests that (i) $E_g = 0.376$ eV ($\lambda = 3.3$ μm) can be achieved in bulk for $x \lesssim 5\%$, but with large MBL Al compositions $y \gtrsim 20\%$, corresponding to large strains $\epsilon_{xx} \approx -2\%$ and (ii) $E_g = 0.248$ eV ($\lambda = 5$ μm) can be achieved, e.g., at $x \approx 14\%$ ($\epsilon_{xx} \approx -1.5\%$) via growth on an $Al_{0.1}In_{0.9}As$ MBL. These results suggest that compressively strained $InAs_{1-x}Sb_x$ grown on relaxed $Al_yIn_{1-y}As$ MBLs offer access to a broad range of mid-infrared emission wavelengths $\lambda \gtrsim 3$ μm. We find that with growth on an $Al_{0.125}In_{0.875}As$ MBL, which has a lower lattice constant than InAs, pseudomorphically grown $InAs_{1-x}Sb_x$ alloys are in a state of compressive strain ($\epsilon_{xx} < 0$) and that incorporation of Sb in $InAs_{1-x}Sb_x$ alloys leads to a rapid decrease of the band gap with increasing x, allowing access to mid-infrared emission wavelengths. The initial Al composition $y = 0.125$ was chosen to ensure type-I QWs in the first LED structures grown. We consider in Chapter 4 the impact of reducing the Al composition in the buffer layer, where we show that the initial choice does indeed provide better confinement and recombination coefficients compared to what would be achieved with a lower Al composition in the buffer layer.

We note however that the calculations presented in Fig. 3.3(a) are for bulk-like epitaxial $InAs_{1-x}Sb{-}x$ layers. When considering QWs the confinement energy – typically ~ 50 meV for the lowest energy bound CB ($e1$) and highest energy bound hole ($h1$) states in full numerical calculations – must be accounted for. Hence, achieving a desired QW transition energy ($e1 - hh1$) requires growth of $InAs_{1-x}Sb_x$ QWs having a bulk band gap which is lower by ~ 50 meV, mandating a significant increase in x and hence $|\epsilon_{xx}|$, consequently limiting the accessible wavelength range.

Another important factor while considering growth of QW epitaxial layers is strain-thickness product limit. There have been a number of methods to calculate strain thickness product limit. These calculations primarily differ from each other in the assumed energy stored in a dislocation [5, 70–72]. We use here an approach due to Voisin, as it provides one of the most straightforward routes to estimate the strain-thickness product limit [72]. The energy stored per unit area is defined by $E_s = 2G\left(\frac{1+\sigma}{1-\sigma}\right)\epsilon_{||}^2 t$; where G is the shear module of the layer material, σ is Poisson's ratio and t is the layer thickness. The energy stored per unit area increases linearly with increasing layer thickness t. Expressions vary as to the energy

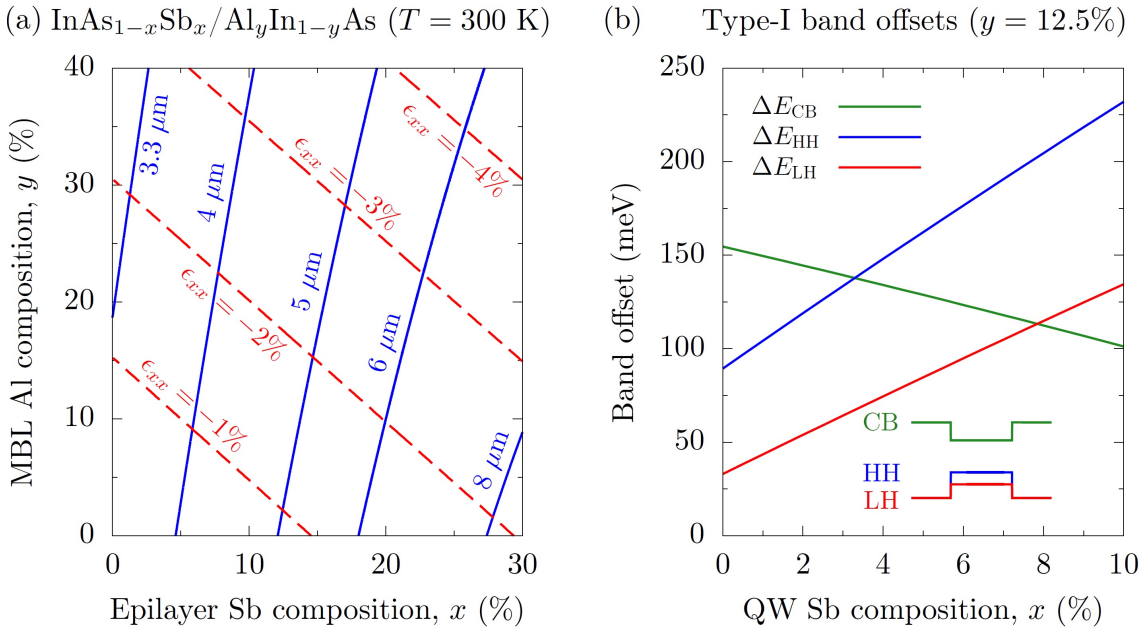


FIGURE 3.3: (a) Composition space map describing the ranges of in-plane strain (ϵ_{xx}) and band gap (at T = 300 K) accessible using bulk-like InAs$_{1-x}$Sb$_x$ epitaxial layers grown on an Al$_y$In$_{1-y}$As MBL. Dashed red and solid blue lines respectively denote paths in the composition space along which ϵ_{xx} and the band gap are constant. (b) Calculated variation of the CB, HH and LH type-I band offsets (solid green, blue and red lines, respectively) with Sb composition x, for compressively strained InAs$_{1-x}$Sb$_x$ QWs grown on an Al$_{0.125}$In$_{0.875}$As MBL.

required to introduce a network of dislocations. However, in all expressions the energy required to introduce a dislocation is large, as it involves breaking a line of bonds. The dislocation energy increases slowly with increasing layer thickness t due to the strain field associated with it [5]. Therefore, there will be a critical layer thickness below which a dislocation-free strained layer will be stable. As an example, by using the expression due to Voisin [5, 72], we estimate a strain-thickness limit $t_c|\epsilon_{xx}| \approx 23$ nm % for InAs$_{1-x}$Sb$_x$/Al$_{0.125}$In$_{0.875}$As. This suggests a maximum permissible strain $|\epsilon_{xx}| \approx 2.3\%$ for a 10 nm thick QW, corresponding to $x \approx 22\%$. For such an InAs$_{0.78}$Sb$_{0.22}$/Al$_{0.125}$In$_{0.875}$As QW we calculate an $e1$-$h1$ transition energy equal to 0.221 eV at T = 300 K, which in turn would suggest that the room temperature emission wavelength is limited to $\lesssim 5.6$ μm. However, further analysis (below) suggests that this upper limit on the emission wavelength is likely reduced in practice.

Turning our attention to InAs$_{1-x}$Sb$_x$/Al$_{0.125}$In$_{0.875}$As QWs, the solid green, blue and red lines in Fig. 3.3(b) respectively show the calculated type-I conduction band (CB), heavy-hole (HH) and light-hole (LH) QW band offsets ΔE_{CB}, ΔE_{HH} and ΔE_{LH}, as a function of the Sb composition x in the QW. At $x = 0\%$ (MQW1) we calculate large type-I CB and HH band offsets, $\Delta E_{CB} = 155$ meV and $\Delta E_{HH} = 89$ meV (cf. Table 3.1). As x increases we calculate a strong increase in ΔE_{HH}, as a result of the increase in (i) the VB offset brought about by Sb incorporation, and (ii) the magnitude $|\epsilon_{xx}|$ of the compressive strain. Contrarily, ΔE_{CB} is decreasing

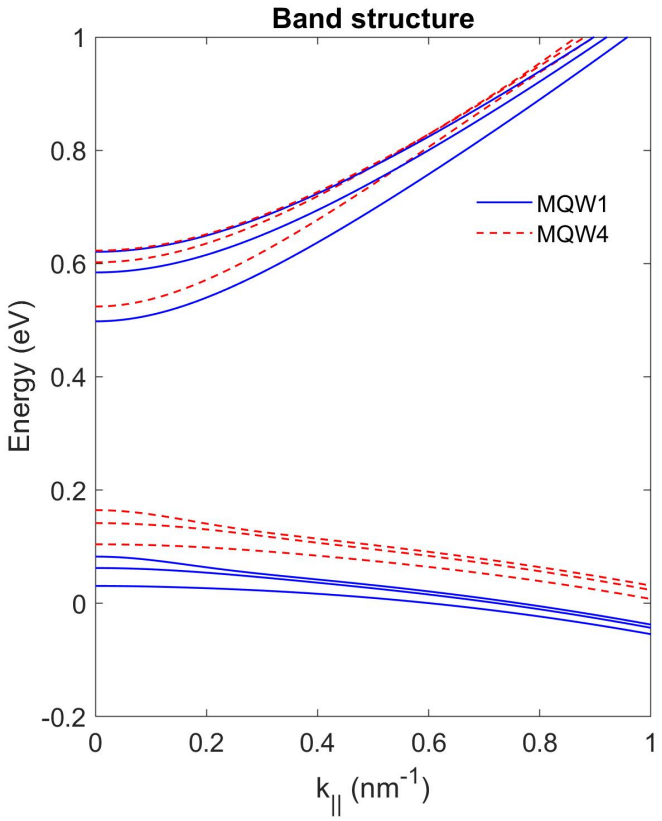


FIGURE 3.4: Calculated CB and VB structure for structures MQW1 (solid blue lines) and MQW4 (dashed red lines) of Table 3.1.

strongly with increasing x – from 151 meV at $x = 0$ to 101 meV at $x = 10\%$ – due to the upward shift of the $InAs_{1-x}Sb_x$ CB edge energy with increasing $|\epsilon_{xx}|$. This suggests that electron confinement is significantly degraded for $x \gtrsim 10\%$, corresponding in a full numerical calculation to $\lambda \gtrsim 3.9$ μm. Therefore, it can be concluded that high type-I band offsets – providing high electron-hole spatial overlap and minimising thermal carrier leakage – can be achieved for $\lambda \lesssim 4$ μm in $InAs_{1-x}Sb_x/Al_{0.125}In_{0.875}As$ QWs having $x \lesssim 10\%$. Achieving the emission wavelength beyond 4 μm is then likely to require careful QW design and optimisation (cf. Chapter 4) [14, 73, 74].

Fig. 3.4 shows the calculated CB and valence band (VB) structure for structures MQW1 (solid blue lines) and MQW4 (dashed red lines) of Table 3.1. The larger compressive strain in MQW4 (cf. Table 3.1) leads to reduced in-plane hole effective masses, and hence an overall reduction in the VB edge DOS. On the basis of the calculated electronic properties we note that (i) achieving longer emission wavelengths requires higher Sb compositions x, but comes at the expense of degrading the electron confinement (cf. Fig. 3.3(b)), and (ii) for fixed MBL Al composition y larger Sb compositions x are associated with larger $|\epsilon_{xx}|$, which in turn is expected to enhance the radiative efficiency [75, 76]. Our analysis therefore identifies an important trade-off for the design of optimised structures to target specific emission wavelengths: sufficiently high

Sb compositions x should be sought to generate appreciable compressive strain in the QW, while also ensuring that x is not so large that thermal leakage of electrons reduces the overall radiative efficiency [74].

Having described general trends in the calculated electronic properties of these structures, we turn our attention to the optical properties. Figs. 3.5(a) and 3.5(b) show the measured PL spectra for the structures of Table 3.1, at respective temperatures $T = 4$ and 300 K. In each case the measured spectra for MQW1 – MQW4 are shown using solid red, green, blue and black lines, respectively. At each temperature the PL spectra have been normalised to the magnitude of the structure having the highest measured PL magnitude (MQW1 at $T = 4$ K, and MQW4 at $T = 300$ K). Examining first the PL spectra measured at $T = 4$ K in Fig. 3.5(a) we note that incorporating Sb leads to a significant redshift of the emission wavelength. For the Sb-free structure MQW1 a PL peak wavelength of 2.51 μm (0.495 eV) is measured, which shifts to 2.95 μm (0.420 eV) in MQW4 which contains 10% Sb. At $T = 300$ K the temperature-induced band gap reduction redshifts these PL peak wavelengths to 2.84 and 3.35 μm (0.437 and 0.370 eV), respectively. For MQW1 we calculate respective peak PL wavelengths of 2.58 and 2.91 μm, corresponding to respective PL peak energies of 0.480 and 0.426 eV. Looking at the theoretical calculations, we notice an underestimation of the measured PL peak energy by only 15 meV (11 meV) at $T = 4$ K (300 K), suggesting good agreement between theory and experiment. We note that these small deviations between the measured and calculated values for the Sb-free structure are likely attributable to inhomogeneities in the structure due, e.g., to fluctuations in QW thickness, or diffusion of Al atoms into the QW from the surrounding barrier layers during growth.

At $T = 4$ and 300 K a similar overall character of the measured PL spectra is observed. Firstly, all spectra possess a single, well-defined emission peak, suggesting that the measured PL is generated by recombination of electrons (and probably holes) occupying a single respective conduction subband. This is consistent with the low carrier densities generated by optical excitation, whereby we expect that excited carriers thermalise rapidly into the $e1$ and $hh1$ subbands. Secondly, while the measured PL spectra at $T = 4$ K are approximately symmetric about the peak, at $T = 300$ K we note the presence of a pronounced tail on the high energy (low wavelength) side of the peak. This is consistent with the presence of thermalised carrier distributions, describable by separate electron and hole quasi-Fermi distribution functions, whereby carriers at higher temperature occupy subband states over larger ranges of energies than at low temperature.

Turning our attention to the intensity of the measured PL spectra, at $T = 4$ K we note that the measured peak PL intensity remains relatively constant for all structures, reducing by approximately 10% in going from the Sb-free MQW1 to MQW4 in which $x = 10\%$. Conversely, at $T = 300$ K we note that the measured peak PL intensity increases strongly with increasing

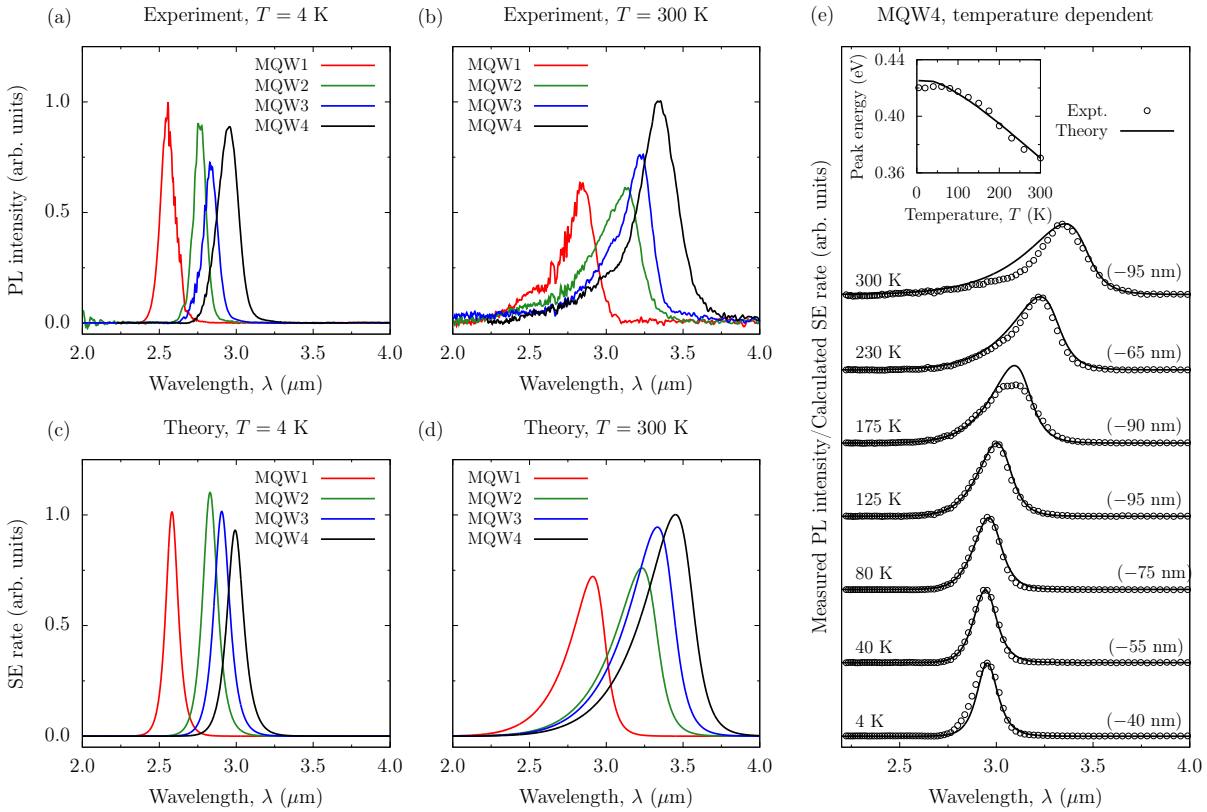


FIGURE 3.5: Measured PL spectra for structures MQW1 – MQW4 (solid red, green, blue and black lines, respectively) at temperatures (a) $T = 4$ K, and (b) $T = 300$ K. The corresponding calculated SE spectra for structures MQW1 – MQW4 at $T = 4$ and 300 K are shown respectively in (c) and (d). At each temperature the values of the measured PL and calculated SE have been normalised to that of the structure having the highest measured PL intensity (MQW1 at 4 K, and MQW4 at 300 K). The full temperature-dependent set of measured PL and calculated SE spectra for MQW4 are shown in (e) using, respectively, open circles and solid black lines. The calculated SE spectra in (e) have, at each temperature, been normalised in intensity (except at $T = 175$ K; see text) and shifted in wavelength (by the amount specified in parentheses) to match the experimental data at the PL peak. The open circles (solid black line) in the inset to (e) show the measured (calculated) variation of the PL (SE) peak energy with temperature in MQW4, where a rigid 11 meV redshift has been applied to the calculated SE peak energies.

Sb composition x – or, equivalently, increasing emission wavelength – with the measured peak PL intensity for MQW4 at $T = 300$ K being larger by approximately two-thirds than that measured for MQW1 at the same temperature. We note that the measured peak PL intensity at $T = 300$ K is reduced by a factor of approximately 300 compared to that measured at $T = 4$ K, for all structures studied. Overall, we note that this trend is promising from the perspective of device applications at wavelengths $\gtrsim 3$ μm, since the requirement to incorporate Sb to reach these wavelengths appears to be associated with an intrinsic enhancement of the radative efficiency of a multi-QW structure.

Figs. 3.5(c) and 3.5(d) show the calculated SE spectra for the structures of Table 3.1, at respective temperatures $T = 4$ and 300 K. The line colours and normalisation of the peak SE rate are as in Figs. 3.5(a) and 3.5(b). We note good overall qualitative agreement with the

measured PL spectra of Figs. 3.5(a) and 3.5(b). At $T = 4$ K the peak measured PL intensity and calculated SE rate reduce by $\lesssim 10\%$ as x increases from 0 (MQW1) to 10% (MQW4), while at $T = 300$ K the peak measured PL intensity and calculated SE rate increases by $\gtrsim 30\%$ between $x = 0$ and 10%. On this basis we conclude that the theoretical model correctly captures the key observed trends in the experimental measurements: at low temperature the emission intensity is roughly independent of x (or, equivalently, λ), while at room temperature the emission intensity increases with increasing λ.

Fig. 3.5(e) shows the measured PL (open circles) and calculated SE (solid lines) spectra for MQW4 ($x = 10\%$), for a range of temperatures from $T = 4$ to 300 K. To facilitate comparison of the overall character of the measured and calculated spectra, the calculated SE spectra at each temperature have been (i) shifted in wavelength (by the amount denoted in parentheses) to the peak of the corresponding measured PL spectrum, and (ii) normalised to the magnitude of the PL peak in the measured spectrum. We again note overall good agreement between theory and experiment. The calculated SE spectra – in which the spectral broadening is described by a hyperbolic secant lineshape of width 6.6 meV – describe that the spectral broadening of the measured PL spectra is typical of that of a conventional III-V semiconductor alloy, [12] suggesting high material quality in the metamorphic QWs. The inset to Fig. 3.5(e) shows the variation with temperature of the measured PL (open circles) and calculated SE (solid line) peak energy, where no shifts have been applied to the calculated data. The close agreement between theory and experiment here verifies that the temperature dependence of the measured PL peak energy is well described via the conventional Varshni parametrisation. [68, 69]

To identify and quantify the origin of the measured increase in room temperature PL intensity with increasing λ we have analysed the contributions made by the band gap (emission wavelength), inter-band optical matrix elements, and electron and hole quasi-Fermi levels [12, 77, 78] to the calculated SE spectra for each structure. For a QW of fixed thickness, the SE rate at fixed carrier density n is directly proportional to the photon energy, so that the decrease in band gap with increasing x acts to decrease the peak SE rate. For MQW1 we calculate an inter-band optical transition strength 19.0 eV – where the relevant scale [45] is the Kane parameter E_P – for the TE-polarised e_1-hh_1 transition at $k_{||} = 0$, which decreases to 18.1 eV in MQW4. Both of these contributions then act to reduce the peak SE rate at fixed n, suggesting that the filling of the QW energy bands – described by the electron and hole quasi-Fermi levels – is responsible for the calculated increase in the peak SE rate with increasing λ.

The calculated carrier (quasi-Fermi) distributions for MQW1 – MQW4 confirms that the reduction of the VB edge DOS brought about by compressive strain at larger x (cf. Fig. 3.3(c)) is sufficient to increase the peak SE rate at fixed n. The larger effective masses in the VB compared to the CB lead to holes occupying $hh1$ subband states over a smaller (larger) range of energies (in-plane wave vectors, $k_{||}$) than those occupied by electrons in the $e1$ subband.

The strict **k**-selection associated with optical transitions then renders holes occupying states at larger $k_{||}$ unavailable to undergo radiative recombination, due to a lack of $e1$ electrons occupying states at the same wave vector. [76] As the in-plane effective mass of the $hh1$ VB decreases with increasing x, the DOS at the VB edge reduces to more closely match that at the CB edge. This allows holes to occupy $hh1$ subband states over an increased (reduced) range of energy ($k_{||}$) – reflected in a reduction in the hole quasi-Fermi level at fixed n – making more electron-hole pairs available to undergo radiative recombination and contribute to the SE.

At $T = 4$ K this effect is not pronounced since at low temperature the quasi-Fermi distribution functions are step-like about the quasi-Fermi levels, with carriers occupying subband states across a limited range of $k_{||}$. As a result, the calculated peak SE rate at $T = 4$ K depends only weakly on x (cf. Fig. 3.5(c)). Conversely, at $T = 300$ K the hole quasi-Fermi distribution possesses a significant tail at energies below the hole quasi-Fermi level, describing that, on average, holes occupy states over a larger range of $k_{||}$ than at low temperatures. As such, the impact of the strain-induced reduction in the VB edge DOS with increasing λ becomes pronounced, leading to the calculated 30% increase in the peak SE rate between structures MQW1 and MQW4 at $T = 300$ K (cf. Fig. 3.5(d)).

To obtain a quantitative measure of the impact of Sb incorporation on the SE rate we compute the radiative recombination coefficient B at $T = 300$ K for each structure by (i) calculating the radiative current density J_{rad} via integration of the calculated SE spectrum of Fig. 3.5(d), and (ii) assuming $J_{\text{rad}} = eBn^2$ (i.e. the Boltzmann approximation). Given the expected [79] weak dependence of B on n up to $n \sim 10^{17}$ cm^{-3} (a carrier density typical of operation of an electrically pumped QW-LED), we anticipate that the values of B computed in this manner describe trends which should remain largely valid for practical LED devices. [74] We calculate $B = 0.56$ and 0.72×10^{-4} cm^2 s^{-1} for MQW1 and MQW4 respectively, describing a predicted increase of approximately 29% in the radiative emission rate between $x = 0$ and 10%. Further theoretical analysis suggests that the radiative emission rate can be enhanced further in structures designed to emit at 3.3 μm, via the design and optimisation of strain-balanced structures [73, 74].

Although the existing devices investigated in this section are emitting at or near $\lambda \approx 3.3$ μm, there is still scope to design more efficient InAsSb/AlInAs QW LED structures emitting at $\lambda = 3.3$ μm. This is feasible by designing strain-balanced structures which are not only defect-free structures, but can also deliver better optical performance. In the next section, we discuss the theory of strain-balancing in epitaxial QW layers. Then in Section 3.4, we investigate the routes to design strain-balanced $InAs_{1-x}Sb_x/Al_yIn_{1-y}As$ QW structures providing a design template for efficient QW LEDs operating at 3.3 μm.

3.3 Strain-balanced structures: design procedure

In this section we turn our attention to designing strain-balanced QW structures. So long as the strain in each layer does not exceed a critical value, it is then in principle possible to grow strain-balanced structures where no maximum is set on the number of QWs, unlike in the case of lattice-matched barriers. The useful growth combinations are then compressive wells with tensile barriers, and tensile wells with compressive barriers. In addition, structures can be grown which contain both compressive and tensile wells with unstrained barriers [6].

There is a limit to the amount of strained material that can be grown before plastic relaxation occurs and hence a limit to the number of strained quantum wells that can be grown between lattice-matched barriers while maintaining device – quality material [6]. It is however possible to avoid this problem by using oppositely strained well and barrier materials to balance out the strain over an entire structure. Two epitaxially strained layers – having thicknesses t_w and t_b are strain-balanced when their average in-plane stress vanishes, in which case it can be shown that the thickness ratio of the barrier and well thickness could be defined as the ratio of material parameters of the barrier and the well

$$\frac{t_b}{t_w} = -\frac{A_w \epsilon_{||,w} a_{l,b}}{A_b \epsilon_{||,b} a_{l,w}} \ , \tag{3.1}$$

where the relaxed lattice constant of barrier and well are shown by $a_{l,b}$ and $a_{l,w}$, respectively; and $\epsilon_{||,b}$ and $\epsilon_{||,w}$ respectively denote the in-plane strain in barrier and well [13]. A_b and A_w are also defined as a function of the elastic constants of barrier and well, respectively:

$$A_b = C_{11,b} + C_{12,b} - 2C_{11,b}^{-1} C_{12,b}^2, \tag{3.2}$$

$$A_w = C_{11,w} + C_{12,w} - 2C_{11,w}^{-1} C_{12,w}^2. \tag{3.3}$$

Here, we denote the $Al_yIn_{1-y}As$ barrier layer and $InAs_{1-x}Sb_x$ well layer by b and w, respectively.

The design procedure that we follow for $InAs_{1-x}Sb_x/Al_yIn_{1-y}As$ structures is as follows:

- Firstly, we define t_w and t_b.

- Secondly, we find the ratio between x and y satisfying Eq. 3.1.

- Finally, we vary x (and consequently y to satisfy Eq. 3.1) in order to produce a desired QW band gap energy.

Using this procedure, we provide a design template for strain-balanced $InAs_{1-x}Sb_x/Al_yIn_{1-y}As$ QW structures emitting at a fixed wavelength. This model can also be used for designing

structures using any given material platform of ternary III-V semiconductors with any given thickness ratio t_b/t_w. As the sign convention, we note here that throughout this chapter the in-plane strain $\epsilon_{xx} > 0$ and $\epsilon_{xx} < 0$ correspond to tensile and compressive strain, respectively. As we will show, while changing the strain in the QW we can also adjust the QW thickness in order to maintain 3.3 μm emission.

3.4 Optimisation of InAsSb/AlInAs quantum wells for 3.3 μm emission

In this section, we start by designing strain-balanced $InAs_{1-x}Sb_x/Al_yIn_{1-y}As$ QWs, grown on relaxed $Al_{0.125}In_{0.875}As$ MBL designed to emit at 3.3 μm. Then, we discuss and analyse the optoelectronic properties of these structures. The layout of the QW LED structure is shown in Fig. 3.6. Based on the established epitaxial growth mentioned in Sec 3.2.1, we consider structures grown on an $Al_{0.125}In_{0.875}As$ MBL. To target 3.3 μm emission we focus on nitrogen-free $InAs_{1-x}Sb_x/Al_yIn_{1-y}As$ QWs, where we constrain the Sb composition x in the compressively strained QW layers and Al composition y in the tensile strained barrier layers to (i) obtain the peak of the SE spectrum at room temperature at 3.3 μm, and (ii) produce overall strain-balancing by choosing x and y for the corresponding QW and barrier thicknesses, to produce zero net in-plane stress in the structure. Repeating this procedure as a function of the QW thickness, t_w, we identify strain-balanced structures emitting at 3.3 μm. Finally, by analysing SE rate and generated radiative current density we discuss the effect of strain-balancing on the performance of these devices.

In Section 3.2.2 we investigated the validity of the model being used for InAsSb bulk band structure, as presented in Fig. 3.3(a). Here we evaluate the potential to engineer the electronic band structure of $InAs_{1-x}Sb_x/Al_yIn_{1-y}As$ QWs in order to design strain-balanced QW LED structures operating at 3.3 μm. We clarify general trends in the predicted properties of these devices, and identify structures that deliver optimal electronic and optical performance. We analyse the performance of candidate LED structures by computing band offsets, optical transition strength, SE spectrum and the relevant radiative current density at fixed temperature and injected carrier density. We identify a number of interacting and competing effects that govern the LED characteristics:

1) Band offsets:

The CB and VB offsets depend on the material systems used in the QW structures. Thermal leakage of the carriers should be minimised in type-I structures with larger band offsets.

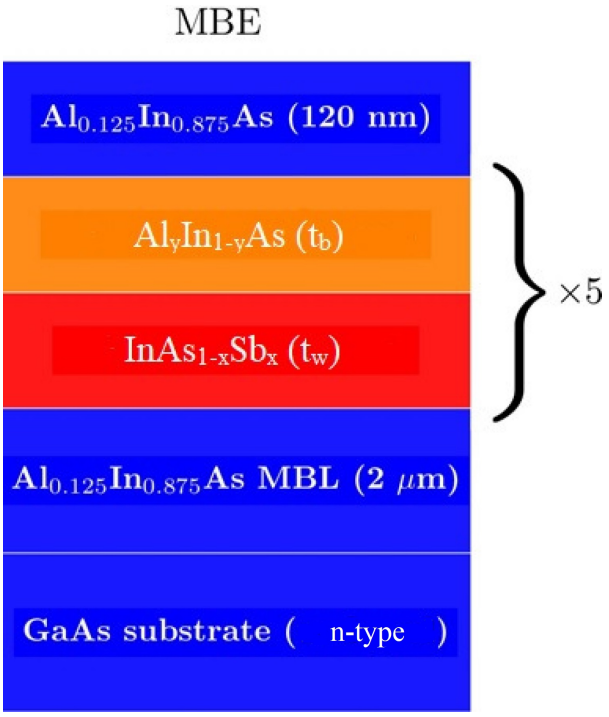


FIGURE 3.6: Schematic illustration of the structures considered to design strain-balanced QW LED devices.

2) Valence band density of states:

The incorporation of compressive strain into a QW splits the degeneracy of the LH and HH states at the valence band maximum [5], which leads to a reduced in-plane hole effective mass, and consequently a reduced density of states [80]. The valence band DOS should be minimised in thin, highly strained wells, where the subband separation is maximised [81–83].

3) Optical transition strengths:

The optical transition strength depends directly on the degree of overlap between the electron and hole envelope functions. As the electron envelope function tends for narrow wells to penetrate more strongly into the barrier compared to the hole envelope function, the transition strength increases with increasing QW thickness in conflict with the DOS which is optimised for narrow wells [83].

4) Spontaneous emission rate and radiative current density at a fixed carrier density:

Increasing compressive strain reduces the effective masses of the QW hole states in the plane of the QW, which in turn leads to a reduction of the DOS close to the VB edge. The hole effective masses increase in response to the reduced compressive strain, and the VB structure changes in such a way that holes occupy states over a smaller range of $\mathbf{k}$. This then makes the overall QW band structure more symmetric about the centre of the band gap, and means that

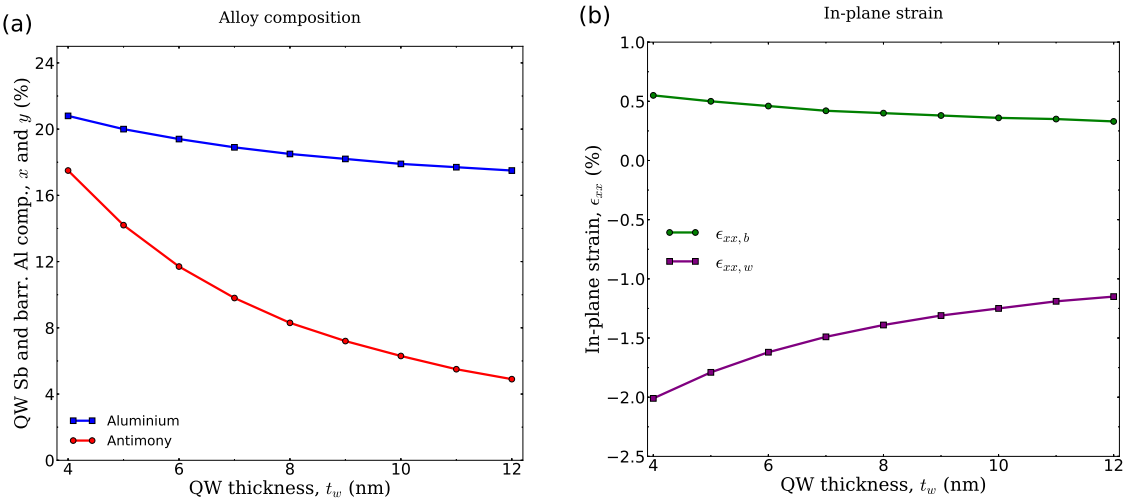


FIGURE 3.7: (a) $InAs_{1-x}Sb_x$ QW alloy Sb composition x, and $Al_yIn_{1-y}As$ barrier alloy Al composition y required to maintain $\lambda = 3.3$ μm and to satisfy strain-balancing condition as a function of QW thickness. Blue curve denotes the Al composition in $Al_yIn_{1-y}As$ barrier alloy, and red curve denotes Sb composition in $InAs_{1-x}Sb_x$ QW alloy. (b) Calculated in-plane strain in the well (purple curve) and in the barrier (green curve) as a function of QW thickness.

there are more holes available to undergo optical recombination and hence contribute to the SE.

3.4.1 Electronic properties

In order to provide a design template for 3.3 μm QW LEDs, we have considered structures with barrier to well thickness ratio of $t_b/t_w = 3$ with t_w ranging from 4 nm to 12 nm. For each structure, we have obtained the relevant compositions in the well and in the barrier as outlined in Section 3.3 to design a strain-balanced structure with the peak of SE rate at 3.3 μm.

The range of Sb composition x in $InAs_{1-x}Sb_x$ QWs and that of Al composition y in $Al_yIn_{1-y}As$ barriers that can be used in compressively strained well and tensile strained barrier structures to operate at 3.3 μm with $t_b = 3t_w$ and subject to the above constraints are shown in Fig. 3.7(a) as a function of QW thickness t_w. The range of Sb compositions required to achieve 3.3 μm emission ranges from 17.5% in a narrow QW having $t_w = 4$ nm, to 4.9% in a wide QW having $t_w = 12$ nm. The decrease in x required to maintain fixed emission wavelength with increasing t_w is associated with the smaller confinement energy in a wider QW. The range of Al composition y in the $Al_yIn_{1-y}As$ barrier is chosen in order (i) to satisfy the strain-balancing condition, and (ii) to determine the carrier confinement energies when designing the QW band gap energy. As Sb composition in the well decreases with increasing QW thickness, the magnitude of the in-plane strain in the well $|\epsilon_{xx,w}|$ also drops as a consequence of the decrease in the lattice constant of $InAs_{1-x}Sb_x$ in the well. Therefore, the Al composition in

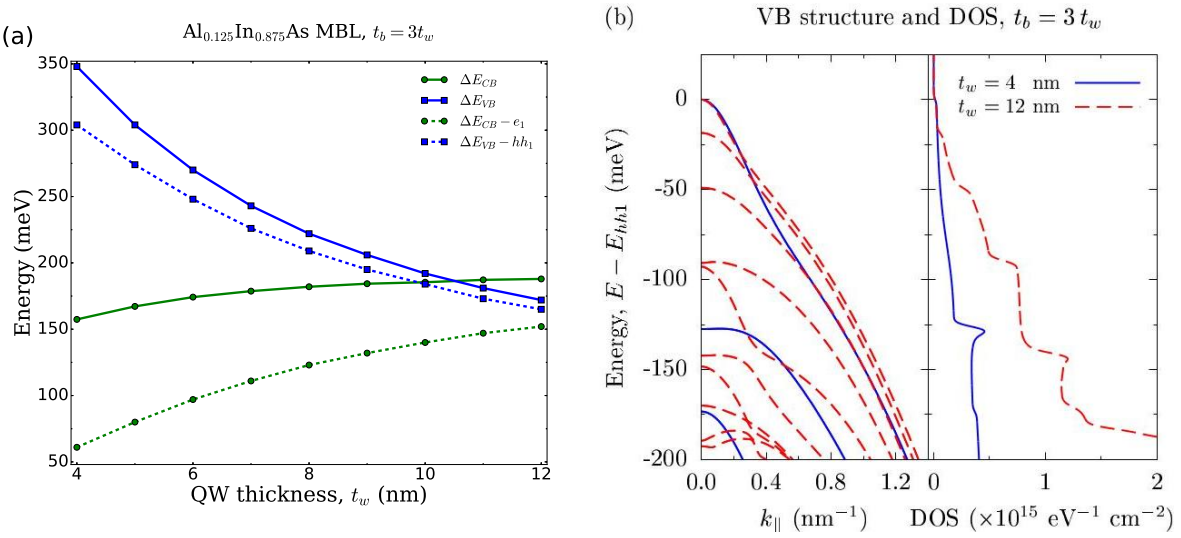


FIGURE 3.8: (a) Calculated variation of CB and VB offsets and carrier confinement energy with QW thickness t_w. (b) Calculated VB strcuture (left panel) and DOS (right panel) for structures with the narrowest well width, $t_w = 4$ nm (solid blue curve), and the widest well width, $t_w = 12$ nm (dashed red curve). For each structure the zero of energy has been set at the QW VB edge – i.e. at the energy of the highest energy valence subband $hh1$, which is purely HH-like at $k_{||} = 0$.

the barrier also decreases from 21.6% to 17.7% with increasing well width, to compensate the reduced compressive in-plane strain in the well and to maintain the strain-balancing condition.

As already mentioned, the structures are designed to have compressive in-plane strain in the well and tensile strain in the barrier. Fig. 3.7(b) shows how $\epsilon_{xx,w}$ and $\epsilon_{xx,b}$ vary as a function of t_w. As mentioned above, due to the presence of less Sb in the wider wells, the compressive in-plane strain in the well $\epsilon_{xx,w}$ varies from -2.01% to -1.15% with increasing QW thickness. Also, having less Al in the barrier with increasing well width results in a decrease of the tensile strain in the barrier $\epsilon_{xx,b}$, from 0.55% to 0.33%.

The calculated variation of the type-I CB and VB offsets, ΔE_{CB} and ΔE_{VB}, with well width for the proposed structures are shown in Fig. 3.8(a). In order to avoid thermal leakage of carriers, CB and VB offsets must generally be greater than $3kT$ where k is the Boltzmann's constant. The CB offset remains nearly constant, increasing from 157 to 188 meV with increasing t_w from 4 to 12 nm. This is because of a tradeoff between the CB edge being pushed down due to less Sb in wider structures and the effect of the hydrostatic strain pushing up the CB edge. The calculated, roughly linear, decrease in ΔE_{VB} (the band offset between the HH band edge of the well and LH band edge of the barrier) with increasing QW thickness is primarily associated with the decrease in x. Although the VB offsets decrease with increasing well width, they are still large enough to minimise thermal leakage, with ΔE_{VB} ranging from 348 to 172 meV. Carrier confinement energy is another important factor when considering carrier thermal leakage in QW structures, which is defined by calculating the difference in energy between the

CB (highest VB) edge of the barrier and the first electron (hole) state. Electron confinement energy $\Delta E_{CB} - e_1$ increases from 61 meV to 152 meV with varying QW thickness t_w from 4 nm to 12 nm. However, calculated hole confinement energy $\Delta E_{VB} - hh_1$ shows a strong confinement as it varies from 304 meV to 165 meV with varying t_w from 4 nm to 12 nm. Therefore, given the tradeoff between electron and hole confinement energy as a function of QW thickness, and the fact that holes are more strongly confined in these QW structures, one can consider using QW structures with wider QW thickness t_w in order to minimise electron thermal leakage.

The left- and right-hand panels of Fig. 3.8(b) respectively show the calculated VB structure and DOS for the narrowest and widest proposed strain-balanced structures. The larger compressive strain in the narrower structure, $t_w = 4$ nm, leads to reduced in-plane hole effective masses, and hence an overall reduction in the VB edge DOS compared to the wider structure, $t_w = 12$ nm.

To quantify the impact of the band offsets on the expected characteristics of the QW LED we have calculated the fraction of the total electron and hole charge density confined within the QW. Wider structures can more effectively confine the carriers inside the well and prevent them from spreading into the barrier. We calculate that the total electron charge density increases from 64.5% to 91.3% when increasing the well width from 4 nm to 12 nm. However, due to a high hole effective mass, the hole charge density remains nearly constant $\approx 95.5\%$ as a function of QW thickness.

Another important parameter for determining the ability of a given QW structure to absorb or emit light is the optical transition strength. In practice, this is calculated via the matrix elements of the momentum operator between the initial and final states involved in a given optical absorption or emission process. We calculate $|M_{e1,h1}|^2$ varying, roughly linearly, from 13.5 to 19.7 eV with increasing t_w from 4 to 12 nm. As discussed in Sec. 2.5, optical transition strength plays an important role in calculating the optical properties of QW LEDs. We will discuss and analyse the optical properties of our proposed strain-balanced QW LED structures in the next section.

3.4.2 Optical properties

Having analysed the electronic properties of strain-balanced $InAs_{1-x}Sb_x/Al_yIn_{1-y}As$ QW LEDs designed to emit at $\lambda = 3.3$ μm, we now turn our attention to investigating the optical properties, such as SE spectra and radiative current density, of these devices.

Fig. 3.9(a) shows the calculated SE spectra of the structures reported in Section 3.4.1. We have used a fixed carrier density ($n_{2D} = 10^{11}$ cm^{-2}) to calculate the SE spectrum of each structure. As already mentioned above, by increasing QW thickness, less Sb is required to achieve 3.3 μm

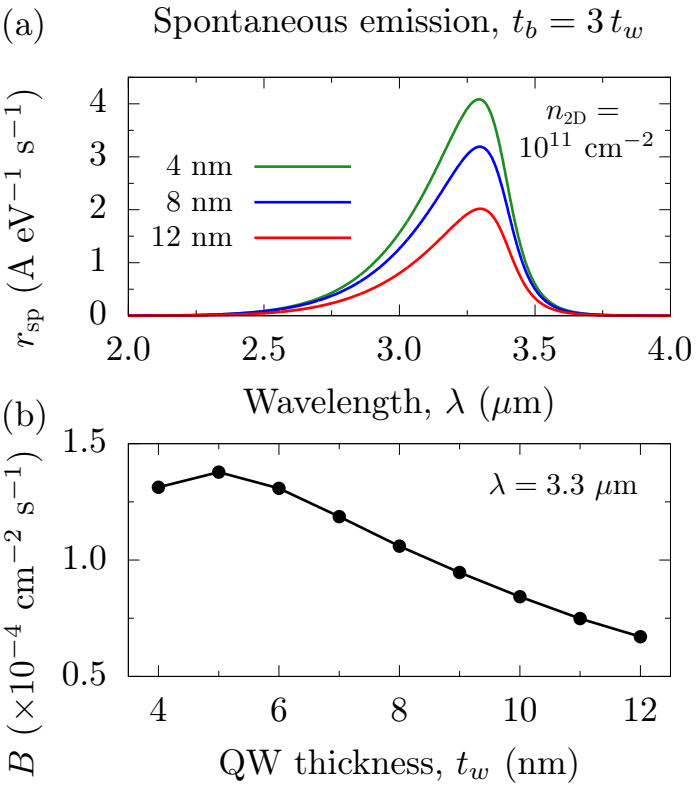


FIGURE 3.9: Summary of calculated optical properties for $InAs_xSb_{1-x}/Al_yIn_{1-y}As$ QW structures grown on $Al_{0.125}In_{0.875}As$ MBL emitting at $\lambda = 3.3$ μm at T = 300 K. (a) Calculated variation of SE spectra with wavelength λ. (b) Calculated variation of the radiative recombination coefficient B with QW thickness t_w in the 3.3 μm QW LEDs. x and y vary from 17.5% to 4.9% and 21.6% to 17.7% respectively with increasing the QW thickness from 4 to 12 nm.

emission in wider structures. The lower Sb composition in the well means that compressive in-plane strain in the well would also decrease as a consequence of the lattice constant of the well getting closer to that of the substrate. The decrement in the compressive strain leads to an increment in the effective masses of the QW hole states in the plane of the QW, which in turn leads to an increment of the density of states close to the VB edge. As the Sb composition decreases and the hole effective masses increase in response to the reduced compressive strain, the VB structure changes in such a way that holes occupy states over a larger range of **k**. This then makes the overall QW band structure less symmetric about the centre of the band gap, and means that there are fewer holes available to undergo optical recombination and hence contribute to the SE. Hence, the peak of the SE rate decreases in wider structures having less Sb.

Fig. 3.9(b) summarises the calculated radiative recombination coefficient B of these 3.3 μm strain-balanced structures. Here, the radiative recombination coefficient B has been computed by (i) integrating over the calculated SE spectrum to obtain the radiative current density J_{rad}, and (ii) writing $J_{rad} = eBn_{2D}^2$ in the Boltzmann approximation. In order to remove any explicit dependence on t_w, we present B in two-dimensional units. At 3.3 μm we calculate a maximum value $B = 1.38 \times 10^{-4}$ cm^2 s^{-1} for a narrow QW having $t_w = 5$ nm, which decreases by a

factor of approximately two as t_w is increased to 12 nm. While detailed investigation of non-radiative recombination in these structures is beyond the scope of this thesis, we note on the basis of detailed analysis of the calculated electronic properties (i) that both the hot electron- and hole-producing (CHCC) and (CHSH) Auger recombination mechanisms are likely to play a role in limiting the overall radiative efficiency, and (ii) while it may be possible to engineer the QW VB structure to reduce the CHSH recombination rate [16], the mixing of LH- and SO-like eigenstates brought about by strain and quantum confinement effects likely render the CHSH process thresholdless.

As a comparison to the existing QW LED structures described in Section 3.2, we compare the calculated radiative recombination coefficient B of 3.3 μm strain-balanced structures with existing MQW structures. In Section 3.2, we argued that even though increasing Sb composition may not be favourable as a growth point of view, it leads to an improved optical performance of the device. The calculated radiative recombination coefficient B of these existing devices reaches to a maximum of $B = 0.72 \times 10^{-4}$ cm^2 s^{-1} in MQW4 with $x = 10\%$. By comparison the designed strain-balanced QW structure with roughly the same Sb composition ($x = 9.8$ %) delivers a significantly improved optical behaviour of the device, with $B = 1.06 \times 10^{-4}$ cm^2 s^{-1} – c.f. the calculated radiative coefficient B of the structure with $t_w = 8$ nm shown in Fig. 3.9(b). This shows an enhancement of almost 50% in the optical performance of the device.

3.5 Conclusions

In this chapter we have presented a theoretical investigation and optimisation of the electronic and optical properties of 3.3 μm InAsSb quantum well structures grown on AlInAs metamorphic buffer layers.

By quantifying the scope offered by this material system to use strain and band structure engineering we demonstrated that there is large scope for the design of quantum well structures, incorporating compressively strained ternary InAsSb quantum wells having unstrained or tensile strained ternary AlInAs barriers. Such quantum well structures combine large type-I band offsets with emission wavelengths ~ 3.3 μm, offering the possibility to design devices having high optical efficiency and reduced temperature sensitivity, and making these structures particularly appealing for the development of light emitting diodes operating at mid-infrared.

We have defined design criteria to achieve strain-balanced quantum well structures at a desired emission wavelength, thereby providing a general method which can be applied to produce candidate multi-quantum well or superlattice structures for epitaxial growth and experimental investigation. Via a systematic analysis of strain-balanced quantum well structures designed

to emit at 3.3 μm we identified key trends in their electronic and optical properties and performance as functions of alloy composition, quantum well thickness and epitaxial strain.

Overall, our theoretical analysis has identified important trends in the performance of GaAs-based metamorphic quantum well light emitting diodes operating at mid-infrared wavelength, has provided guidelines for the growth of optimised devices suitable for practical applications, and has confirmed the promise of these novel metamorphic heterostructures for the development of high-performance mid-infrared light emitting sources.

Chapter 4

Design and optimisation of dilute nitride metamorphic mid-infrared quantum well light emitting diodes

In this chapter we investigate the electronic and optical properties of InNAsSb/AlInAs quantum well (QW)-based light emitting diode (LED) structures grown on an AlInAs metamorphic buffer layer (MBL) with the aim of designing efficient strain-balanced QW LED structures emitting at 4.2 μm.

In Section 4.1, we discuss the possibility of using metamorphic $InN_y(As_{1-x}Sb_x)_{1-y}/Al_zIn_{1-z}As$ QW structures to emit at $\lambda \geq 4$ μm by studying the bulk-like composition space map of this material platform. Due to their potential to facilitate the improvement of optical and electronic properties of QW LEDs, we suggest growing $InN_y(As_{1-x}Sb_x)_{1-y}/Al_zIn_{1-z}As$ QW structures using AlInAs MBLs grown on a GaAs substrate. By growing a relaxed AlInAs MBL on a GaAs substrate heterostructure, we can obtain a desired lattice constant in order to enhance scope for band structure engineering and QW LED design.

In Section 4.2 we present the design procedure for strain-balanced QW structures containing quaternary semiconductors to emit at a desired wavelength. We show that using quaternary alloys opens up a new degree of freedom to design QW LED structures: (i) with a fixed well width, and variable in-plane strain, and (ii) with a fixed in-plane strain, and variable well width.

In Section 4.3, we design strain-balanced $InN_y(As_{1-x}Sb_x)_{1-y}/Al_zIn_{1-z}As$ QW structures grown on an $Al_{0.125}In_{0.875}As$ MBL emitting at $\lambda = 4.2$ μm. We analyse the electronic and optical properties of these devices by analysing their compositions, band offsets, spontaneous emission (SE) spectra, and radiative recombination coefficient B.

In Section 4.4, we seek the possibility of using a different MBL to analyse the effect of MBL composition on the electronic and optical properties of the $InN_y(As_{1-x}Sb_x)_{1-y}/Al_zIn_{1-z}As$ QW LED structures emitting at $\lambda = 4.2$ μm. We discuss the pros and cons of using different MBLs, and provide a design template for designing efficient mid-infrared QW LEDs emitting at $\lambda = 4.2$ μm in Section 4.5. Finally, in Section 4.6 we conclude.

4.1 Routes toward achieving emission beyond 4 μm

We argued in Chapter 3 that should we wish to achieve emission wavelengths beyond 4 μm, nitrogen-free InAsSb/AlInAs QW structures will no longer be appealing, due to the growing compressive in-plane strain in the well making it difficult to grow multiple epitaxial layers. Here, we analyse using dilute nitride $InN_y(As_{1-x}Sb_x)_{1-y}$ wells grown on a relaxed $Al_{0.125}In_{0.875}As$ MBL. Incorporation of a few percent of nitrogen can reduce both the band gap energy [12, 37, 84] and the compressive strain associated with antimony incorporation. The results of this analysis are summarised in Fig. 4.1(a), where dashed black lines and solid red lines respectively denote paths in the composition space along which the in-plane strain ϵ_{xx} and band gap are constant. We note however that the calculations presented in Fig. 4.1(a) are for bulk-like epitaxial $InN_y(As_{1-x}Sb_x)_{1-y}$ layers. When considering QWs the confinement energy – typically ~ 50 meV for the lowest energy bound CB ($e1$) and highest energy bound hole ($h1$) states in full numerical calculations – must be accounted for. Therefore, achieving a desired QW transition energy ($e1 - hh1$) requires growth of $InN_y(As_{1-x}Sb_x)_{1-y}$ QWs having a bulk band gap which is lower by $\sim$ 50 meV, mandating a significant increase in x and y, consequently limiting the accessible wavelength range. In the next section, we explain the design procedure that we employ to achieve strain-balanced $InN_y(As_{1-x}Sb_x)_{1-y}/Al_zIn_{1-z}As$ structures emitting at a fixed wavelength.

The use of a quaternary alloy to form the QW layer(s) of the LED structure provides significant freedom to engineer the band structure, allowing in-plane strain and wavelength to be varied independently. For a desired wavelength λ, this then allows for the growth of an extremely large number of structures having distinct combinations of alloy compositions x and y, in-plane strain ϵ_{xx}, and QW thickness t_w. Fig. 4.1 shows the composition space map of bulk-like $InN_y(As_{1-x}Sb_x)_{1-y}$ with respect to an $Al_{0.125}In_{0.875}As$ MBL. This shows how the bulk band gap energy and the in-plane compressive strain vary with Sb and N composition. The ability to independently vary $\epsilon_{xx,w}$ and λ in quaternary $InN_y(As_{1-x}Sb_x)_{1-y}$ alloys presents significant scope to engineer the band structure, in order to obtain properties suitable for the development of high performance LED devices.

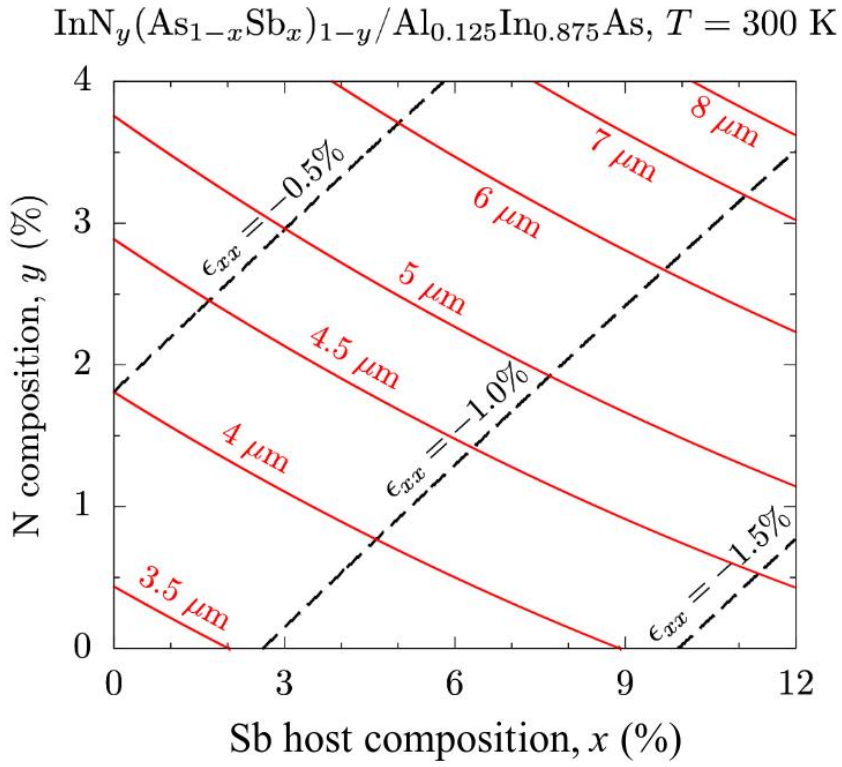


FIGURE 4.1: Composition space map describing the ranges of in-plane strain (ϵ_{xx}) and band gap (at $T = 300$ K) accessible using bulk-like $InN_y(As_{1-x}Sb_x)_{1-y}$ epitaxial layers grown on an $Al_{0.125}In_{0.875}As$ MBL. Dashed black and solid red lines respectively denote paths in the composition space along which ϵ_{xx} and the band gap are constant.

4.2 Design procedure for strain-balanced InNAsSb/AlInAs quantum wells

In Section 3.3 we outlined the importance of strain-balancing in growth of multiple expitaxial layers, and explained the design procedure of strain-balanced ternary InAsSb/AlInAs QW structures. Here, we expand the method decribed in Section 3.3 to provide a design procedure of strain-balanced $InN_y(As_{1-x}Sb_x)_{1-y}/Al_zIn_{1-z}As$ QW structures to emit at a desired wavelength. Using quaternary $InN_y(As_{1-x}Sb_x)_{1-y}$ alloys gives another degree of freedom that enables the band gap and in-plane strain to be selected independently of one another. We use a 10-band **k.p** Hamiltonian described in Section 2.4 to take the effect of nitrogen localised states in the CB into account.

The design procedure of strain-balanced $InN_y(As_{1-x}Sb_x)_{1-y}/Al_zIn_{1-z}As$ structures to emit at a fixed wavelength is as follows:

- Firstly, we define either a fixed thickness t_w and t_b, or a fixed in-plane strain $\epsilon_{xx,w}$.

- Secondly, we find the ratio between x, y, and z satisfying Eq. 3.1.

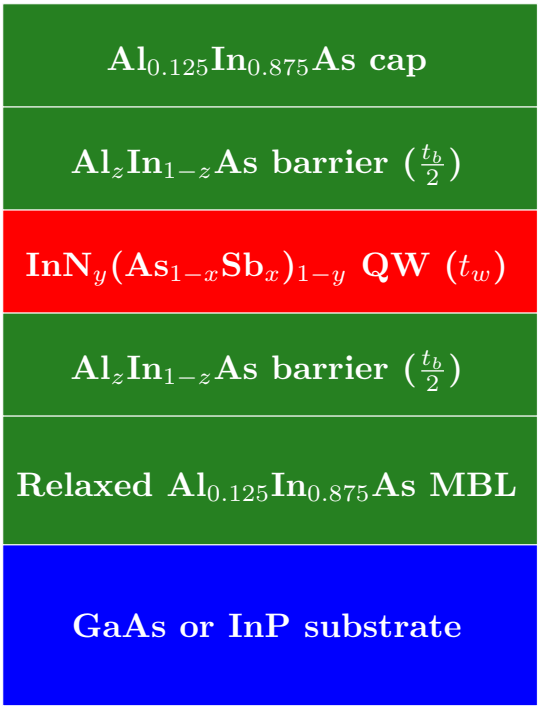


FIGURE 4.2: Schematic illustration of the structures considered to design strain-balanced $InN_y(As_{1-x}Sb_x)_{1-y}/Al_zIn_{1-z}As$ QW LED devices.

- Finally, we vary x and y (and consequently z to satisfy Eq. 3.1) in order to produce a desired QW band gap energy.

Following this procedure, we provide a template for designing strain-balanced quaternary $InN_y(As_{1-x}Sb_x)_{1-y}/Al_zIn_{1-z}As$ QW structures emitting at a fixed wavelength. This model could also be used for designing structures using any given material platform of quaternary III-V semiconductors with any given thickness ratio t_b/t_w. As the sign convention, we note here that throughout this chapter the in-plane strain $\epsilon_{xx} > 0$ and $\epsilon_{xx} < 0$ correspond to tensile and compressive strain, respectively. As we will show, while changing the strain in the QW we can also adjust the QW thickness in order to maintain 4.2 μm emission.

4.3 Design and optimisation of InNAsSb/AlInAs quantum wells for 4.2 μm emission

In this section, we start by designing strain-balanced $InN_y(As_{1-x}Sb_x)_{1-y}/Al_zIn_{1-z}As$ QWs, grown on a relaxed $Al_{0.125}In_{0.875}As$ MBL (c.f. Fig. 4.2) and designed to emit at 4.2 μm. Then, we will discuss and analyse the optoelectronic properties of these structures. As we cannot investigate all possible well and barrier combinations, we must search for optimum LED structures by focusing on key parameters in QW design such as well width and strain. This allows the important trends to be established which can then be applied to other long

wavelength LED structures. In order to analyse the properties of $InN_y(As_{1-x}Sb_x)_{1-y}$ QWs for a given emission wavelength λ, we focus our attention on two structure types. Firstly, in Section 4.3.1 we consider QWs with fixed thickness and variable strain: we choose t_w = 8 nm and vary $\epsilon_{xx,w}$ from 0 to -2.00% by adjusting x and y in the QW to maintain fixed λ. Secondly, in Section 4.3.2 we consider QWs with fixed strain and variable thickness – we choose $\epsilon_{xx,w}$ = -1.5% and vary t_w from 4 to 12 nm, again adjusting x and y to maintain fixed λ. In addition to quantifying key trends in the expected performance, this approach enables us to identify specific LED structures offering optimal performance.

4.3.1 Fixed thickness, variable in-plane strain

Here, we analyse $InN_y(As_{1-x}Sb_x)_{1-y}/Al_zIn_{1-z}As$ QW structures with a fixed well thickness t_w and a fixed barrier thickness t_b with variable in-plane strain $\epsilon_{xx,w}$ in the well and a variable in-plane strain $\epsilon_{xx,b}$ in the barrier. We begin our optimisation by fixing the thickness, t_w = 8 nm, and varying $\epsilon_{xx,w}$ from 0 to -2.00%. For each structure, we have identified the Sb host composition x and the N composition y in the well and the Al composition z in the barrier so that to: (i) produce a desired $\epsilon_{xx,w}$, (ii) satisfy the strain-balancing condition, and (iii) confine the carriers so as to achieve emission at 4.2 μm. We note that the actual Sb composition, $x(1-y)$ is slightly lower than the host composition x, which describes the relative amounts of As and Sb in the $InN_y(As_{1-x}Sb_x)_{1-y}$ QW structure. Fig. 4.3(a) illustrates how x and y vary as the in-plane strain $|\epsilon_{xx,w}|$ changes from 0 to 2.00%. We note a tradeoff between the Sb and N compositions required to achieve 4.2 μm wavelength, which essentially provides more freedom to pick the desired compositions. Sb (N) composition x (y) increases (decreases) by varing in-plane strain in the well $\epsilon_{xx,w}$ from 0 to -2.00% in order to maintain the emitting wavelength at 4.2 μm using a fixed well width t_w of 8 nm. Even though highly strained structures require more Sb host composition x (2.0 - 17.8%) to emit at 4.2 μm, significantly less N composition y (5.33 - 0.19%) is required in highly-strained QW structures. At the same time, Al composition z increases from 12.5 to 20.8% as a function of in-plane strain to maintain the strain-balancing condition in the entire structure. We note that in-plane tensile strain in the barrier $\epsilon_{xx,b}$ varies from 0 to 0.55% as a function of in-plane strain in the well.

As also argued in Chapter 3, it is important to minimise the thermal leakage in type-I QWs by designing structures with favourable CB and VB offsets. The CB and VB offsets of the structures described above are shown in Fig. 4.3(b) as a function of in-plane strain $\epsilon_{xx,w}$. As a function of $\epsilon_{xx,w}$, the CB offset varies from 347 to 164 meV, and the VB offset varies from 91 to 351 meV as a consequence of the changes in material composition and also of the hydrostatic and biaxial strain effects in each structure. Considering a structure with compressively strained wells and tensile strained barriers, the VB offset is calculated as an offset between the HH band edge of the well and LH band edge of the barrier. Another important factor when

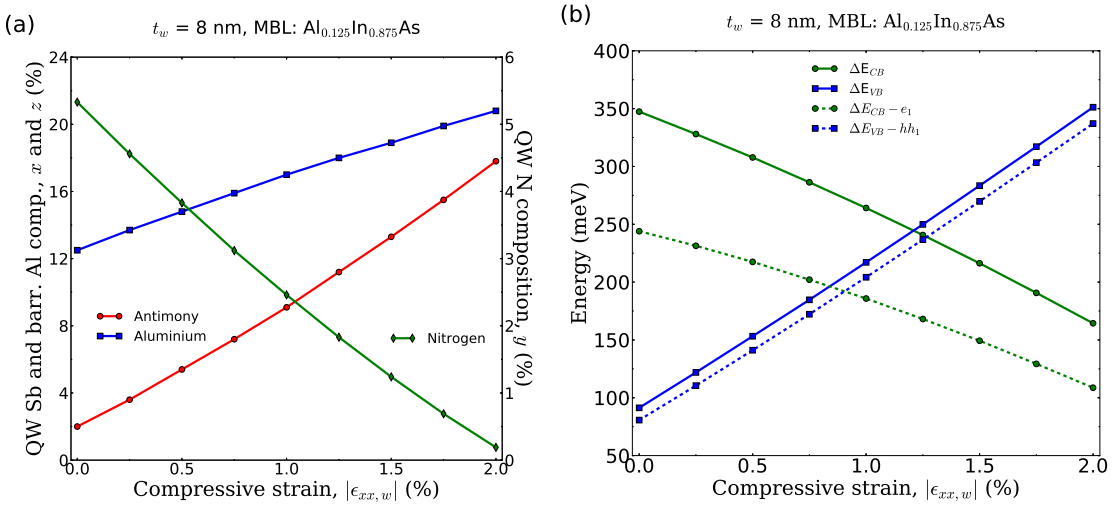


FIGURE 4.3: Summary of calculated electronic properties for $InN_y(As_{1-x}Sb_x)_{1-y}/Al_zIn_{1-z}As$ QW structures grown on an $Al_{0.125}In_{0.875}As$ MBL emitting at $\lambda = 4.2$ μm at T = 300 K. (a) $InN_y(As_xSb_{1-x})_{1-y}$ QW alloy Sb host composition x and N composition y, and $Al_zIn_{1-z}As$ barrier alloy Al composition z required to maintain $\lambda = 4.2$ μm and to satisfy strain-balancing condition as a function of in-plane strain in the well $|\epsilon_{xx,w}|$. (b) Calculated CB and VB offsets and carrier confinement energy as a function of in-plane strain in the well $|\epsilon_{xx,w}|$.

considering carrier thermal leakage in QW LEDs is the carrier confinement energy which defines the difference in energy between the CB (VB) edge of the barrier material and the first electron (hole) energy level. The bigger the carrier confinement energy, the lower the chance of carrier leakage. Green and blue dotted curves in Fig. 4.3(b) denote electron and hole confinement energy in the CB and VB, respectively. With increasing compressive in-plane strain in the well from 0.0% to 2.0%, electron confinement energy in the CB changes from 244 meV to 109 meV; showing a relatively strong carrier confinement. However, one can notice that higher strained structures should be preferred for stronger hole confinement energy in the VB, as this energy increases from 81 meV to 337 meV by increasing $\epsilon_{xx,w}$ from 0.0% to 2.0%.

Having analysed the band offsets and carrier confinement energies in these structures, we now turn our attention to the optical properties of these devices. Fig. 4.4(a) shows the SE spectra at a fixed carrier density as the in-plane strain $\epsilon_{xx,w}$ is increased from 0.0% to 2.0%. As expected, the peak of SE rate at a fixed injected carrier density – $n_{2D} = 10^{11} cm^{-2}$ – increases with increasing $|\epsilon_{xx,w}|$. This is primarily because of the decrement of the effective masses of QW hole states in the plane of the QW as a response to the increasing compressive in-plane strain in the well. This in turn leads to a reduction in the density of states at the VB edge. Therefore, the VB structure changes in such a way that holes occupy states over a smaller range of $\mathbf{k}$. This then makes the overall QW band structure more symmetric about the centre of the band gap, and means that there are more holes available to undergo optical recombination and hence contribute to the SE. As mentioned in Chapter 3, these proposed QW LEDs are for application in gas sensing. A crucial factor when considering sensors is the full width at half maximum

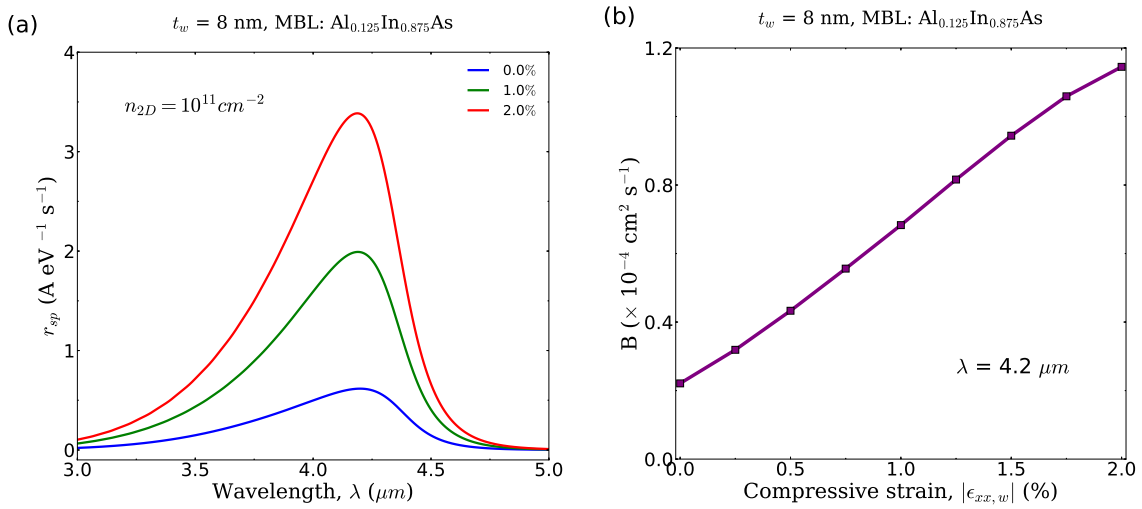


FIGURE 4.4: Summary of calculated optical properties for $InN_y(As_{1-x}Sb_x)_{1-y}/Al_zIn_{1-z}As$ QW structures grown on $Al_{0.125}In_{0.875}As$ MBL emitting at λ = 4.2 μm at T = 300 K. (a) Calculated spontaneous emission spectra at a fixed injected carrier density $n_{2D} = 10^{11} cm^{-2}$. (b) Calculated radiative recombination coefficient B at a fixed injected carrier density $n_{2D} = 10^{11} cm^{-2}$ as a function of compressive in-plane strain in the well $|\epsilon_{xx,w}|$.

(FWHM), which determines the capability of measuring small changes. The narrower the peak of the SE spectra, the better the signal to noise ratio of the device. Comparing the FWHM of the SE spectra of these structures to comparable $Al_xIn_{1-x}Sb$ bulk systems emitting at mid-infrared region [85] we note that the calculated FWHM of the SE spectra is approximately 0.7 μm for the $InN_y(As_{1-x}Sb_x)_{1-y}/Al_zIn_{1-z}As$ QW structures grown on an $Al_{0.125}In_{0.875}As$ MBL, which is significantly smaller than the FWHM of $\cong$1.1 μm observed when using $Al_xIn_{1-x}Sb$ bulk systems.

Fig. 4.4(b) summarises the calculated radiative recombination coefficient B of these 4.2 μm strain-balanced structures. As was done in Chapter 3, the radiative recombination coefficient B has been computed by (i) integrating over the calculated SE spectrum to obtain the radiative current density J_{rad}, and (ii) writing $J_{\text{rad}} = eBn_{2D}^2$ in the Boltzmann approximation. At 4.2 μm we calculate a maximum value $B = 1.14 \times 10^{-4}$ cm^2 s^{-1} for a QW having $|\epsilon_{xx,w}| = 2.0\%$.

4.3.2 Fixed in-plane strain, variable thickness

There are a few different characteristics of 4.2 μm $InN_y(As_{1-x}Sb_x)_{1-y}/Al_zIn_{1-z}As$ QW structures that govern their electronic and optical properties. Having designed these structures with a fixed QW thickness of t_w = 8 nm and in-plane strain in the well $|\epsilon_{xx,w}|$ varying from 0.0 to 2.0%, we now choose an optimum $|\epsilon_{xx,w}|$ to design structures with variable QW thickness. This allows us to engineer these devices electronically and optically by modifying the alloy compositions and well widths to achieve a set of strain-balanced structures emitting at 4.2 μm.

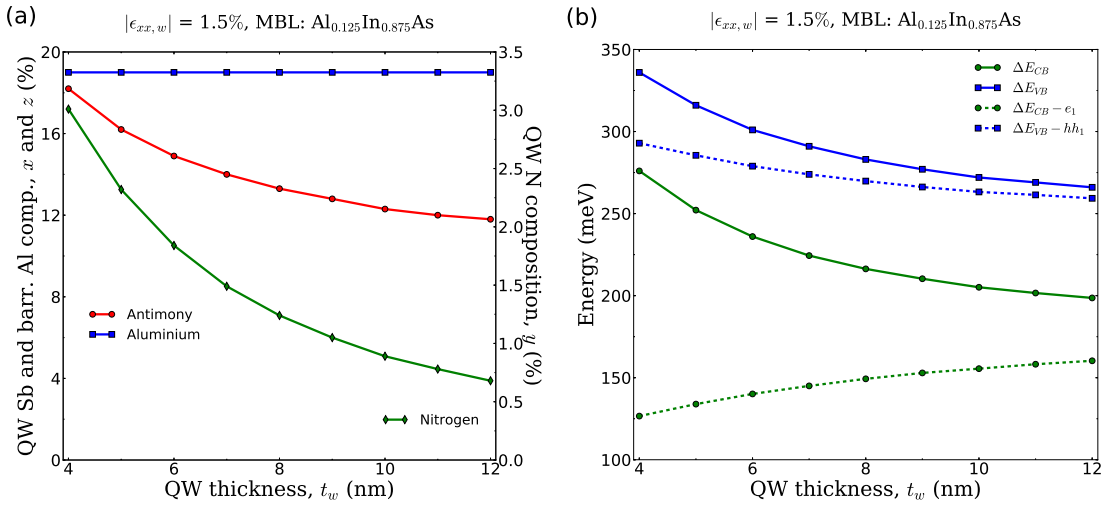


FIGURE 4.5: Summary of calculated electronic properties for $InN_y(As_{1-x}Sb_x)_{1-y}/Al_zIn_{1-z}As$ QW structures grown on $Al_{0.125}In_{0.875}As$ MBL emitting at λ = 4.2 μm at T = 300 K. (a) $InN_y(As_xSb_{1-x})_{1-y}$ QW alloy Sb host composition x and N composition y, and $Al_zIn_{1-z}As$ barrier alloy Al composition z required to maintain λ = 4.2 μm emission and to satisfy strain-balancing condition as a function of QW thickness t_w. (b) Calculated variation of CB and VB offsets and carrier confinement energy with QW thickness t_w.

Here, we have chosen a fixed in-plane strain $\epsilon_{xx,w}$ = -1.5% with a variable QW thickness, ranging from 4 to 12 nm. The selection criteria for the optimum in-plane strain $\epsilon_{xx,w}$ is summarised as follows:

- Structures with lower Sb host composition x and N composition y are easier to grow.

- Structures with higher CB and VB offsets suppress the thermal leakage more effectively.

- The higher the SE rate and the radiative recombination coefficient B, the better the optical efficiency of the device.

We follow the same design procedure as used in Section 4.2. We therefore begin by fixing the in-plane strain in the well, $\epsilon_{xx,w}$ = -1.5%, and vary QW thickness t_w from 4 to 12 nm. For each structure, we identify Sb host composition x and N composition y in the well and Al composition z in the barrier in order to: (i) produce a desired $\epsilon_{xx,w}$ = -1.5%, (ii) satisfy the strain-balancing condition, and (iii) confine the carriers so as to achieve emission at 4.2 μm.

Figure 4.5(a) depicts the calculated Al, Sb and N alloy compositions required for strain-balanced $InN_y(As_xSb_{1-x})_{1-y}/Al_zIn_{1-z}As$ QW LED structures on an $Al_{0.125}In_{0.875}As$ MBL emitting at λ = 4.2 μm at T = 300 K. Having a fixed compressive in-plane strain in the well mandates a fixed tensile in-plane strain in the barrier to satisfy the strain-balancing condition. In this regard, the Al composition z remains constant (= 19%) as a function of QW thickness t_w. The wider the QW thickness t_w, the smaller the value of e_1 and hh_1; therefore, Sb host composition x

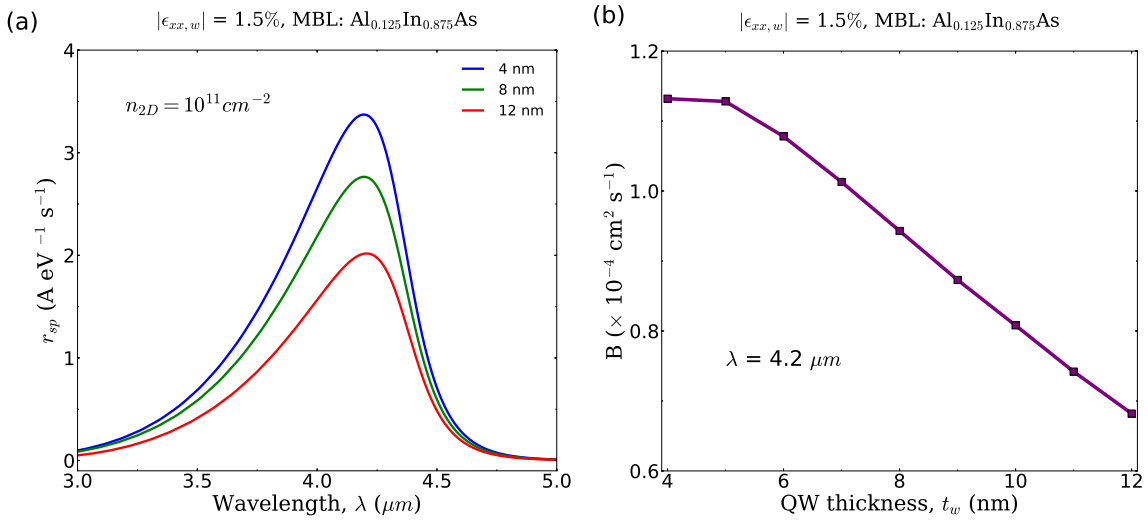


FIGURE 4.6: Summary of calculated optical properties for $InN_y(As_{1-x}Sb_x)_{1-y}/Al_zIn_{1-z}As$ QW structures grown on an $Al_{0.125}In_{0.875}As$ MBL emitting at $\lambda = 4.2$ μm at T = 300 K. (a) Calculated spontaneous emission spectra at a fixed injected carrier density $n_{2D} = 10^{11} cm^{-2}$. (b) Calculated radiative recombination coefficient B at a fixed injected carrier density $n_{2D} = 10^{11} cm^{-2}$ as a function of QW thickness t_w.

and N composition y in the well both decrease as QW thickness t_w increases: x (y) varies from 18.2% (3.01%) to 11.8% (0.68%) by varying t_w from 4 to 12 nm.

The CB and VB offsets of these structures are shown in Fig. 4.5(b). QW structures with higher band offsets suppress the thermal leakage more effectively. As mentioned above, the barrier composition $Al_zIn_{1-z}As$ remains constant in the structures with a fixed in-plane strain. Hence the CB and VB offsets are only functions of Sb host composition x and N composition y in the $InN_y(As_xSb_{1-x})_{1-y}$ well. Therefore, as a consequence of the smaller x and y required in wider structures, both CB and VB offsets decrease by increasing the QW thickness t_w. The CB offset varies from 276 to 199 meV. The VB offset is calculated as the offset between the HH band edge in the well and the LH band edge in the barrier, varying from 336 to 266 meV. The calculated band offsets look promising to help the carrier states to be confined strongly and therby minimise thermal leakage of electrons and holes from the CB and VB, respectively. We have assessed this by studying the carrier confinement energies $\Delta E_{CB} - e_1$ and $\Delta E_{VB} - hh_1$. The green and blue dotted curves in Fig. 4.5(b) denote electron and hole confinement energy in the CB and VB, respectively. With increasing QW thickness from 4 to 12 nm, electron confinement in the CB increases from 127 meV to 160 meV. Stronger hole confinement energies in the VB are witnessed in structures with narrower QW thickness, though the difference in this energy is not significant when varying t_w from 4 to 12 nm; decreasing from 293 meV to 259 meV.

Turning our attention to the optical properties of these devices, we next calculate the SE spectra and radiative current density of these structures at a fixed injected carrier density.

Fig. 4.6(a) shows the calculated SE spectra of three of the structures discussed above with t_w = 4, 8, 12 nm. As discussed in Section 4.3.1, we expect the peak SE rate at a fixed injected carrier density – $n_{2D} = 10^{11} cm^{-2}$ – to decrease in structures with a larger density of states at the VB maximum, which consequently have less carriers available to undergo optical recombination. The energy separation between the higher confined hole states decreases as the well width increases, and the VB edge effective mass also increases with reducing confined state separation. As a consequence, the peak of the SE rate drops from 3.4 $A\ eV^{-1}\ s^{-1}$ in the narrowest structure with t_w = 4 nm to 2.0 $A\ eV^{-1}\ s^{-1}$ in the widest structure having t_w = 12 nm.

At a fixed injected carrier density $n_{2D} = 10^{11} cm^{-2}$, we expect the 2D radiative coefficient B to decrease in structures with wider QWs. The calculated radiative coefficient B is also depicted in Fig. 4.6(b) – dropping from 1.13 $\times$ 10^{-4} cm^2 s^{-1} in the narrowest structure with t_w = 4 nm to 0.68 $\times$ 10^{-4} cm^2 s^{-1} in the widest structure having t_w = 12 nm.

4.4 Possibility of using a different metamorphic buffer layer

Given the large band offsets observed for an $Al_{0.125}In_{0.875}As$ MBL, we consider now the potential to use a MBL with a different composition, closer to that of InAs. This change in MBL will reduce the Al content in the barrier layer at fixed strain, hence reducing the barrier band gap energy, however barrier heights will then reduce e_1 for electrons and hh_1 holes in the QW, so that 4.2 μm emission may then be achieved using a QW layer with larger bulk energy gap and hence lower Sb and N composition for a fixed well width and strain value. We choose a MBL composition of $Al_{0.06}In_{0.94}As$ for this investigation. We analyse the electronic and optical properties of the strain-balanced $InN_y(As_{1-x}Sb_x)_{1-y}/Al_zIn_{1-z}As$ QW structures grown on this MBL in order to seek the potential of reducing the MBL aluminium composition. We will conclude this section by a comparison between the structures considered in Sections 4.3.1 and 4.3.2 and those considered her in Sections 4.4.1 and 4.4.2, discussing the pros and cons of using MBLs with different compositions with regards to the electronic and optical properties of the proposed structures.

The strain-balanced $InN_y(As_{1-x}Sb_x)_{1-y}/Al_zIn_{1-z}As$ QW structures considered in Sections 4.3.1 and 4.3.2 were designed with respect to an $Al_{0.125}In_{0.875}As$ MBL – from now on, we will refer to this as MBL1 – with a lattice constant of 6.0087 Å. These structures require N composition y in a range of 0.19% to 5.33% for designing strain-balanced $InN_y(As_{1-x}Sb_x)_{1-y}/Al_zIn_{1-z}As$ QW structures emitting at 4.2 μm. Practically, structures with less Sb and N composition are more favourable to grow. Therefore, we assess here the potential of using an $Al_{0.06}In_{0.94}As$ MBL with a lattice constant of 6.0345 Å – we refer to this as MBL2 below. We investigate the extent to

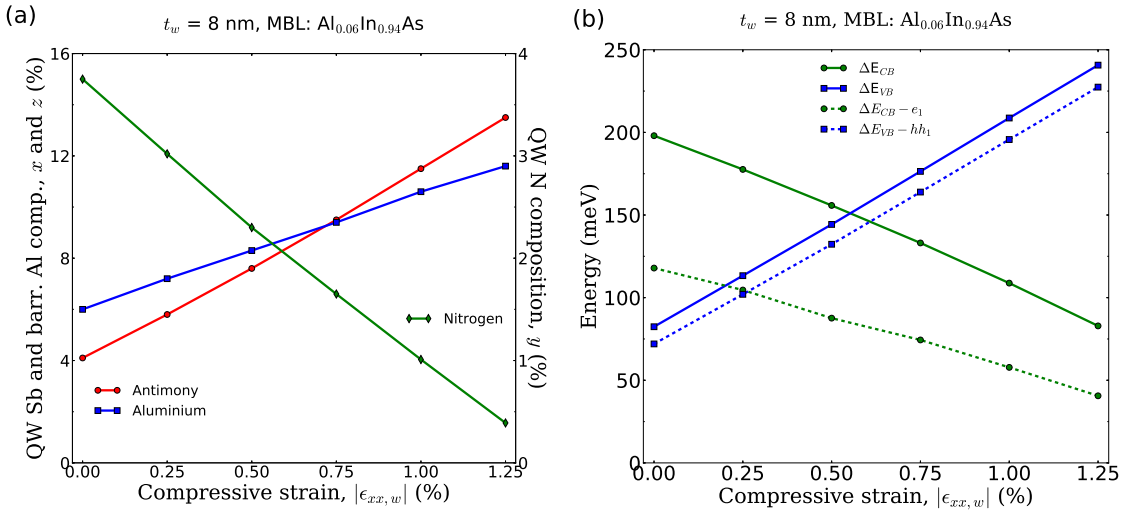


FIGURE 4.7: Summary of calculated electronic properties for $InN_y(As_{1-x}Sb_x)_{1-y}/Al_zIn_{1-z}As$ QW structures grown on $Al_{0.06}In_{0.94}As$ MBL emitting at $\lambda = 4.2$ μm at T = 300 K. (a) $InN_y(As_{1-x}Sb_x)_{1-y}$ QW alloy Sb host composition x and N composition y, and $Al_zIn_{1-z}As$ barrier alloy Al composition z required to maintain $\lambda = 4.2$ μm and to satisfy strain-balancing condition as a function of in-plane strain in the well $|\epsilon_{xx,w}|$. (b) Calculated CB and VB offsets and carrier confinement energy as a function of in-plane strain in the well $|\epsilon_{xx,w}|$.

which it may allow reduced N and Sb composition in a strain-balanced QW structure emitting at 4.2 μm, and whether such structures bring any benefit for the overall optical properties.

4.4.1 Fixed thickness, variable in-plane strain

Here, we analyse $InN_y(As_{1-x}Sb_x)_{1-y}/Al_zIn_{1-z}As$ QW structures with a fixed well thickness t_w and a fixed barrier thickness t_b with variable in-plane strain $\epsilon_{xx,w}$ in the well and a variable in-plane strain $\epsilon_{xx,b}$ in the barrier. Again, we consider the thickness ratio $t_b = 3t_w$. We begin our optimisation by fixing the thickness, $t_w = 8$ nm, and varying $\epsilon_{xx,w}$ from 0% to a maximum possible value while satisfying the strain-balancing condition and emitting at $\lambda = 4.2$ μm. Using MBL2 for fixed thickness, variable in-plane strain structures may limit the achievable in-plane strain in the well due to MBL2 having a larger lattice constant than MBL1. As was done in Section 4.3.1, for each structure, we identify the Sb host composition x and the N composition y in the well and the Al composition z in the barrier in order to: (i) produce a desired $\epsilon_{xx,w}$, (ii) satisfy the strain-balancing condition, and (iii) confine the carriers so as to achieve emission at 4.2 μm.

The variation of x and y with in-plane strain $|\epsilon_{xx,w}|$ is depicted in Fig. 4.7(a). Analysing the composition variation of $InN_y(As_{1-x}Sb_x)_{1-y}/Al_zIn_{1-z}As$ QW structures grown on MBL2, we note that the maximum achievable $\epsilon_{xx,w}$ for a well width of 8 nm is -1.41%, with $x = 14.8\%$, $y = 0.0\%$, and $z = 12.2\%$. We consider here the structures with $0.0\% \leqslant |\epsilon_{xx,w}| \leqslant 1.25\%$ with steps of 0.25%. There is again a tradeoff between the Sb and N compositions required to achieve

4.2 μm wavelength using MBL2. Using a fixed well width t_w of 8 nm, Sb (N) composition x (y) increases (decreases) by varying in-plane strain in the well $\epsilon_{xx,w}$ from 0 to -1.25% nm in order to maintain the emission at λ = 4.2 μm. As strain is increased, we require larger Sb host composition x (4.1 - 13.5%) to emit at 4.2 μm, but this will lead to requiring significantly lower N composition y (3.75 - 0.39%) in higher-strained QW structures. In addition, the Al composition z increases from 6.0 to 11.6% as a function of in-plane strain to satisfy the strain-balancing condition in the entire structure. It is worth noting that the in-plane tensile strain in the barrier $\epsilon_{xx,b}$ ranges from 0 to 0.37% as a function of the in-plane strain in the well.

Due to the effects of the compressive in-plane strain in the well and the tensile in-plane strain in the barrier, the VB offset in these structures is calculated as the offset between the HH band edge in the well and the LH band edge in the barrier. The CB and VB offsets of these QW structures with respect to the $Al_{0.06}In_{0.94}As$ MBL are shown in Fig. 4.7(b) as a function of in-plane strain $\epsilon_{xx,w}$. By varying $|\epsilon_{xx,w}|$ from 0 to 1.25%, the CB offset decreases from 198 to 83 meV, and the VB offset increases from 82 to 241 meV. Green and blue dotted curves in Fig. 4.7(b) denote electron and hole confinement energy in the CB and VB, respectively. With increasing compressive in-plane strain in the well from 0.0% to 1.25%, electron confinement energy in the CB decreases from 118 meV to 41 meV; showing stronger carrier confinement in structures with lower compressive in-plane strain in the well. However, one can notice that highly strained structures produce stronger hole confinement energy, with the hole confinement exceeding electron confinement for $|\epsilon_{xx,w}|$ >0.25%.

Turning our attention to the optical properties of these devices, we next calculate the SE spectra and radiative coefficient B of these QW LED devices. Fig. 4.8(a) depicts the SE spectra at a fixed carrier density for selected strain values. Highly-strained structures have less hole effective mass, mandating the density of states close to the VB edge to diminish. Hence, holes occupy states over a smaller range of $\mathbf{k}$ in the VB, meaning that more holes are available to participate in optical recombination. The peak of the SE rate at a fixed injected carrier density – $n_{2D} = 10^{11} cm^{-2}$ – increases with increasing $|\epsilon_{xx,w}|$ from 0.0 to 1.25%. However the peak rate for 1% strain ($\sim$ 1.4 A eV^{-1} s^{-1}) is lower than that for 1% strain in MBL1 ($\sim$ 2 A eV^{-1} s^{-1}); c.f. Fig. 4.4(a). This reduction arises due to the weaker electron confinement in the QW in MBL2 – which is primarily associated with the smaller CB and VB offsets compared to the structures grown on MBL1, reducing both the elctron-hole overlap and also allowing electron spill over from the well to barrier layer.

Fig. 4.8(b) summarises the calculated radiative recombination coefficient B of these 4.2 μm strain-balanced structures. At 4.2 μm we calculate a maximum value $B = 0.49 \times 10^{-4}$ cm^2 s^{-1} for a QW with $|\epsilon_{xx,w}| = 1.25\%$, again reduced compared to the value of $B = 0.82 \times 10^{-4}$ cm^2 s^{-1} for $|\epsilon_{xx,w}| = 1.25\%$ in Fig. 4.4(b) (MBL1).

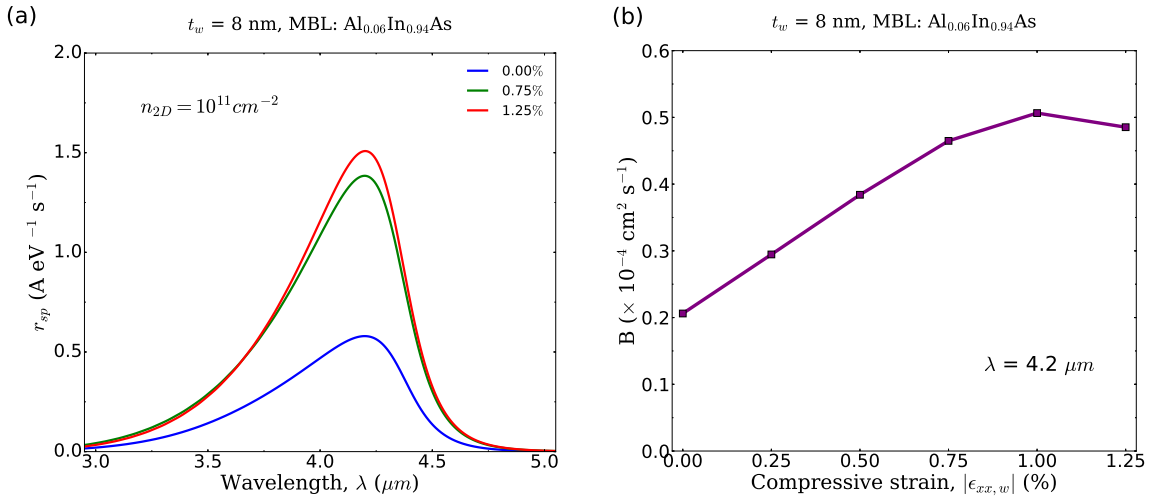


FIGURE 4.8: Summary of calculated optical properties for $InN_y(As_{1-x}Sb_x)_{1-y}/Al_zIn_{1-z}As$ QW structures grown on $Al_{0.06}In_{0.94}As$ MBL emitting at λ = 4.2 μm at T = 300 K. (a) Calculated spontaneous emission spectra at a fixed injected carrier density $n_{2D} = 10^{11} cm^{-2}$. (b) Calculated radiative recombination coefficient B at a fixed injected carrier density $n_{2D} = 10^{11} cm^{-2}$ as a function of compressive in-plane strain in the well $|\epsilon_{xx,w}|$.

4.4.2 Fixed in-plane strain, variable thickness

Here, we have chosen a fixed in-plane strain $\epsilon_{xx,w}$ = -1.0% with a variable QW thickness ranging from 4 to 12 nm. We have used the selection criteria as outlined in Section 4.3.2 in order to find the optimum in-plane strain $\epsilon_{xx,w}$. For each structure, we have identified Sb host composition x and N composition y in the well and Al composition z in the barrier so as to: (i) produce a desired $\epsilon_{xx,w}$ = -1.0%, (ii) satisfy the strain-balancing condition, and (iii) confine the carriers so as to obtain the peak of the SE spectra at λ = 4.2 μm.

Fig. 4.9(a) summarises the calculated alloy compositions in the well and in the barrier required to design strain-balanced $InN_y(As_{1-x}Sb_x)_{1-y}/Al_zIn_{1-z}As$ QW structures emitting at λ = 4.2 μm on MBL2 at T = 300 K. The Al composition z remains constant (= 10.6%) as a function of QW thickness t_w. Carrier confinement is stronger in wider structures. Therefore, the Sb host composition x and N composition y in the well both decrease as QW thickness t_w increases: x (y) varies from 14.6% (2.14%) to 10.4% (0.59%) by varying t_w from 4 to 12 nm.

The calculated CB and VB offsets of these structures are summarised in Fig. 4.9(b). QW structures with higher band offsets suppress the thermal leakage more effectively. Barrier composition $Al_zIn_{1-z}As$ remains constant in the structures with a fixed in-plane strain. Therefore the CB and VB offsets only depend on Sb host composition x and N composition y in the $InN_y(As_{1-x}Sb_x)_{1-y}$ well. Both the CB and VB offsets decrease by increasing the QW thickness t_w due to the less x and y required in wider structures. The CB offset varies from 145 to 96 meV. The VB offset is again calculated as an offset between the HH band edge in the well and the LH band edge in the barrier: varying from 243 to 195 meV. As also shown in Fig. 4.9(b),

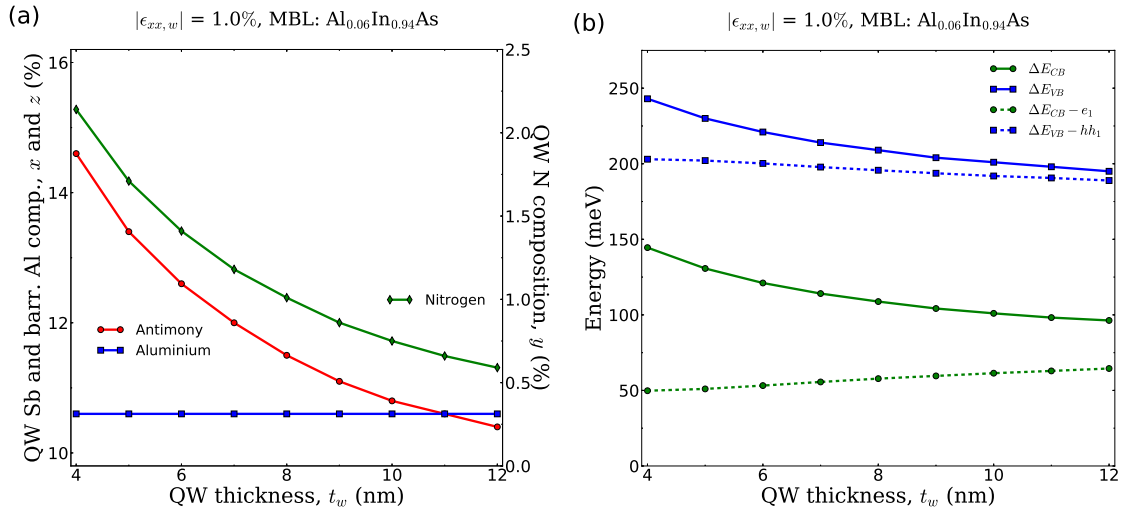


FIGURE 4.9: Summary of calculated electronic properties for 1% strained $InN_y(As_{1-x}Sb_x)_{1-y}/Al_zIn_{1-z}As$ QW structures grown on $Al_{0.06}In_{0.94}As$ MBL emitting at $\lambda = 4.2$ μm at T = 300 K. (a) $InN_y(As_{1-x}Sb_x)_{1-y}$ QW alloy Sb host composition x and N composition y, and $Al_zIn_{1-z}As$ barrier alloy Al composition z required to maintain $\lambda = 4.2$ μm emission and to satisfy strain-balancing condition as a function of QW thickness t_w. (b) Calculated variation of CB and VB offsets and carrier confinement energy with QW thickness t_w.

while the electron confinement energy, $\Delta E_{CB} - e_1$, increases from 50 meV to 65 meV with increasing QW thickness, the hole confinement energy has an opposite trend; decreasing from 203 meV to 189 meV. Given the sufficiently large hole confinement energy in these structures, the priority when choosing an optimal structure is then to go with structures with wider QW thickness, delivering a higher electron confinement energy.

We now turn our attention to analysing the optical properties of these devices. Fig. 4.10(a) shows the calculated SE spectra of three of the structures discussed above with t_w = 4, 8, 12 nm. Once again, the peak of the SE rate with a fixed injected carrier density – $n_{2D} = 10^{11} cm^{-2}$ – increases in narrower QWs. The peak of the SE rate drops from 2.09 $A\ eV^{-1}\ s^{-1}$ in the narrowest structure with t_w = 4 nm to 1.14 $A\ eV^{-1}\ s^{-1}$ in the widest structure with t_w = 12 nm.

Likewise, the radiative coefficient B at a fixed injected carrier density $n_{2D} = 10^{11} cm^{-2}$ decreases in wider structures that contain less Sb host composition x. The calculated radiative coefficient B is shown in Fig. 4.10(b) – dropping from 0.78 $\times$ 10^{-4} cm^2 s^{-1} in the narrowest structure with t_w = 4 nm to 0.17 $\times$ 10^{-4} cm^2 s^{-1} in the widest structure having t_w = 12 nm.

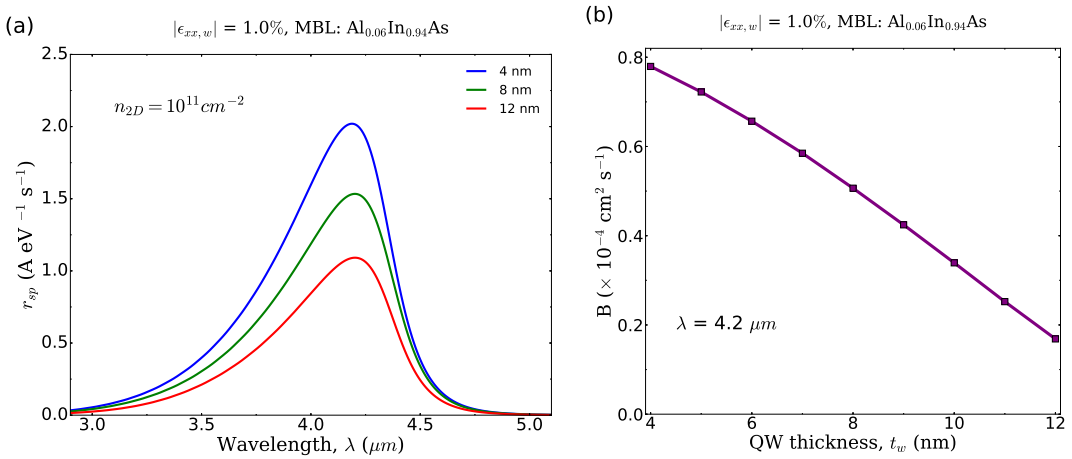


FIGURE 4.10: Summary of calculated optical properties for $InN_y(As_{1-x}Sb_x)_{1-y}/Al_zIn_{1-z}As$ QW structures grown on $Al_{0.06}In_{0.94}As$ MBL emitting at λ = 4.2 μm at T = 300 K. (a) Calculated spontaneous emission spectra at a fixed injected carrier density $n_{2D} = 10^{11} cm^{-2}$. (b) Calculated radiative recombination coefficient B at a fixed injected carrier density $n_{2D} = 10^{11} cm^{-2}$ as a function of QW thickness t_w.

4.5 Design criteria for optimum quantum well light emitting diode emitting at 4.2 μm

In Sections 4.3 and 4.4 we investigated a series of strain-balanced $InN_y(As_{1-x}Sb_x)_{1-y}/Al_zIn_{1-z}As$ QW LED structures emitting at λ = 4.2 μm. We argued that there are several electronic and optical characteristics of QW LEDs that govern the performance of the device. Here, we discuss different aspects of these devices while using MBL1 or MBL2 as the MBL on top of which the structures are grown.

QW thickness and alloy composition:

The improved carier confinement in wider wells allows the use of lower antimony and nitrogen contents to deliver λ = 4.2 μm emission. This also leads to a reduced level of compressive in-plane strain in the well which is favourable from a growth point of view. Given the larger lattice constant of MBL2 compared to MBL1, using MBL2 also allows the use of less antimony and nitrogen contents in the well to obtain emission at 4.2 μm (c.f. Fig. 4.9(a)). Also, by using MBL2, the optimised in-plane strain in the well $\epsilon_{xx,w}$ drops to -1.0% (using MBL1 requires $\epsilon_{xx,w}$ = -1.5%, as shown in Fig. 4.5(a)); which in turn produces a lower strain-thickness product. Hence, growth considerations tend to favour MBL2 and wider wells.

Carrier confinement energy:

Although holes are more strongly confined in QW structures with narrower QW thickness at a fixed compressive in-plane strain, wider structures deliver a better confinement energy of

electrons at a fixed compressive in-plane strain using either MBL1 or MBL2 (c.f. Figures 4.5(b) and 4.9(b)). Nevertheless, MBL1 allows for good electron confinement across the full range of well widths studied, with the electron confinement energy increasing from 127 meV to 160 meV as the well width increases from 4 nm to 12 nm. Electron confinement is weaker for all well widths considered for MBL2, increasing from 50 meV to only 65 meV, as the width increases from 4 nm to 12 nm. The holes are generally very well confined in all structures considered on both MBL1 (ranging from 293 to 259 meV by increasing the well width) and MBL2 (ranging from 203 to 189 meV by increasing the well width). Overall carrier confinement considerations look to favour MBL1 over MBL2. This conclusion is further confirmed when we next consider the SE rate for the deifferent structures considered.

Spontaneous emission rate and radiative current density:

Choosing a fixed in-plane strain in the well, narrower structures tend to have a higher peak of spontaneous emission rate, and subsequently a higher radiative recombination coefficient B. Higher SE rate and radiative current density are found in the structures grown on MBL1 (c.f. Fig. 4.6), showing an increase of ∼45% compared to the structures grown on MBL2 (c.f. Fig. 4.10).

Considering all of the above characteristics, there is apparently a tradeoff while trying to choose the optimal QW LED structures since some of the characteristics are optimised in the narrower wells, and some are optimised in the wider wells. Nevertheless, when choosing a fixed compressive in-plane strain in the well, we conclude that structures with QW thickness t_w from 6 to 10 nm exhibit a good balance of different electronic and optical properties, while also allowing to have a reduced Sb and N composition compared to the narrowest structures. All in all, although using MBL2 is more favourable in terms of requiring significantly less antimony and nitrogen content in the well to achieve $\lambda = 4.2$ μm emission, but this comes at the expense of smaller band offsets and carrier confinement energy as well as weaker optical performance of the devices. Therefore, we conclude that structures grown on MBL1 deliver a better balance of the electronic and optical properties.

4.6 Summary and conclusions

In this chapter we have presented a theoretical investigation to guide optimisation of the optical properties of 4.2 μm InNAsSb QWs grown on AlInAs MBLs. Analysing the bulk composition space map of this material system, we have argued that using dilute nitride $InN_y(As_{1-x}Sb_x)_{1-y}$ is critical to achieve emission beyond 4 μm. By quantifying the scope offered by this material system to use strain and band structure engineering we demonstrated that there is large scope for the design of QW structures, incorporating compressively strained quaternary

$InN_y(As_{1-x}Sb_x)_{1-y}$ QWs having tensile strained ternary $Al_zIn_{1-z}As$ barriers. Such QWs can combine large type-I band offsets with emission wavelengths ~ 4.2 μm, offering the possibility to design devices having high optical efficiency and reduced temperature sensitivity, and making these structures specifically appealing for the development of mid-infrared light emitters.

We have presented design criteria to achieve strain-balanced quaternary QWs at a desired emission wavelength, thereby providing a general method which can be applied to produce candidate multi-QW or superlattice structures for epitaxial growth and experimental investigation. Via a systematic analysis of strain-balanced structures designed to emit at 4.2 μm we identified key trends in their properties and performance as functions of alloy composition, QW thickness and epitaxial strain, while considering growth on two different metamorphic buffer layers.

Overall, our theoretical analysis has identified important trends in the performance of GaAs-based metamorphic quantum well light emitting diodes operating at $\lambda = 4.2$ μm, providing guidelines for the growth of optimised devices suitable for practical applications, and pointing to the promise of these novel metamorphic heterostructures for the development of high-performance mid-infrared light emitting sources.

Chapter 5

Band structure engineering of type-II $GaAs_{1-x}Sb_x$/GaAs quantum rings for intermediate band solar cells

A Quantum Ring (QR) is a term describing a doubly-connected nanostructure of ring-like shape. Charge carriers in QRs experience unusual density of states, and display novel physical properties which differ significantly from singly-connected nanostructures, e.g. quantum dots [86–88]. In this chapter we focus on results of modelling type-II $GaAs_{1-x}Sb_x$/GaAs QRs to study their electronic band structure in order to design and optimise intermediate band solar cells (IBSCs).

We begin with an introduction and an overview of past related works in Section 5.1. In Sec. 5.2, using an analytical analysis – based on a solution of the time-independent Schrödinger equation for a cylindrical QR of infinite potential depth – we highlight that the QR geometry offers significant flexibility, compared to the conventional quantum dot (QD) geometry, to engineer the valence band (VB) structure of $GaAs_{1-x}Sb_x$/GaAs structures for IBSC applications. Our numerical calculations in Sec. 5.3 – based on a multi-band $\mathbf{k}\cdot\mathbf{p}$ Hamiltonian, and including full strain and piezoelectric effects – corroborate this finding. We highlight that type-II $GaAs_{1-x}Sb_x$/GaAs QRs [89–92] are ideally suited to IBSC applications, due not only to their radiative lifetimes, but also due to their large VB offsets, which can be expected to mitigate thermionic emission of holes from the intermediate band (IB). In Sec. 5.4, we undertake a numerical optimisation of the QR morphology, by varying the QR dimensions and alloy composition, to identify structures which allow to achieve optimum IB energy so as to maximise

IBSC efficiency. Our results confirm the potential of $GaAs_{1-x}Sb_x/GaAs$ QRs for IBSC applications, and provide guidelines for the growth of suitable structures for prototype IBSCs. Finally, we conclude in Sec. 5.5.

5.1 Intermediate band solar cells

Nowadays the sustainable energies are of most importance. Solar cells as photovoltaic systems which can generate electrical energy from solar radiation have become the most popular devices in the field of using sustainable energies [93]. Conventional single-energy-gap solar cells have an ultimate efficiency limit that was established by Shockley and Queisser on the basis of detailed balance arguments [94]. The limited efficiency of these single-energy-gap solar cells is primarily due to two opposing fundamental processes – absorption and emission, and also that only photons with an energy close to that of the semiconductor band gap are effectively converted [95]. Due to their potential to significantly exceed the single-junction Shockley-Queisser (detailed balance) photovoltaic efficiency limit, IBSCs constitute a promising approach towards developing next-generation solar cells [96, 97]. This is achieved via introduction of an IB lying energetically within the band gap of a host matrix semiconductor. In the case that the IB is electrically isolated from both the VB and conduction band (CB) of the host matrix semiconductor – via gaps in the density of states – carrier generation due to absorption of photons having energy less than the band gap $E_{\mathrm{G}} = E_{\mathrm{CB}} - E_{\mathrm{VB}}$ of the host matrix semiconductor can occur via two-step photon absorption (TSPA).

There are two processes involved in a generic hole-based IB material as illustrated in Fig. 5.1. Process (I) consists of electron-hole pair generation via the absorption of two subband gap photons, one of them with E > E_L (pumping one electron from the VB to the IB) and the other with E > E_H, pumping one electron (not necessarily the same one) from the IB to the CB. The idea of this two-photon mechanism for harvesting subband gap photons and increasing the conversion efficiency of solar cells was first proposed in Ref. [96], after which the conversion efficiency of an ideal system was calculated in Refs. [98–100]. In process (II), one photon has energy above the band gap energy (E > E_G) while the second one exhibits subband gap energy (E > E_L). Through the absorption of the above-band-gap photon, an electron-hole pair is created. In a hole-based IBSC, TSPA proceeds via (i) an electron in the IB being promoted to the CB via absorption of a sub-band gap photon having energy $E_{\mathrm{H}} = E_{\mathrm{CB}} - E_{\mathrm{IB}}$, and (ii) subsequent promotion of the resulting IB hole to the VB via the absorption of a second sub-band gap photon having energy $E_{\mathrm{L}} = E_{\mathrm{IB}} - E_{\mathrm{VB}}$. The presence of the IB therefore enhances the photocurrent generated by a single-junction solar cell at fixed illumination, by allowing absorption of photons having energy $< E_{\mathrm{G}}$, while the electrical isolation of the IB from the host matrix CB and VB ensures that the open-circuit voltage V_{OC} is determined by E_{G} rather than being limited by the sub-band gap energies E_{L} and E_{H} [96, 101].

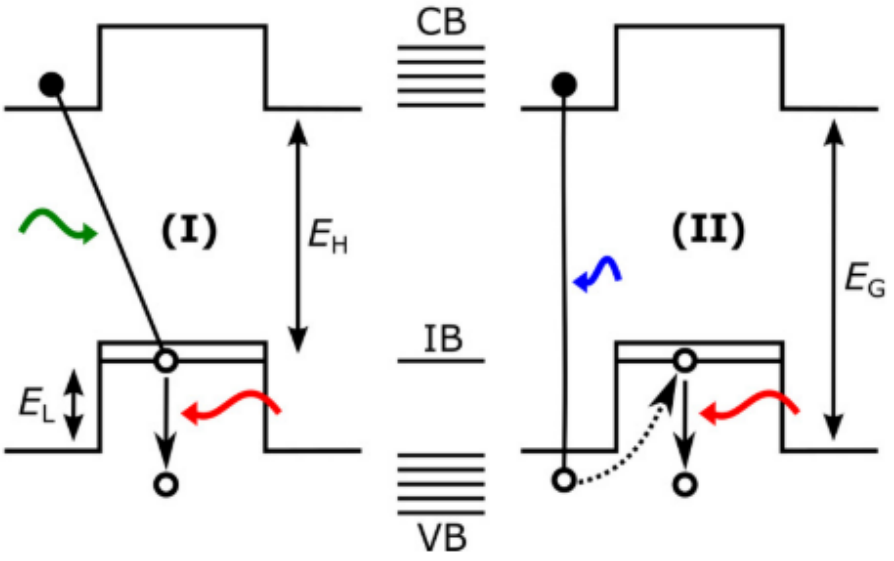


FIGURE 5.1: A schematic of a hole-based intermediate band solar cell. In process (I) one photon pumps an electron from the IB to the CB and, subsequently, a hole confined in the IB is pumped by another photon to the VB. In process (II) one electron-hole pair is created by one photon. The hole relaxes into the less energetic IB and is subsequently pumped back into the VB by a second photon [102].

Due to their promise of high efficiency – with a predicted detailed balance limit of 63.8% under concentrated illumination [96, 97, 101] – IBSCs have attracted significant research interest. We consider the following assumptions when realising ideal IBSCs [96]:

- Nonradiative transitions between any two of the three bands are forbidden.

- Carrier mobilities are infinite.

- Ohmic contacts are applied so that only electrons (holes) can be extracted from the conduction (valence) band to form the external current.

- No carrier can be extracted from the impurity band.

- The cell is thick enough so that the photons with enough energy to induce any one of the transitions described above are absobed.

- A perfect mirror is located at the back of the cell (and elsewhere) so that the radiation generated in the cell can only escape by the front area of illumination.

- The incident light is isotropic. This is achieved by using an ideal concentrator – of zero absorptance – that sends the luminescent photons escaping from the cell to somewhere inside the solar cell.

Despite the simplicity of the elemental concepts, practical realisation of IBSCs has proved extremely challenging [97, 103]. Practical efforts to realise IBSCs have to date focused primarily on two approaches to introduce an IB into the band gap of a host matrix semiconductor, relying on (i) a bound electron or hole ground state in a three-dimensional quantum confined heterostructure possessing a discrete density of states, e.g. in a QD, or (ii) an IB formed via incorporation of a small concentration of a substitutional impurity, e.g. in a highly-mismatched alloy (HMA) such as dilute nitride $GaN_xAs_yP_{1-x-y}$ [104]. The performance of QD-IBSCs has been limited by a combination of poor sub-band gap absorption, which limits short-circuit current density J_{SC}, and short radiative lifetimes τ_{rad} for carriers occupying IB states, resulting in loss of carriers from the IB via radiative recombination and consequently reducing V_{OC} [97]. Likewise, the presence of insufficiently large band offsets in QDs can lead to loss of carriers via thermionic emission (e.g. from the IB to CB in an electron-based QD-IBSC) [105]. The use of localised impurity states in HMA-IBSCs also introduces fundamental issues, increasing losses associated with non-radiative (Shockley-Read-Hall) recombination of carriers occupying IB states at defect sites, and thereby limiting carrier extraction and degrading overall efficiency of the device.

As a result, research studies to realise IBSCs have increasingly shifted away from conventional platforms such as type-I QDs, and towards novel materials and heterostructures whose electronic and optical properties offer the potential to overcome the aforementioned limitations. In particular, there is increasing interest in heterostructures having type-II band alignment [106–109], due to their potential to suppress radiative losses as a consequence of the intrinsically large radiative lifetimes associated with their bound eigenstates (resulting from reduced electron-hole spatial overlaps) [110, 111], as well as reduced intra-band carrier relaxation via non-radiative (Auger) recombination [112, 113]. One such class of novel heterostructures are type-II $GaAs_{1-x}Sb_x/GaAs$ quantum rings (QRs). These hole-based IBSCs – in which the IB is formed by the highest energy bound hole eigenstate in the QR – have attracted increasing attention due not only to their type-II band alignment, but also to their large band offsets, which are expected to mitigate carrier loss via thermionic emission from the IB. Experimental analysis of prototype type-II $GaAs_{1-x}Sb_x/GaAs$ QR-IBSCs has revealed several promising properties compared to conventional QD-IBSCs, including (i) enhanced TSPA and external quantum efficiency [114, 115], (ii) reduced losses via radiative recombination, leading to improved carrier extraction and overall efficiency [116], and (iii) recovery of V_{OC} under concentrated illumination [117–119]. However, the main critical unwanted transition in type-II QR IBSCs is hole capture into the QR. We will show Section 5.3.3 that this transition is not likely to be significant.

Despite numerous and ongoing experimental investigations of type-II $GaAs_{1-x}Sb_x/GaAs$ QRs for IBSC applications, there is little detailed information available in the literature regarding the electronic properties of these structures. In the rest of this chapter, we present a combined

analytical and numerical analysis of the electronic properties of $GaAs_{1-x}Sb_x$/GaAs QRs and demonstrate that minor changes in morphology, compatible with established epitaxial growth, can be exploited to tune the QR hole ground state (IB) to an optimum energy to maximise IBSC efficiency.

5.2 Eigenstates of an infinite quantum ring

Our analytical analysis is based on the solution of the time-independent Schrödinger equation for the eigenstates of an idealised (001)-oriented cylindrical QR of infinite potential depth. The QR is taken to have inner and outer radii a_1 and a_2 in the plane perpendicular to the (001)-direction, and height h along the (001)-direction. A schematic illustration of the QR geometry is shown in Fig. 5.2(a). Choosing the origin of a cylindrical polar coordinate system (r, ϕ, z) to lie at the centre of the base of the QR, the potential – which is axially symmetric about the (001), or z, direction and hence independent of ϕ – is

$$V(r,h) = \begin{cases} 0\,, & a_1 < r < a_2 \text{ and } 0 < z < h \\ \infty, & \text{otherwise} \end{cases} . \tag{5.1}$$

Separating the variables by writing the QR eigenstates $\psi_{lmn}(r,\phi,z) = R_{lm}(r)\Phi_m(\phi)Z_n(z)$, yields three separable differential equations (one in each of the radial, polar and longitudinal coordinates r, ϕ and z). The solution of the ϕ and z equations are as in the conventional cylindrical QD of infinite potential depth (corresponding here to $a_1 = 0$). The solution in the polar (ϕ) direction is trivial due to the axial symmetry of the potential about the z direction, with $\Phi_m(\phi) = \frac{1}{\sqrt{2\pi}} e^{im\phi}$ for integer m. Along the z direction the eigenstates are those of the infinite square well

$$Z_n(z) = \sqrt{\frac{2}{h}} \sin\left(\frac{n\pi z}{h}\right) . \tag{5.2}$$

Within the QR $V(r,z) = 0$, and the radial equation reduces to the (cylindrical) Bessel equation, the general solution of which is $R_{lm}(r) = A_{lm}J_m(kr) + B_{lm}Y_m(kr)$, where $J_m(kr)$ and $Y_m(kr)$ are respectively the Bessel functions of the first and second kind. Here, l is a positive integer which indexes the allowed values k_{lm} of the radial wave vector k. To this point, the general solution is identical to that of a cylindrical QD of infinite potential depth. The difference in the QR case arises due to the presence of the central barrier for $r \leq a_1$. Due to the presence of the central barrier we seek radial wave functions satisfying the boundary conditions $R_{lm}(a_1) = 0$ and $R_{lm}(a_2) = 0$. Applying the first of these conditions allows us to solve for B_{lm} in terms of A_{lm}, giving

$$R_{lm}(r) = A_{lm}\left(J_m(kr) - \frac{J_m(ka_1)}{Y_m(ka_1)}\,Y_m(kr)\right), \tag{5.3}$$

where the constant A_{lm} can be determined via normalisation. Applying the second boundary condition then yields the transcendental equation

$$J_m(ka_1)\,Y_m(\rho ka_1) - J_m(\rho ka_1)\,Y_m(ka_1) = 0\,, \tag{5.4}$$

where we have defined $\rho = \frac{a_2}{a_1}$ as the ratio of the outer and inner QR radii (so that $\rho ka_1 = ka_2$). The wave vector k_{lm} associated with the radial wave function $R_{lm}(r)$ is then, for a given value of m, determined via the l^{th} root $k_{lm}a_1$ of Eq. (5.4). Defining $a = a_2 - a_1$ as the radial thickness of the QR, we note that Eq. (5.3) reduces to $R_{lm}(r) = A_{lm}J_m(kr)$ in the limit $a_1 \to 0$ ($a_2 \to a$), with Eq. (5.4) correspondingly reducing to $J_m(ka) = 0$, yielding the well-known solution of Schrödinger's equation for a cylindrical QD of radius a as the QR is transformed into a QD via the removal of the central potential barrier.

The energies of the QR eigenstates are given by the sum of the in- and out-of-plane contributions

$$E_{lmn} = \frac{\hbar^2}{2m_0}\left(\frac{k_{lm}^2}{m_\perp^*} + \frac{\pi^2 n^2}{m_\parallel^* h^2}\right), \tag{5.5}$$

where m_0 is the free electron mass, and where $m_\parallel^*$ and $m_\perp^*$ are respectively the (relative) effective mass parallel and perpendicular to the [001] growth direction. The QR ground state is obtained for quantum numbers $(l, m, n) = (1, 0, 1)$.

A useful convergence property of the ground state radial wave vector k_{10} can be obtained from the first root of Eq. (5.4) for $m = 0$. Specifically, for a QR having radial thickness $a = a_2 - a_1$, k_{10} converges rapidly to $\frac{\pi}{a}$ with increasing inner radius a_1. This provides a useful approximation, $k_{10} \approx \frac{\pi}{a}$, which can be used to estimate the radial contribution to the QR ground state energy (cf. Eq. (5.5)).

To see that this is the case we note that, for large x, $J_0(x) \approx \sqrt{\frac{2}{\pi x}}\cos\left(x - \frac{\pi}{4}\right)$ and $Y_0(x) \approx \sqrt{\frac{2}{\pi x}}\sin\left(x - \frac{\pi}{4}\right)$, so that the $m = 0$ radial wave function can be written in the form

$$R_{l0}(r) \approx C_{l0}\sqrt{\frac{2}{\pi kr}}\cos\left(kr + \theta\right), \tag{5.6}$$

for some phase θ and normalisation constant C_{l0}. This approximate expression for $R_{l0}(r)$ satisfies the boundary conditions $R_{l0}(a_1) = 0$ and $R_{l0}(a_2) = 0$ for radial wave vectors $k_{l0} \sim \frac{l\pi}{a}$.

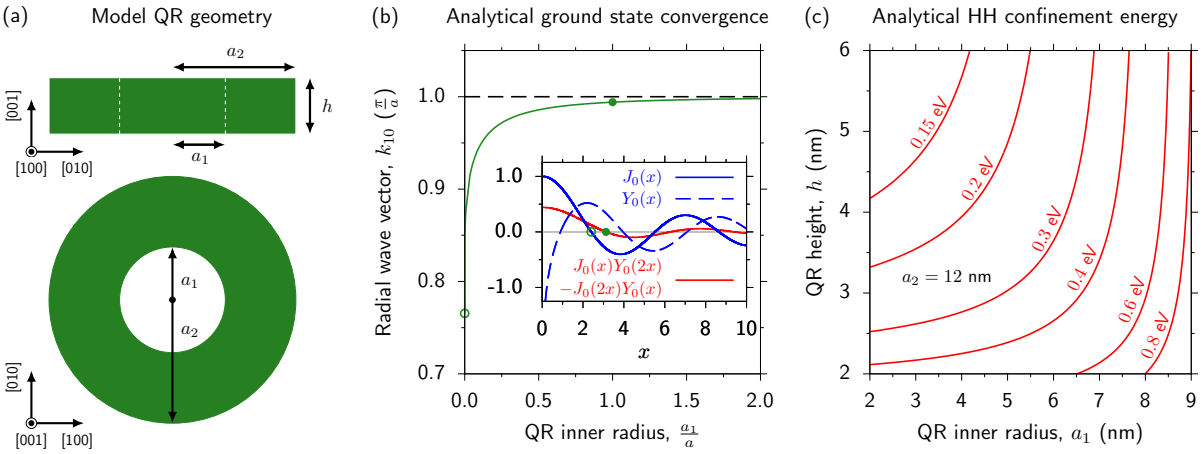


FIGURE 5.2: (a) Schematic illustration of the QR geometry considered in this work, viewed side-on from the (100)-direction (top) and top-down from the (001)-direction (bottom). The cylindrical QR has inner and outer radii a_1 and a_2, radial thickness $a = a_2 - a_1$, and height h along the growth direction. (b) Variation of the ground state radial wave vector k_{10}, computed as the first root of Eq. (5.4) for $m = 0$, as a function of the inner radius a_1 for a QR of fixed radial thickness a. As a_1 increases as a proportion of a, k_{10} rapidly converges to a value of $\frac{\pi}{a}$ (dashed black line). The inset shows the Bessel functions $J_0(x)$ (solid blue line) and $Y_0(x)$ (dashed blue line), as well as the left-hand side of Eq. (5.4) for $\rho = 2$ (i.e. $a_1 = a$). (c) Contour map showing the confinement energy associated with the HH ground state in a GaSb/GaAs QR – assuming an infinite confining quantum well offset – having outer radius $a_2 = 12$ nm, calculated via Eqs. (5.4) and Eq. (5.5), as a function of the QR inner radius a_1 and height h.

We therefore deduce that, for a QR of fixed radial thickness a, as the inner radius a_1 increases, the first root k_{10} of Eq. (5.4) should converge to $\frac{\pi}{a}$.

To verify that this is the case we have computed the first root $k_{10}a_1$ of Eq. (5.4) as a function of a_1 for a QR having fixed thickness a (= 11.5 nm). The results of this analysis are summarised in Fig. 5.2(b), where the solid green line shows the calculated variation of k_{10} (in units of $\frac{\pi}{a}$) as a function of $\frac{a_1}{a}$ ($= \frac{1}{\rho-1}$). The inset to Fig. 5.2(b) shows the functions $J_0(x)$ (solid blue line) and $Y_0(x)$ (dashed blue line), as well as the left-hand side of Eq. (5.4) for $m = 0$ and $\rho = 2$ ($a_2 = 2a_1$, solid red line). Examining Fig. 5.2(b), we note *rapid* convergence of k_{10} to $\frac{\pi}{a}$ with increasing $\frac{a_1}{a}$. For $a_1 = 0$ – i.e. for a cylindrical QD of radius a – k_{10} is given by the first root of $J_0(ka) = 0$. This solution, highlighted by the open green circles in Fig. 5.2(b) and its inset, is $k_{10}a \approx 2.4048$ (the first zero of $J_0(ka)$), so that $k_{10} \approx 0.7655 \times \frac{\pi}{a}$. As $\frac{a_1}{a}$ increases due to the inclusion of the central potential barrier to form a QR, k_{10} then rapidly approaches $\frac{\pi}{a}$. For example, for $\frac{a_1}{a} = 1$ ($\rho = 2$), which corresponds well to real QR dimensions, we compute $k_{10} \approx 0.9941 \times \frac{\pi}{a}$.

Generally, we find $k_{10} = \frac{\pi}{a}$ to be an excellent approximation to the ground state radial wave vector for $\frac{a_1}{a} \gtrsim 1$ – i.e. for $a_1 \gtrsim \frac{a_2}{2}$ or, equivalently, $\rho \lesssim 2$. For $a = 11.5$ nm we note that $\rho = 2$ corresponds to an outer QR radius $a_2 = 2a_1 = 23$ nm, dimensions typical of epitaxially grown $GaAs_{1-x}Sb_x/GaAs$ QRs, which will be analysed in further detail in Sec. 5.3. This rapid convergence of k_{10} then provides a simple and reliable approach to estimate the radial

contribution to the QR ground state energy, circumventing the requirement to numerically compute the roots of Eq. (5.4), with the overall accuracy of the corresponding estimate of the ground state energy E_{101} being better for smaller overall confinement energy (cf. top left of Fig. 5.2(c)).

We have used Eq. (5.5) to estimate the confinement energy associated with the HH ground state in a GaSb/GaAs QR. To do so we set $m_{\parallel}^{*} = (\gamma_1 - 2\gamma_2)^{-1}$ and $m_{\perp}^{*} = (\gamma_1 + 2\gamma_2)^{-1}$, which are the bulk HH VB edge effective masses admitted by the 6-band Luttinger-Kohn Hamiltonian, where γ_1 and γ_2 are the VB Luttinger parameters. Following Ref. [69] we set $\gamma_1 = 13.4$ and $\gamma_2 = 4.7$ and respectively obtain $m_{\parallel}^{*} = 0.250$ and $m_{\perp}^{*} = 0.044$ for the (relative) HH effective masses parallel and perpendicular to the [001] direction. The results of our calculations are summarised in Fig. 5.2(c), in which the solid red lines are contours of constant HH ground state (confinement) energy as a function of inner radius a_1 and height h, for a QR having fixed outer radius $a_2 = 12$ nm. We note from these results the flexibility offered by the QR geometry from the perspective of band structure engineering for IBSC applications: the HH confinement energy can readily be tuned across a broad range via relatively minor adjustments in QR morphology, allowing the IB energy to be engineered in a hole-based QR-IBSC. This provides distinct advantages compared to, e.g., equivalent $GaAs_{1-x}Sb_x/GaAs$ QDs, since the QR inner radius a_1 provides an additional parameter by which the electronic properties can be tuned. The realities of epitaxial growth do not in general allow a_1 to be fine tuned independently of the other QR dimensions a_2 and h, the relationships between which are in practice determined in large part by the (Stranski-Krastanov) strain relaxation mechanism that drives QR formation. However, it is generally observed that Stranski-Krastanov QR formation tends to fix a_2, with the inner radius a_1 then depending largely on growth rate. Correspondingly, QR heights are generally found to be in the range $h = 3 \pm 2$ nm [120]. Despite incomplete control over the morphology of individual QRs during epitaxial growth, we emphasise that $GaAs_{1-x}Sb_x/GaAs$ QRs offer additional benefits for IBSC applications due to the nature of carrier localisation within these structures. To elucidate these properties requires a more detailed, quantitative analysis of the electronic properties, to which we now turn our attention.

5.3 Numerical results: strain, band offsets, and carrier localisation

While the analytical treatment of Sec. 5.2 provides useful insight into some of the general features of the electronic properties of QRs, this approach neglects several key factors which play an important role in determining the nature of the electronic properties in a real semiconductor QR. Firstly, the large lattice mismatch which drives QR formation – 7.2% in the case of GaSb/GaAs – produces large, strongly position dependent strain fields, which impact the

electronic properties directly (as well as via the associated strain-induced piezoelectric potential). Secondly, the natural type-II band offsets between GaSb and GaAs produce confining potentials which are markedly different in nature for electrons and holes. Thirdly, the analytical treatment described above neglects band hybridisation effects, which can be expected to play a role in determining the precise nature of QR eigenstates in the presence of strain, quantum-confinement, spin-orbit coupling and narrow band gap, all of which are present in real $GaAs_{1-x}Sb_x/GaAs$ QRs. In order to quantitatively understand the QR electronic structure we have therefore undertaken multi-band $\mathbf{k}\cdot\mathbf{p}$ calculations, based on the formalism described in Sec. 2.4.2.

Our numerical analysis of the electronic properties of $GaAs_{1-x}Sb_x/GaAs$ QRs is based on multi-band $\mathbf{k}\cdot\mathbf{p}$ calculations [121]. We employ a supercell approach, by embedding a cylindrical $GaAs_{1-x}Sb_x/GaAs$ QR in a GaAs matrix, and relax the supercell by minimising the total elastic energy with respect to the components ϵ_{ij} of the strain tensor to obtain the strain fields $\epsilon_{ij}(\mathbf{r})$. The QR VB eigenstates are computed using a strain-dependent 6-band $\mathbf{k}\cdot\mathbf{p}$ Hamiltonian – i.e. the Luttinger-Kohn VB Hamiltonian, including Bir-Pikus strain-related terms – which explicitly treats heavy-hole (HH), light-hole (LH) and spin-split-off (SO) VB states. The QR CB eigenstates are computed using a strain-dependent 1-band (effective mass) Hamiltonian. We note that the separate treatment of the CB and VB eigenstates has been chosen to circumvent the emergence of spurious solutions in full 8-band $\mathbf{k}\cdot\mathbf{p}$ calculations, which arise in the presence of large plane wave cut-off energies due to the strong inter-band coupling present in narrow-gap GaSb. Both the 6-band VB and 1-band CB calculations explicitly include the strain-induced piezoelectric potential, computed to second order for a given structure using the relaxed strain fields. The QR band offsets are computed firstly for an unstrained structure using the model solid theory – assuming a natural (unstrained) VB offset of 0.58 eV between GaSb and GaAs [89, 92] – with the position-dependent band edge energy profiles then computed via direct diagonalisation of the strain-dependent bulk 6- and 1-band $\mathbf{k}\cdot\mathbf{p}$ Hamiltonians at each real space grid point in the supercell.

Our numerical calculations have been implemented using a plane wave (reciprocal space) approach, using the S/Phi/nX software library [32]. We employ (001)-oriented supercells of size 50 nm $\times$ 50 nm $\times$ 14 nm, and a plane wave cut-off energy equivalent to a real space resolution of 0.2 nm in each of the x, y and z directions. This choice of plane wave cut-off was validated by examining the convergence of the bound carrier eigenstate energies, which were found to vary by < 1 meV with respect to further increases in the size of the plane wave basis set. All material parameters used in our calculations – including lattice and elastic constants, band gaps, VB spin-orbit splitting energies and Luttinger parameters, electron effective masses, and CB and VB edge deformation potentials – are taken from Ref. [69], with the exception of the first and second order piezoelectric coefficients, which are taken from Ref. [33]. All calculations are performed at temperature $T = 300$ K.

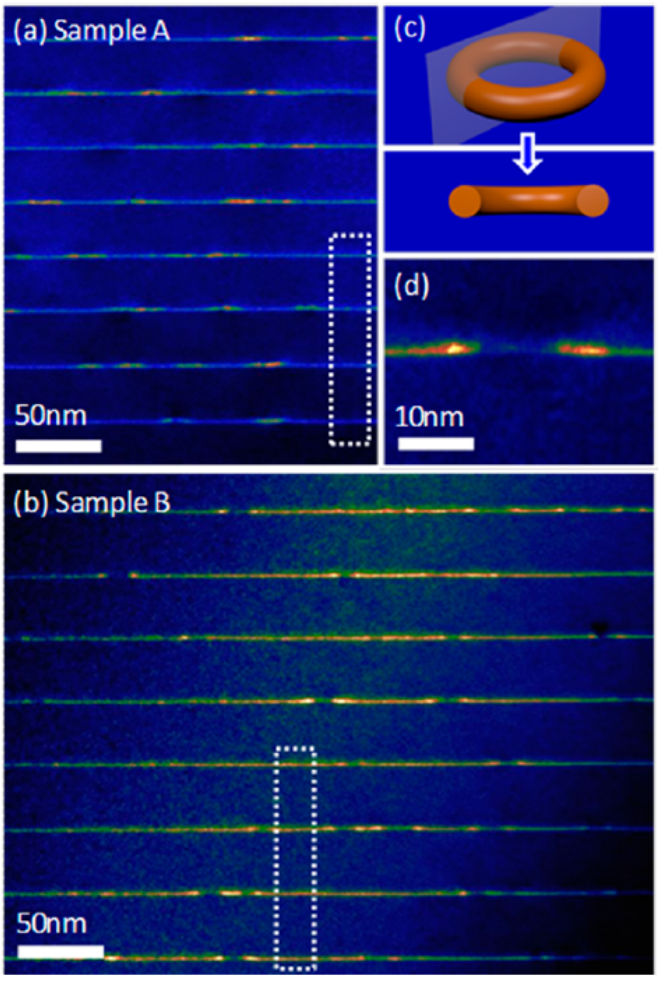


FIGURE 5.3: (a) and (b) TEM images showing GaSb QR arrays embedded in a GaAs host matrix. The prototype structures are grown at University of Lancaster. (c) A schematic of the QR structure indicating a cross section through the centre of the ring that is shown in TEM images. (d) A closer look at the TEM image of a cross section of a GaSb QR array in GaAs host matrix.

We provide here an overview of the results of these calculations, elucidating the electronic properties of $GaAs_{1-x}Sb_x/GaAs$ QRs and identifying optimised QR morphologies providing electronic properties well-suited to IBSC applications. We investigate the strain profile and the strain-induced piezoelectric potential in type-II GaSb/GaAs QR structures in Secs. 5.3.1 and 5.3.2, respectively. Then in Sec. 5.3.3, we investigate the localisation of carrier states in a type-II GaSb/GaAs QR structure.

5.3.1 Strained quantum ring

Here, we calculate and analyse the strain profile and band lineups in existing GaSb/GaAs QR prototype structures grown at University of Lancaster [119]. Fig. 5.3 shows a transmission electron microscopy (TEM) image of two of these structures provided by University of Lancaster. We note that the QR arrays shown in Fig. 5.3(a) and (b) are the cross sections of these

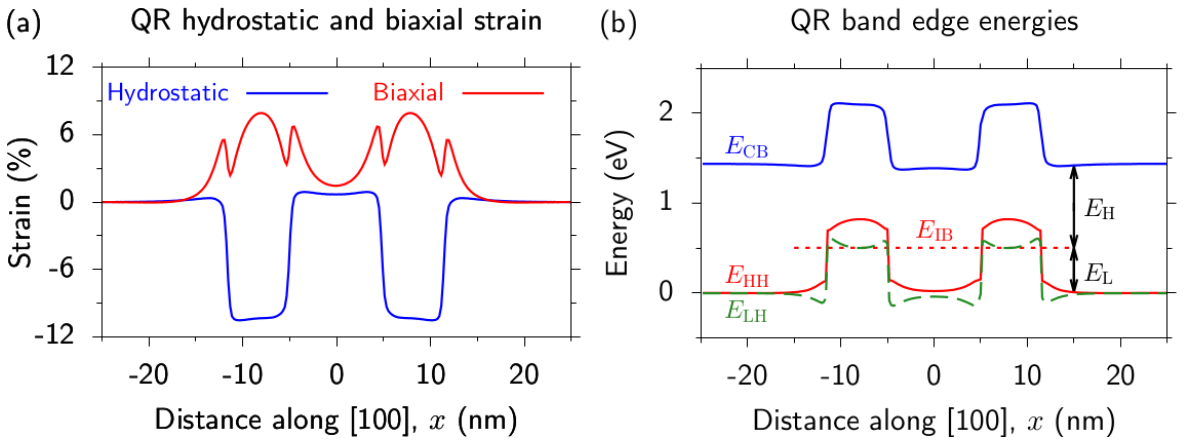


FIGURE 5.4: (a) Linescan along the (100) in-plane direction, through the centre of the QR, showing the calculated hydrostatic (solid blue line) and biaxial (solid red line) components of the strain field for a GaSb/GaAs QR having $a_1 = 5$ nm, $a_2 = 11.5$ nm and $h = 3$ nm. (b) Linescan along the (100) in-plane direction, through the centre of the QR, showing the calculated bulk band edge energies (band offsets) for the CB (solid blue line), and light-hole (LH; dashed green line) and heavy-hole (HH; solid red line) VBs, for the same QR as in (a). The dashed red line shows the energy of the highest energy bound hole state $h1$ – i.e. the intermediate band – at energy E_{IB}, separated from the CB and VB edges by the sub-band gaps E_{H} and E_{L} respectively.

structures in xy plane, and hence may not necessarily show a cross section of the centre of the ring. Nevertheless, Fig. 5.3(d) shows a good example of a cross section through the centre of these rings. For our $\mathbf{k}\cdot\mathbf{p}$ calculations we begin by considering an exemplar GaSb/GaAs QR having inner radius $a_1 = 5$ nm, outer radius $a_2 = 11.5$ nm and height $h = 3$ nm (dimensions typical of epitaxially grown QRs). The solid blue and red lines in Fig. 5.4(a) respectively show linescans – taken through the centre of the QR along the (100)-direction – of the calculated hydrostatic and biaxial components $\epsilon_{\mathrm{hyd}} = \mathrm{Tr}(\epsilon)$ and $\epsilon_{\mathrm{bia}} = \epsilon_{zz} - \frac{1}{2}(\epsilon_{xx} + \epsilon_{yy})$ of the strain fields in the structure. The hydrostatic strain reaches values as low as -10.5% within the GaSb regions, reflecting that the QR is under significant compressive strain when grown epitaxially on GaAs. We note that the impact of the strain relaxation in the structure acts to place the central GaAs region of the QR under a minor amount ($\lesssim 1\%$) of tensile strain, due to its being surrounded in the plane perpendicular to the (001)-direction by GaSb material having a larger lattice constant. The calculated biaxial strain resembles that associated with a cylindrical QD [122], varying strongly at the interfaces with the surrounding barrier material, albeit with additional features due to the presence of the central GaAs barrier.

Figure 5.4(b) shows a linescan of the band edge energies for the same GaSb/GaAs QR, calculated using the strain fields shown (in part) in Fig. 5.4(a). The band edge energy (confining potential) profiles are shown – using solid blue, solid red and dashed green lines for the CB, HH VB and LH VB edges, respectively – as a linescan along the (100)-direction, through the centre of the QR. We firstly note the presence of large type-II band offsets in the QR. There

exist strong confining potentials for holes within the GaSb region, reaching a maximum depth of ≈ 820 meV for HH states, while electrons are excluded from the GaSb region by a potential barrier having a maximum height of ≈ 670 meV. Due to the compressive strain in the GaSb region, the HH VB edge is pushed higher in energy than the LH VB edge, resulting in a larger confining potential for HH states and ensuring that the highest energy hole bound state – i.e. the IB in a hole-based $GaAs_{1-x}Sb_x$/GaAs QR-IBSC – is primarily HH-like. We therefore expect that hole states will be strongly confined within the GaSb region, experiencing strong annular localisation in the plane perpendicular to the (001)-direction, as well as strong localisation along the (001)-direction. We also note that the aforementioned minor tensile strain in the central barrier of the QR tends to reduce slightly the CB edge energy in the centre of the QR. This, combined with the presence of a confining potential for electrons in the plane perpendicular to the (001)-direction, suggests the possibility of quasi-localised electron states residing in the central barrier region.

5.3.2 The strain-induced piezoelectric potential

Here we calculate the strain-induced piezoelectric potential in a model GaSb/GaAs QR in the presence of (i) first order only, (ii) second order only, and (iii) first and second order piezoelectric potential. Fig. 5.5 shows the strength and distribution of the piezoelectric potential resulting from the two orders of the piezoelectric tensor as outlined in Section 2.3.2. Apart from the different orientations and signs of the two contributions, an important distinctiveness of the second-order piezoelectric potential is its restriction to the interior of the QR, which is in noticeable contrast to the widespread first-order potential. This difference is essentially related to the origin of the total polarisation $P = P_1 + P_2$, where P_1 is a function of the shear-strain components alone, and P_2 results mainly from the product of the diagonal and the shear strain. However, in contrast to the shear-strain components, the diagonal elements ϵ_{ii} are large only inside the QR and its close vicinity. Therefore, P_2 charges are created primarily in this region. We note that the total strain-induced piezoelectric potential associated with a type-II GaSb/GaAs structure attains a maximum value of ≈ 17 meV throughout the calculational supercell, and has minimal impact on the electronic properties . We note that the piezoelectric potential is more pronounced if the structure is grown along the (111)-direction. This is primarily because the calculated strain values [1] are significantly higher in (111)-grown structures [21]. In this case, the piezoelectric potential also points along the (111)-direction, leading to a potential drop across the heterostructure, giving what can be regarded as a quantum confined Stark effect, which tends to shift the electron and hole states towards opposite sides of the structure along the growth direction.

[1] More information on the effect of strain values on determining the piezoelectric potential can be found in Sec. 2.3.2.

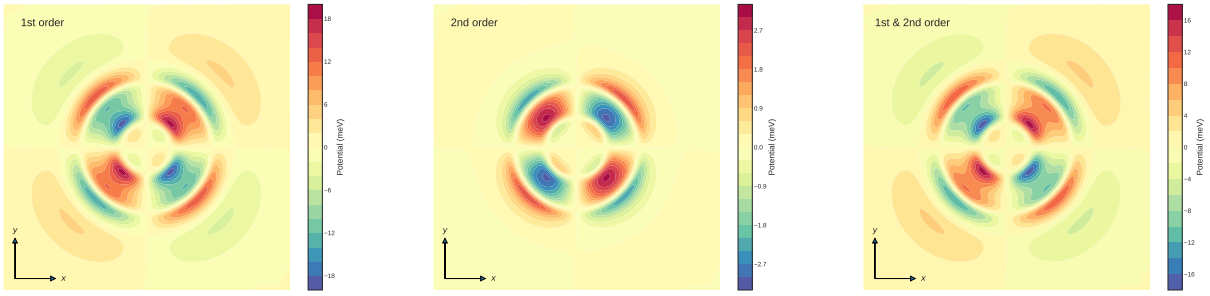


FIGURE 5.5: Contour plots of piezoeletric potential 4 nm above the middle of the ring in the xy plane, where x and y are along the (100) and (010) directions respectively.

5.3.3 Carrier localisation

Figures 5.6(a) and 5.6(b) respectively show cross-sections through the centre of the QR of the calculated electron (green) and hole (orange) probability densities in the plane perpendicular to the (010) and (001) directions. Fig. 5.7 also shows a line scan of the quasi-bound electron and hole probability denisties in the central yz plane. We observe very strong localisation of the highest energy hole bound state within the QR, with minimal tunneling of the hole probability density outside of the GaSb region. We also note the presence of a resonant electron state within the central GaAs barrier of the QR, which our calculations identify as a consequence of the type-II band offsets (cf. Fig. 5.4(b)). While this electron state is strongly localised in the plane of the QR, it is less strongly localised along the (001)-direction, due to the absence of a strongly confining CB potential along that direction.

We note that the quasi-localised electron state for which the probability density is shown in Figures 5.6(a) and 5.6(b) was not the lowest energy electron state identified in our calculation: it was in fact the sixth lowest energy electron state. The type-II band alignment in this GaSb/GaAs QR results in a large range of delocalised electron states lying at and above the GaAs CB edge in energy, which are characterised by their probability density being excluded from the central region of the QR in the plane of the QR. (The precise number of delocalised states appearing in a given energy range in a numerical calculation depends on a combination of the supercell dimensions and the size of the plane wave basis set employed.) The quasi-bound electron state identified in our analysis lies only 31 meV above the GaAs CB edge in energy and, given its higher spatial overlap with the highest energy bound hole state compared to the delocalised CB edge states described above, transitions involving this state can be expected to contribute significantly to the band edge optical absorption. From the perspective of IBSC design and optimisation, the presence of this unusual quasi-bound electron state is particularly appealing. By varying the QR morphology the in-plane confinement of this electron state can be engineered so as to control the spatial overlap with the highest energy bound hole state. This overlap governs a key trade-off in an IBSC, between (i) the generation rate associated with

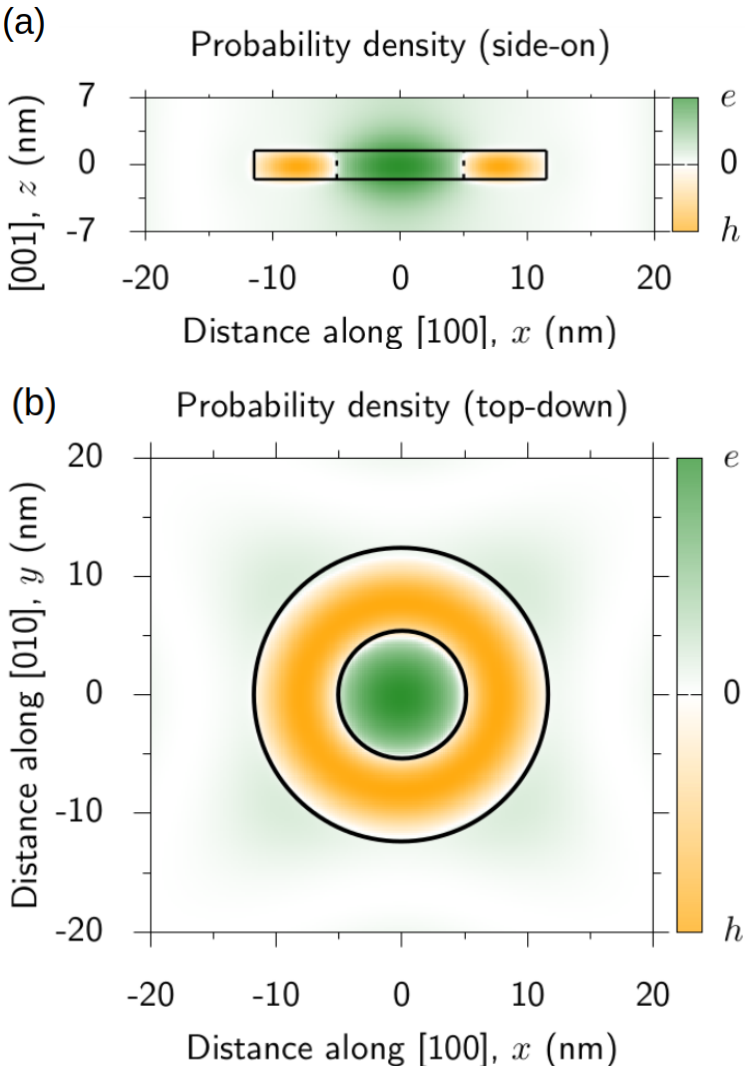


FIGURE 5.6: (a) Side-on view, along the (010)-direction, of the probability density associated with the lowest energy quasi-bound electron (green) and highest energy bound hole (orange) states. (b) Top-down view, along the (001)-direction, of the probability density associated with the same two states as in (a).

carriers occupying IB states (i.e. the generation of holes in the VB via absorption of photons having energy $\geq E_{\mathrm{L}}$), and (ii) the radiative lifetime for recombination involving electron and hole states (i.e. recombination of quasi-bound CB electrons with bound IB holes via emission of photons having energy $> E_{\mathrm{H}}$). Moreover, the weak electron localisation along the (001)-direction suggests that photo-generated electrons can be readily collected from the QRs in a real QR-IBSC structure, with hole extraction proceeding via excitation of holes from the IB to the GaAs VB via TSPA. Finally, the large VB offsets in these QR structures result in very large ionisation energies of ≈ 0.5 eV for IB hole states. This ionisation energy is far in excess of the thermal energy in the range of temperatures relevant to IBSC operation, and so electrical leakage of carriers via thermionic emission from the IB should be adequately suppressed in these heterostructures.

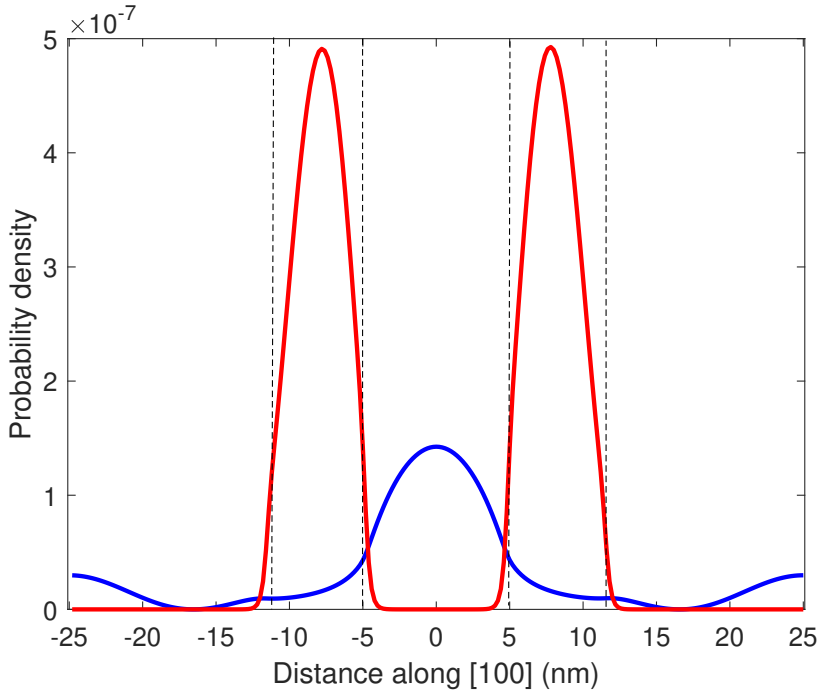


FIGURE 5.7: A line scan of the probability density associated with the lowest energy quasi-bound electron (red curve) and highest energy bound hole (blue curve) in the central yz plane. The vertical black dashed lines represent the QR region.

5.4 Intermediate band gap engineering in type-II quantum rings

For the GaSb/GaAs QR considered above we calculate that the highest energy bound hole state – the energy of which is denoted by a horizontal dotted red line in Fig. 5.4(b) – lies 502 meV above the GaAs barrier VB edge, corresponding to IBSC sub-band gaps $E_{\rm L} = 0.502$ eV and $E_{\rm H} = E_{\rm G}({\rm GaAs}) - E_{\rm L} = 0.922$ eV at temperature $T = 300$ K. We note that these sub-band gaps are – in addition to being in good quantitative agreement with experimental measurements [123] – close to the optimum values associated with an IBSC implemented using a GaAs host matrix. Specifically, for GaAs (which has $E_{\rm G} = 1.42$ eV at $T = 300$ K) the optimum sub-band gaps $E_{\rm L} = 0.45$ eV and $E_{\rm H} = 0.97$ eV correspond to a detailed balance efficiency limit of $\approx 58\%$ under concentrated illumination, close to the overall efficiency limit for an ideal IBSC – cf. assumptions outlined in Sec. 5.1. However, for a given host matrix band gap $E_{\rm G}$ the detailed balance efficiency is a sensitive function of the sub-band gaps $E_{\rm L}$ and $E_{\rm H}$, reducing rapidly as the sub-band gaps are detuned from their optimum values. It is therefore desirable to engineer the band structure such that the sub-band gaps are as close as possible to their optimum energies. The calculated value of $E_{\rm L}$ ($E_{\rm H}$) for the exemplar GaSb/GaAs QR considered above is only ≈ 50 meV higher (lower) than the optimum value, suggesting that minor changes in morphology will be sufficient to realise optimum sub-band gaps.

In order to identify optimised QR morphologies we therefore proceed by repeating our analysis as a function of (i) QR height h, and (ii) QR Sb composition x, for QRs having the same inner

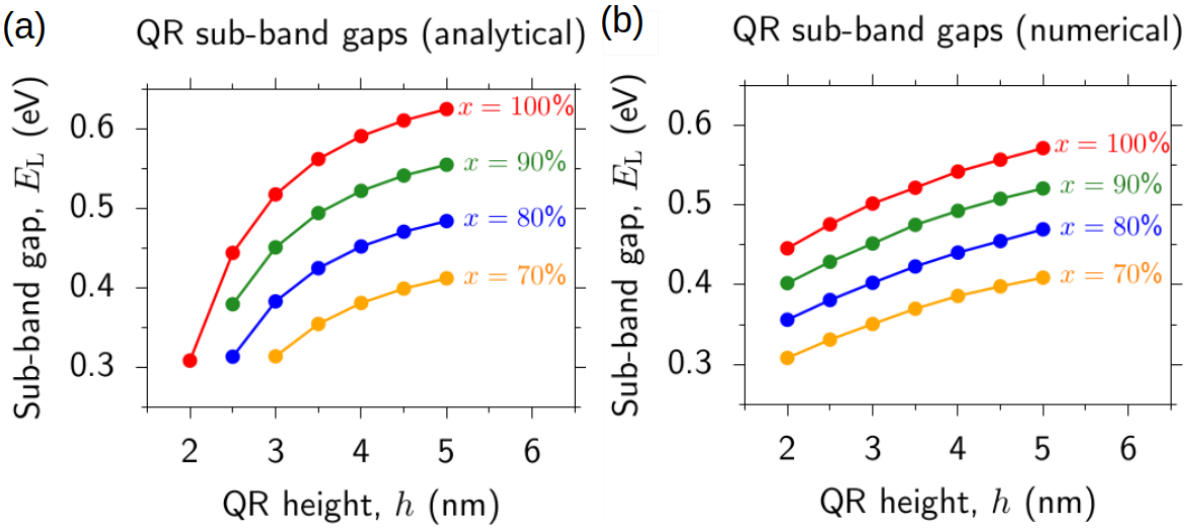


FIGURE 5.8: (a) Lower energy sub-band gap E_L as a function of QR height h for $GaAs_{1-x}Sb_x/GaAs$ QRs having inner and outer radii $a_1 = 5$ nm and $a_2 = 11.5$ nm, estimated based on Eqs. (5.4) and (5.5). (b) As in (a), but with the values of E_L obtained from full numerical multi-band $\mathbf{k}\cdot\mathbf{p}$ calculations.

and outer radii $a_1 = 5$ nm and $a_2 = 11.5$ nm considered above. We note that we have chosen to vary the QR height rather than in-plane dimensions since (i) real $GaAs_{1-x}Sb_x/GaAs$ QRs typically have low aspect ratios $\frac{h}{2a_2} \approx 0.1$, (ii) the confinement energies in such low aspect ratio structures, and hence the sub-band gaps, are dominated by confinement along the (001)-direction (cf. Eq. (5.5)), and (iii) characterisation of epitaxially grown $GaAs_{1-x}Sb_x/GaAs$ QRs has revealed significantly larger *relative* variations in h than in a_1 or a_2. The results of these calculations are summarised in Figs. 5.8(a) and 5.8(b), which respectively show the sub-band gap energy E_L calculated based on the analytical and numerical models. Results are shown for $GaAs_{1-x}Sb_x/GaAs$ QRs having Sb compositions $x = 100$, 90, 80 and 70% using red, green, blue and orange closed circles, respectively.

We note that since the analytical model assumes a confining potential of infinite depth, it is not capable of directly predicting E_L (which is obtained from the full numerical calculations as the difference $E_{h1} - E_{VB}$ in energy between the highest energy bound hole state and host matrix VB edge). In order to estimate E_L using the analytical model we have therefore (i) used Eqs. (5.4) and (5.5) to calculate the confinement energy ΔE_{h1} associated with the HH ground state in a QR of infinite potential depth, and (ii) used the (maximum) HH band offset ΔE_{HH} extracted from a full numerical calculation to compute $E_L = \Delta E_{HH} - \Delta E_{h1}$. Due to its assumption of an infinitely deep confining potential, the analytical approach naturally overestimates ΔE_{h1} – in particular the contribution associated with confinement along the (001)-direction – and hence underestimates E_L for short QRs having $h \lesssim 3$ nm. Nonetheless, we observe that the analytical model accurately captures the key trends observed in the results of the full numerical calculations, and provides reasonably good quantitative agreement with

the results of the numerical calculations for $h \gtrsim 3$ nm, across the full range of Sb compositions considered.

Examining Fig. 5.8(b), the results of our numerical calculations suggest that optimum IBSC sub-band gaps are obtained in short GaSb/GaAs QRs having $h \approx 2$ nm, which lies well within the range of heights observed in real structures. [120] By reducing the QR Sb composition x at fixed h to form alloyed $GaAs_{1-x}Sb_x$/GaAs QRs, we find that E_L decreases by $\approx 45 - 50$ meV for each 10% reduction in x. Therefore, in QRs having reduced Sb composition – due, e.g., to interfacial Sb-As intermixing [124, 125] – the QR height should be slightly increased in order to restore E_L to its optimum energy. In practice, this constitutes reducing the confinement energy ΔE_{h1} so as to maintain fixed hole ionisation energy in response to the reduction in ΔE_{HH} associated with a reduction in x. For Sb compositions $x \gtrsim 75\%$ our calculations indicate that an optimum sub-band gap $E_L = 0.45$ eV is maintained for an ≈ 1 nm increase in h in response to each 10% reduction in x. For Sb compositions $x \lesssim 75\%$ our calculations indicate that QR heights $h \gtrsim 5$ nm are required to obtain optimised electronic properties. Such heights are outside the range typically obtained via epitaxial growth, suggesting that only epitaxial growth of $GaAs_{1-x}Sb_x$/GaAs QRs having $x \gtrsim 75\%$ is likely to produce heterostructures possessing electronic properties which are well-suited to IBSC applications.

We note, however, that our analysis of the electronic properties here has focused solely on idealised QR structures, possessing exact cylindrical shape and uniform alloy composition throughout the $GaAs_{1-x}Sb_x$ region. The presence of Sb-As intermixing at the ring-barrier interface in real $GaAs_{1-x}Sb_x$/GaAs QRs[124, 125] results in a non-uniform alloy composition, which may modify the strain fields and confining potentials compared to those considered in our exploratory calculations here. Overall, we expect the resulting modifications of the electronic properties to be quantitative rather than qualitative in nature compared to those described above for ideal QRs. Of more importance from the perspective of designing real IBSC devices is to build upon our initial analysis here by undertaking theoretical investigations of the optical properties of, and radiative and non-radiative losses in, $GaAs_{1-x}Sb_x$/GaAs QRs and vertical QR stacks.

5.5 Summary and conclusions

In this chapter, we have presented a theoretical analysis of the electronic properties of type-II $GaAs_{1-x}Sb_x$/GaAs QRs based on a combined analytical and numerical approach, and identified optimised combinations of QR morphology and alloy composition for the realisation of hole-based IBSCs – in which the IB is formed by the highest energy bound hole state in the QR – offering the maximum theoretical efficiency available via inclusion of an IB in a GaAs matrix.

Analytically, we presented the solution of the time-independent Schrödinger equation for a cylindrical QR of infinite potential depth and derived a transcendental equation which must be satisfied by bound QR eigenstates. The relationship to the solution of the well-known problem of the cylindrical QD was described, and it was demonstrated that (i) the QR eigenstates evolve smoothly from those of the QD, and (ii) the convergence properties of the QR ground state allow the confinement energy to be estimated straightforwardly, and to high accuracy, for realistic QRs having dimensions typical of those achieved via epitaxial growth. Our analytical analysis demonstrated that type-II $GaAs_{1-x}Sb_x/GaAs$ QRs offer significant benefits from the perspective of band structure engineering for IBSC applications, allowing the IB energy in a hole-based IBSC to be tuned across a broad range via changes in QR morphology.

Numerically, we used multi-band $\mathbf{k}\cdot\mathbf{p}$ calculations – including full strain and piezoelectric effects – to analyse the electronic properties of $GaAs_{1-x}Sb_x/GaAs$ QRs, both as a function of QR dimensions and Sb composition. We further demonstrated that the nature of the carrier confinement in these heterostructures is ideally suited to IBSC applications. Strong hole localisation, with large ionisation energies in excess of 0.4 eV, can be expected to mitigate carrier leakage from the IB via thermionic emission. Additionally, the interplay between strain relaxation and type-II band alignment in these QRs was demonstrated to give rise to electron states which, in the plane of the QR, are strongly localised in the central barrier of the QR. The unusual nature of the carrier localisation in these heterostructures suggests the potential to engineer the trade-off between the electron-hole overlap (which mediates carrier generation via optical absorption) and the radiative lifetime for photo-generated electron-hole pairs (which mediates carrier loss via radiative recombination).

For inner and outer radii $a_1 = 5$ nm and $a_2 = 11.5$ nm, typical of epitaxially grown QRs, our calculations indicate that an optimum IB sub-band gap $E_{\mathrm{L}} = E_{\mathrm{IB}} - E_{\mathrm{VB}}$ ($E_{\mathrm{H}} = E_{\mathrm{CB}} - E_{\mathrm{IB}}$) of 0.45 eV (0.97 eV) can be obtained in GaSb/GaAs QRs having height $h \approx 2$ nm. For $GaAs_{1-x}Sb_x/GaAs$ QRs having reduced Sb compositions x, our calculations indicate that decreases in x can be compensated by slight increases in h – by ≈ 1 nm for each 10% reduction in x – in order to maintain optimum sub-band gap energies. QRs grown to these specifications have a detailed balance efficiency limit of $\approx 58\%$ under concentrated illumination, close to the overall limit of 63.8% for ideal IBSCs. Given the sensitivity of the theoretical IBSC efficiency to the IB energy, our analysis suggests that careful control of QR morphology provides a viable route to realising optimised heterostructures suitable for IBSC applications.

Our initial calculations here, however, were guided by detailed balance efficiency limits which include a number of assumptions – e.g. optimium absorption spectra, infinite carrier mobilities, absence of non-radiative carrier losses, etc. – which are not reflective of the conditions in real quantum-confined heterostructure. Further theoretical work is therefore required to quantify,

and identify pathways towards simultaneously optimising the optical properties and mitigating losses (both radiative and non-radiative) in real $GaAs_{1-x}Sb_x$/GaAs QRs and vertical QR stacks, in order to identify rigorously optimised quantum-confined heterostructures for IBSC applications and to quantify photovoltaic efficiencies that can be realistically achieved using this novel platform.

Overall, our calculations highlight the suitability of type-II $GaAs_{1-x}Sb_x$/GaAs QRs for applications in hole-based IBSCs, and provide initial information regarding optimised combinations of QR alloy composition and morphology to guide the growth and fabrication of prototype QR-IBSC devices.

Chapter 6

Electronic properties of hydrogenated InGaAsN/GaAs dilute nitride nanostructures for single photon emission

In this chapter we perform an analysis of the electronic properties of hydrogenated InGaAsN QD-based heterostructures for application as single photon emitters operating at $\lambda \approx 1.31$ μm.

We begin in Section 6.1 by highlighting the applications and importance of single photon emitters operating at telecommunication frequencies. We take a look at the literature to review the related past works in this field.

In Sections 6.2 and 6.3 we give an overview of the structural properties of the existing InGaAsN:H nanostructures that were prepared at Sapienza University of Rome and whose characteristics are investigated later in the chapter. We then investigate the electronic properties of these structures in Sec. 6.4 . We turn our attention to the photoluminescence (PL) measurements performed on a series of InGaAsN:H QD-based nanostructures. Having understood the behaviour of the electronic structure of InGaAsN-based QDs under strain, we analyse the accuracy of our method by comparing the ground state transition energy with the measured PL energies.

Having benchmarked our theoretical model, in Sec. 6.5 we evaluate the feasibility of designing structures emitting at $\lambda \approx 1.31$ μm using the same material platform as discussed in Sec. 6.4.

6.1 Introduction and motivation

Dilute nitride semiconductors are an example of the failure of linear models for the physical properties of solids. Incorporating a few percent of N to GaAs causes changes in the physical properties that are opposite to those expected, assuming a linear interpolation of the GaAs and GaN properties. In these material systems, the replacement of a tiny fraction of arsenic atoms by nitrogen atoms leads to highly nonlinear effects in the electronic properties of the host lattice [12, 84]. Previous experiments have shown that post-growth irradiation of $GaAs_{1-x}N_x$ with atomic hydrogen leads to a complete reversal of the drastic bandgap reduction, as well as of other material parameters, caused by nitrogen incorporation [126].

Hydrogen is an impurity common to most phases of growth and processing of semiconductor materials and to the related mass production of electronic and optoelectronic devices [127]. High chemical reactivity and diffusivity of this element makes it important to consider H-induced effects in semiconductors. H tends to bind to dangling bonds associated with point and extended defects and therefore cleans up the band gap from the energy levels associated with those defects [128]. This process, usually referred to as *defect passivation*, leads to a large modification of conductivity in many semiconductors and often removes the detrimental consequences associated with crystal imperfections [129].

One of the most significant effects of hydrogen incorporation into a semiconductor has been observed in dilute nitride semiconductors. Despite the small amount of substituted atoms, N alloying perturbs dramatically the electronic properties of a host crystal such as GaAs, leading to a large decease of the band gap energy, a nonmonotonic variation of the electron effective mass and gyromagnetic factor, and a softened response to external perturbations such as hydrostatic pressure and temperature [127, 130].

Single-photon sources are light sources that emit light as single particles or photons. They are distinct from coherent light sources (lasers) and thermal light sources such as incandescent light bulbs. The Heisenberg uncertainty principle dictates that a state with an exact number of photons of a single frequency cannot be created. However, Fock states (or number states) can be studied for a system where the electric field amplitude is distributed over a narrow bandwidth. In this context, a single-photon source gives rise to an effectively one-photon number state. Photons from an ideal single-photon source exhibit quantum mechanical characteristics. These characteristics include photon antibunching, so that the time between two successive photons is never less than some minimum value [131].

In this chapter, we investigate how a route to the engineering of the electronic properties in the growth plane of a semiconductor can be achieved by exploiting the effect hydrogen has on dilute nitrides.

6.2 Nanostructure formation

Here, we explain the experimental procedure of forming InGaAsN:H nanostructures carried out by Sapienza University of Rome. We show that spatially-selective hydrogen irradiation allows for the realisation of ordered arrays of site-controlled InGaAsN quantum dots (QDs), whose optical properties have been broadly investigated by means of PL, time-resolved PL and photon correlation spectroscopy.

Selective hydrogenation:

The fabrication of nanostructure by means of utilising the hydrogen interaction with nitrogen in dilute nitride semiconductors is based on three key features [126]:

- (i) In order to be able to initiate the N-H interaction it is essential to introduce hydrogen into the sample in order to start the passivation process; it is not present to any significant level in the sample immediately after growth.

- (ii) There exists a range of temperatures for which the trapping rate of hydrogen by nitrogen is so fast that hydrogen atoms have little opportunity to diffuse into the material before they are captured by nitrogen. This causes an interaction-governed diffusion front profile.

- (iii) Hydrogen ions impinging on the sample can be effectively blocked before hitting it by a host of capping materials that either capture it and/or recoil it back.

These features, when combined, signify that if one covers only a portion of the sample's surface with a hydrogen-opaque material and then tries to implant hydrogen in it, hydrogen will diffuse primarily through and inside the exposed portions of the sample, leaving the covered ones with little to no hydrogen. As such hydrogen-opaque coverages can be layered selectively on the sample's surface, resulting in what is called a *mask*, so that the hydrogenation process is then selective. Hydrogenated and non-hydrogenated dilute nitride semiconductors should be regarded as different materials due to having different electronic and structural characteristics.

Sample patterning:

For making QDs based on an InGaAsN quantum well (QW), patterning the hydrogen-opaque material was done by e-beam lithography which allows patterning circles with diameters ranging from 900 nm down to 100 nm with an error of less than 5 nm. Fig. 6.1 shows scanning electron microscope (SEM) images of such a pattern made from hydrogen silsesqueoxane (HSQ), a hydrogen resistant material used as an e-beam resist, which was spun on top of a sample that had a single InGaAsN QW embedded 30 nm beneath its surface. The pattern included multiple areas with different mask circle diameter. This pattern was used for the fabrication of InGaAsN/InGaAsN:H QDs. Tailored doses of hydrogen were irradiated at different temperatures on pre-patterned samples in order to search for the optimal combination of H dose,

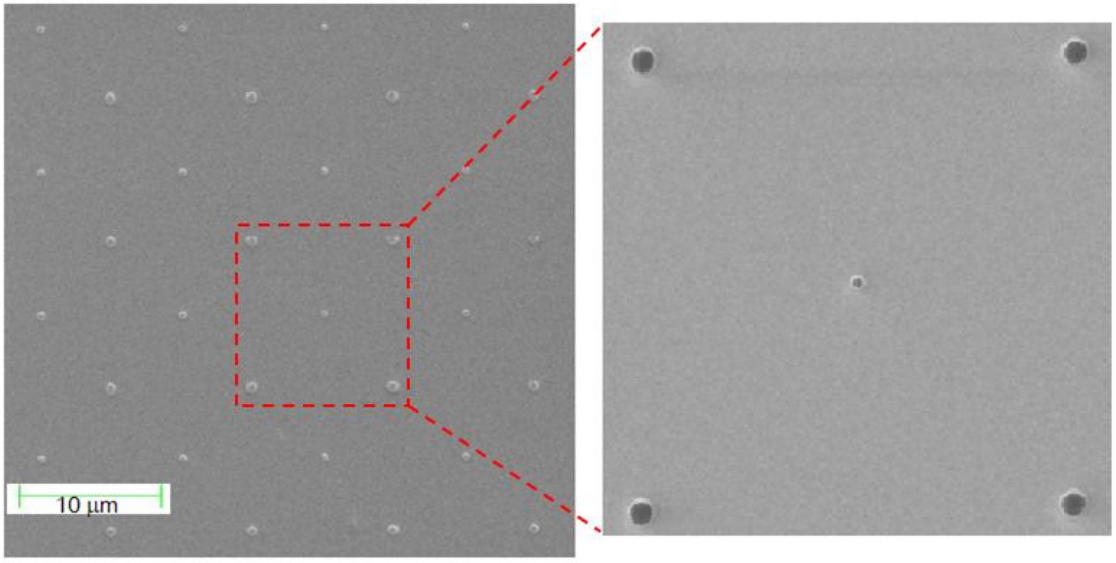


FIGURE 6.1: SEM image of the HSQ pattern used for the fabrication of quantum dots. The image on the right hand side displays a zoom-in of the area surrounded by the red square in seen the image on the left. The images were taken at Sapienza University of Rome

temperature and mask size that would result in creating the best dots. This hydrogenation technique allows the possibility of an accurate control of the implanted ion dose via the adjustment of the filament current – which determines the speed at which the process takes place – and the exposure time. Beam currents were varied between 18 to 29 μA while exposure times were varied between few minutes and up to 10 hours. Hydrogen doses in these samples were 10^{16} ions/cm^2 [131].

The reason why two mask sizes appear to be meshed together is that masks with diameter of less than 400 nm proved difficult to spot under the optical microscope when using a $\times 50$ (or a higher magnification) lens optimised for the infrared (lenses optimised for the infrared were used because they are better for passing infrared signal compared to lenses optimised for visible light). Consequently, masks with a 600 nm diameter were added to the pattern simply to act as markers for finding the location of the smaller ones. They also allowed faster calibration of the laser beam across the optical table (for obtaining optimum signal) utilising the fact that they were (usually, depending on the hydrogen dose) emitting much like a QW giving a relatively higher intensity signal.

6.3 Finite element simulations of selective hydrogen diffusion

Here, we discuss the process for realising the QDs in conjunction with finite element simulations that show the shape of the H-free nitrogen profile upon the hydrogenation process. Finite element simulations were carried out by Sapienza University of Rome using Comsol Multi-Physics

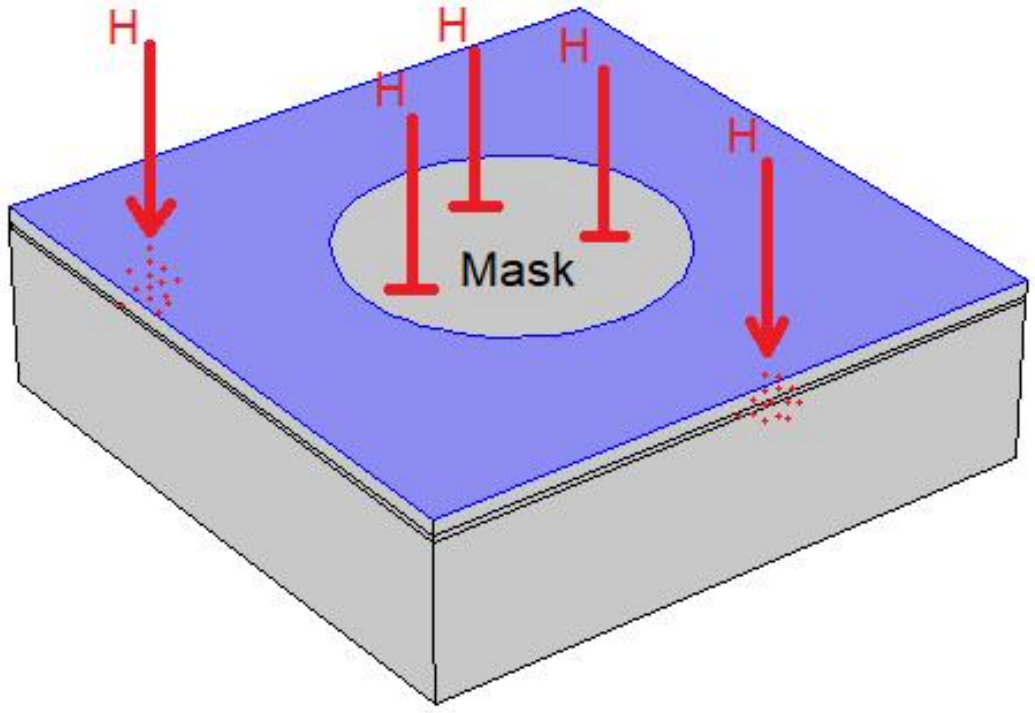


FIGURE 6.2: A 3D model used for the finite element simulations of selective H diffusion into a 6 nm-thick InGaAsN QW buried beneath a GaAs cap. Blue-coloured surface denotes the area of the theoretical sample that is exposed to the hydrogen flux (red arrows). The mask area has "zero" H flux (solid red lines).

software on a theoretical sample construction that consisted of a 6 nm $In_{0.21}Ga_{0.79}As_{0.975}N_{0.025}$ QW with different cap layer thicknesses on top of which, most importantly, an area-selective flux of hydrogen was implemented so as to resemble a hydrogen-opaque mask (c.f. Fig. 6.2). All the hydrogen impinging on the sample surface was assumed to penetrate into the sample and embed in it with zero kinetic energy [131].

Fig. 6.3 shows the H-free nitrogen profile for a set of simulations performed using different mask diameters, with different hydrogen doses for each simulation. The simulations were done in such a way that the resulting profile of N (colours other than dark blue within the QW) are of similar size (roughly $\sim$ 50 nm across the wide axis). This non-zero H-free N profile is in fact the profile of the InGaAsN QD embedded within the surrounding InGaAsN:H matrix around it. These simulations show that, when aiming to obtain a QD of a certain size (50 nm in diameter in the case shown) and provided with a sample that has a given cap thickness, making such a dot using a very small mask size results in a dot that is placed close to the bottom surface of the QW (Fig. 6.3(a)), while using a mask which is too big results in a dot which is placed close to the upper QW surface (Fig. 6.3(c)). Both these scenarios are not preferred as then surface-related states and defects will adversely harm the emission properties of the dot. An optimum mask size therefore exists for which the QD is placed in the centre of the QW and away from its surfaces (Fig. 6.3(b)).

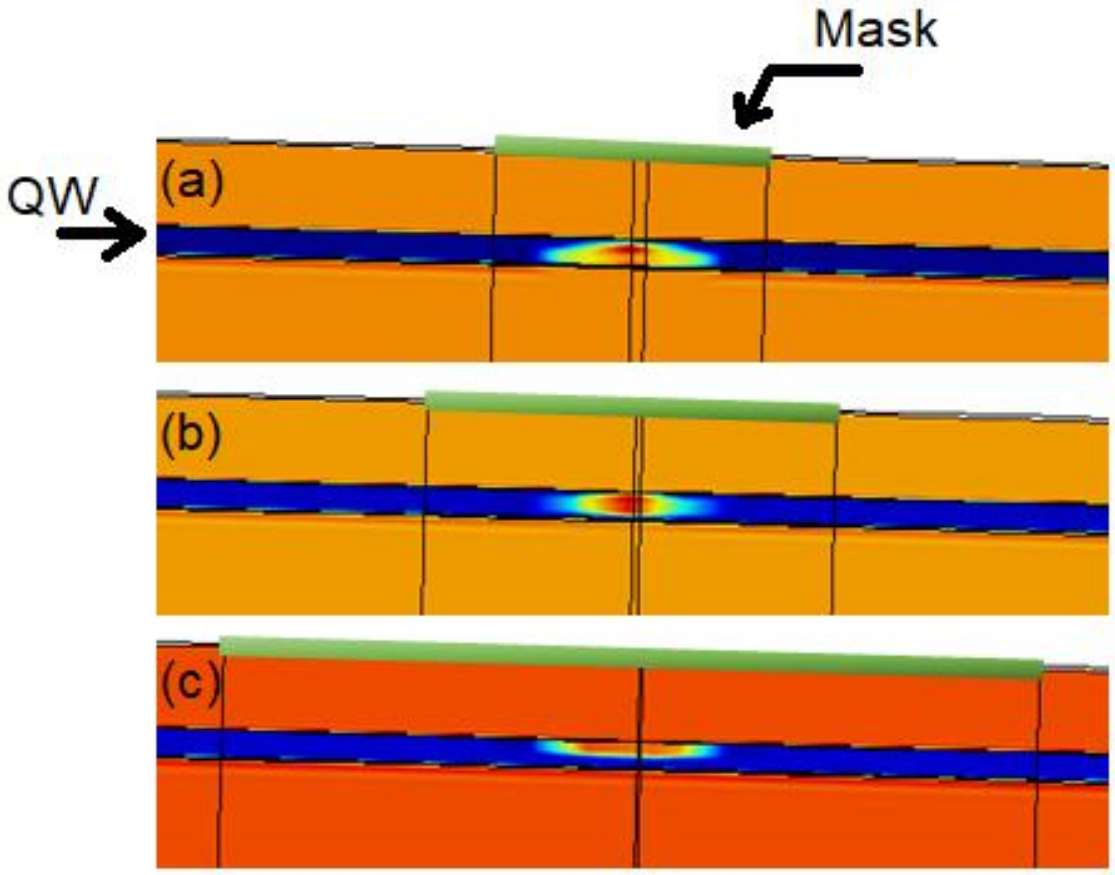


FIGURE 6.3: Simulations from Sapienza University of Rome showing the H-free nitrogen left in the QW (indicated with a horizontal arrow) after selective hydrogenation using a range of different mask sizes (indicated by thick light-green bars and a broken arrow), with different H doses tailored to each mask size so as to result in an H-free N profile of similar size. Dark-blue colour indicates fully passivated areas of the QW, green and yellow colour indicates partially passivated areas, and red indicates non-passivated areas. The relevant colours in the figure are only those inside the QW (colouring of the buffer and cap layers is meant for easier viewing only).

We also note that due to the finite thickness of the QW, whenever the QD is created close to one of its surfaces, its profile is also thinner (along the direction perpendicular to the plane of the well, resembling a disc shape), which is also an unwanted outcome as the dot modes will then be less well confined within its space.

6.4 Theory and experiment for InGaAsN:H quantum dots

In this section, we study the electronic band structure of the nanosctructures described in Sections 6.2 and 6.3. We benchmark the results of our calculations against experimental PL data investigating the existing InGaAsN:H/GaAs nanostructures. Fig. 6.4 shows a schematic of the structure considered. After hydrogenation, an ellipsoid-shaped InGaAsN QD is created

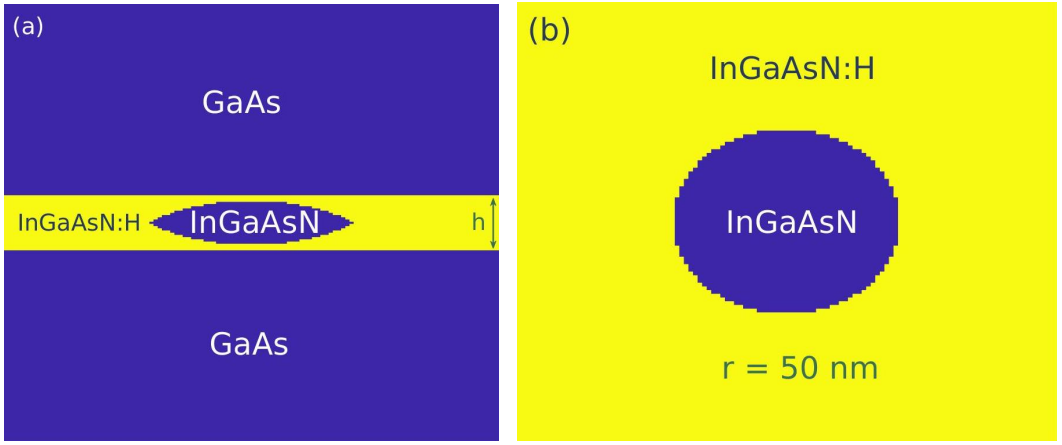


FIGURE 6.4: A line scan through the middle of the structure showing it from side view (a) and from top view (b).

inside an InGaAsN:H QW with a thickness of 6 nm grown on a GaAs matrix along the (001)-direction. The QD has a diameter of 50 nm in the x and y directions, and its height is 6 nm. The size of the supercell we consider in our calculations is 120×120×40 nm in the x, y, and z directions, respectively. Since the QD size in the x and y directions is large enough, a grid size of 1 nm should be sufficient in order to get a converged result. However, given the height of the dot in the z direction, a grid size of 0.2 nm is used in this direction. Hence, the size of the total mesh considered for the band structure calculations is 120×120×200 in the x, y, and z directions, respectively. We note that we have used a Gaussian smoothing to define the smooth degradation of N composition on the edges of the QD, which is in accordance with the simulated profile of the structure (c.f. Fig. 6.3(b)).

6.4.1 Strain distribution

Here, we analyse the strain distribution in the InGaAsN:H/GaAs nanostructures. Growing an InGaAsN QW on a GaAs substrate results in a compressive strain in the well, due to the well having a larger lattice constant than that of GaAs. Although the procedure of hydrogenation removes the effect of the localised nitrogen state in the conduction band of the host material on the conduction band edge, the lattice constant and the elastic parameters of the well are not changed by the process of hydrogenation [126]. This means that calculating the strain distribution of an InGaAsN QW with GaAs barriers in 1D is sufficient for further calculations of the electronic properties of InGaAsN:H/GaAs QDs.

It is reasonable to assume that the strain in the thin semiconductor layers is homogeneous and therefore constant throughout the layer [6]. Though no stress exists in the growth direction the lattice constant is still forced to change due to the Poisson effect. The compressive strain in the well associated with the presence of InGaAsN forces the lattice constant in the plane to

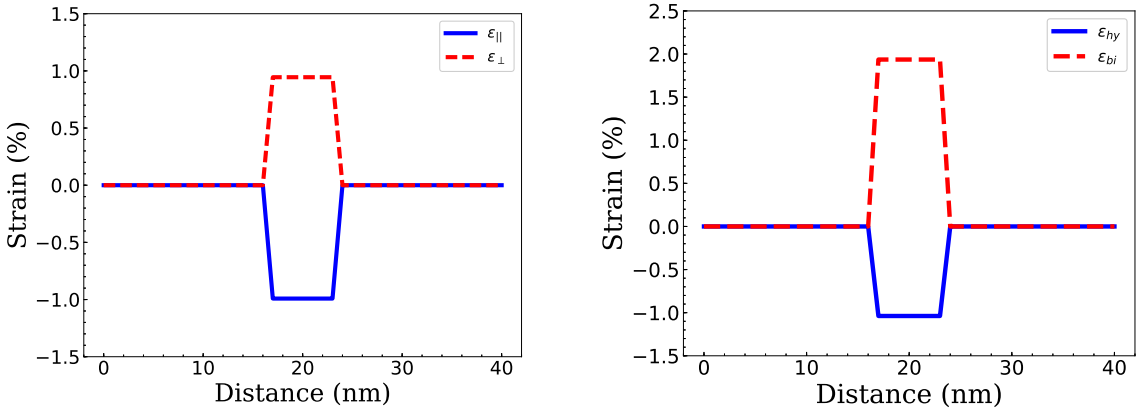


FIGURE 6.5: Calculated in-plane and out of plane strain component of the strain tensor along the (001)-direction (left panel). Calculated hydrostatic strain $\epsilon_{hy} = \epsilon_{xx} + \epsilon_{yy} + \epsilon_{zz}$ and biaxial strain ϵ_{bi} = ϵ_{zz} - $((\epsilon_{xx} + \epsilon_{yy})/2)$ along the (001)-direction (right panel). The (001)-direction is perpendicular to the plane of the InGaAsN layer.

shrink. More details on calculation of in-plane and out of plane strain in QWs is provided in Sec. 2.3.

Fig. 6.5 shows the calculated in-plane, out of plane, hydrostatic, and biaxial strain in a 6 nm $In_{0.21}Ga_{0.79}As_{0.975}N_{0.025}$ QW surrounded by GaAs barriers. The calculated hydrostatic and biaxial strains are used in determining the band lineups of the entire structure as will be discussed in Sec. 6.4.2.

In the Cartesian coordinate system, there is no shear strain, neither in the growth plane nor in the growth direction. The strains in the epitaxial layers are described as:

$$\epsilon_{xx} = \epsilon_{yy} = \epsilon_{||} = \frac{a_s - a_w}{a_w}, \tag{6.1}$$

where a_s is the substrate lattice constant, and a_w is the natural lattice constant of the QW material, with

$$\epsilon_{zz} = -2\frac{C_{12}}{C_{11}}\epsilon_{||}. \tag{6.2}$$

Or in matrix form:

$$\epsilon = \begin{bmatrix} \epsilon_{xx} & 0 & 0 \\ 0 & \epsilon_{yy} & 0 \\ 0 & 0 & \epsilon_{zz} \end{bmatrix},$$

where C_{11} and C_{12} are the QW elastic constants. We note that the hydrostatic strain $\epsilon_{hy} = \epsilon_{xx} + \epsilon_{yy} + \epsilon_{zz}$ and the biaxial strain $\epsilon_{bi} = \epsilon_{zz}$ - $((\epsilon_{xx} + \epsilon_{yy})/2)$ (which splits the valence band (VB) maximum into two separate bands of HH and LH) are shown in the right panel of Fig. 6.5 and are non-zero only in the InGaAsN QW. The resulting hydrostatic strain ϵ_{hy} and the biaxial strain ϵ_{bi} are important in determining the band lineups, as will be discussed in Sec. 6.4.2.

6.4.2 Band structure calculations

Here, we investigate the band lineups of $In_{0.21}Ga_{0.79}As_{0.975}N_{0.025}$:H/GaAs nanostructures. We analyse the effect of strain on the band lineups of the structure along the (001) and $(1\bar{1}0)$ directions through the centre of the dot. In addition to the effects of strain on the band lineups, we also need to consider the impact of localised nitrogen states on the calculated band lineups. The effect of the calculated strains and of the localised nitrogen states on the CB, HH, LH, and SO band edge energies are given by [12]:

$$E_{CB} = E_{c0} + a_c(\epsilon_{xx} + \epsilon_{yy} + \epsilon_{zz}) - \alpha x \tag{6.3}$$

$$E_{HH} = E_{v0} + a_v(\epsilon_{xx} + \epsilon_{yy} + \epsilon_{zz}) + b_v(0.5\epsilon_{xx} + 0.5\epsilon_{yy} - \epsilon_{zz}) + \kappa x \tag{6.4}$$

$$E_{LH} = E_{v0} + a_v(\epsilon_{xx} + \epsilon_{yy} + \epsilon_{zz}) - b_v(0.5\epsilon_{xx} + 0.5\epsilon_{yy} - \epsilon_{zz}) + \kappa x \tag{6.5}$$

$$E_{SO} = E_{v0} + a_v(\epsilon_{xx} + \epsilon_{yy} + \epsilon_{zz}) - \Delta_{SO} + \kappa x \tag{6.6}$$

In these equations, E_{c0} and E_{v0}, respectively, refer to the unstrained CB and VB edge of the host material. The CB and VB deformation potentials are shown with a_c and a_v. Also, α and κ describe how the CB and VB edges of unstrained $In_yGa_{1-y}As_{1-x}N_x$ shift with N composition x with respect to those of the GaAs barrier. Similarly, for the localised nitrogen band we write:

$$E_N = E_{CB} + \Delta E_{Nc} - \gamma x + \kappa x, \tag{6.7}$$

where ΔE_{Nc} is the energy separation between the nitrogen resonant level and the bottom of the host material conduction band, and γ describes the assumed shift of the N level with respect to the $In_yGa_{1-y}As$ VB edge. The BAC parameters used in our calculations are listed in Table 6.1 [12, 37]. We use a linear interpolation when using these parameters in our calculations.

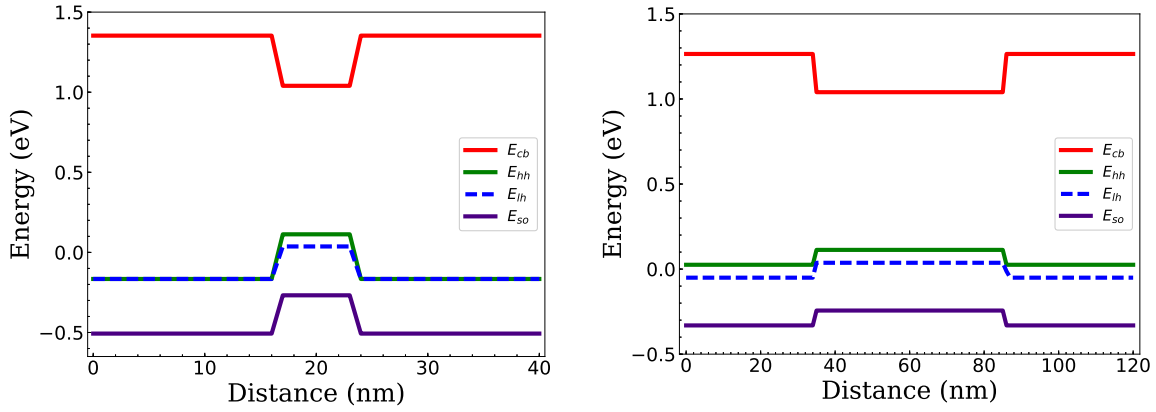


FIGURE 6.6: Calculated band lineups along the (001)-direction (left panel) and (1$\bar{1}$0)-direction (right panel).

Material	ΔE_{Nc} (eV)	β (eV)	α (eV)	κ (eV)	γ (eV)
InAs	0.969	1.212	1.41	3.0	3.0
GaAs	0.187	2.0	1.55	3.0	3.0

TABLE 6.1: BAC parameters used in our calculations.

To investigate the band structure of III-V dilute nitride semiconductors, it is sufficient to account for the BAC effect of the N levels with the CB states and treat the VB separately [84]. Our theoretical model to calculate the CB electronic structure of InGaAsN heterostructures is based on a 2-band BAC Hamiltonian [84]. However, to treat the VB, we use the conventional 6-band basis set including the LH, HH and SO bands [40, 42]. Fig. 6.6 shows a line scan of the calculated band lineups at $T = 5\ K$ through the centre of the QD (cf. Fig. 6.4) along the (001)-direction (left panel) and (1$\bar{1}$0)-direction (right panel). Using the full numerical band structure calculations as outlined in Sec. 2.4 we obtain the confined electron and hole states in the CB and VB, respectively. Assuming $T = 5\ K$, we calculate the transition energy equal to $e_1 - hh_1$ = 1.1199 - 0.0857 = 1.0342 eV which is equivalent to 1.199 μm emission. This is in a very good agreement with the experimental data provided by Sapienza University of Rome reporting the existing structure to have a peak of PL data at 1.2 μm.

Before the hydrogenation process (as discussed in Sections 6.2 and 6.3), the nanostructure is essentially an $In_{0.21}Ga_{0.79}As_{0.975}N_{0.025}$/GaAs QW structure. The calculated transition energy of this QW structure at $T = 5\ K$ is 0.962 eV, equivalent to 1.29 μm. We note that the calculated transition energy increases by 72 meV after the hydrogenation process and creating an ellipsoid-shaped QD inside the QW – cf. Fig. 6.3. A non-linear Gaussian interpolation has been used to deine the alloy composition close to the boundary of the hydrogenated QD and its surrounding for an accurate modelling of the structure according to the simulations made by Sapienza University of Rome. Using the band gap temperature dependence of InGaAsN as recommended by Ref. [132], we calculate a transition energy of 0.906 eV $\equiv$ 1.37 μm for this

QW at room temperature.

6.5 Template model for single photon sources emitting at telecommunication wavelengths

As mentioned earlier in this chapter, the main aim of designing hydrogenated InGaAsN/GaAs heterostructures in the PROMIS[1] project was for single photon sensing at the telecommunication wavelength of 1.31 μm. Although the existing structure that we have considered in Section 6.4 emits at $\lambda \cong 1.2$ μm, there should be scope to design structures emitting at $\lambda \cong 1.31$ μm using the same material platfrom. Increasing InAs content up to 30 % (a reasonable content to remain within the critical thickness limits) and/or nitrogen to 2.6 % could provide a solution to this, given that they both will result in decreasing the band gap energy and consequently in increasing the emission wavelength. Also, increasing the height of the QW would also confine the carriers more effectively, so as to allow the design of the structures to emit at higher wavelengths.

In order to provide a design template for $In_yGa_{1-y}As_{1-x}N_x$/GaAs nanostructures, we investigate impact of varying x, y, and the height of the QW, h. For a given x and h, y is varied to see how the transition energy varies as a function of the composition and the height of the QD. Increasing either x or y will shrink the band gap energy of the $In_yGa_{1-y}As_{1-x}N_x$ QD due to: (i) InAs having a smaller band gap energy than that of GaAs, (ii) increasing nitrogen content reduces the band gap energy of the host III-V semiconductor, due to the BAC effect [12, 37, 84].

Fig. 6.7 shows the calculated emitting wavelength λ as a function of InAs content y for $x = 2.5$, 2.6 % and $h = 6$ nm, 8 nm, and 10 nm. One can conclude that emitting at a wavelength of $\lambda \approx 1.31$ μm should be achievable by appropriately choosing the composition and the height of the QD. Looking at this figure, one can quickly notice that using the structures with thicker QW and higher y and x are necessary in order to achieve an emission of $\lambda \approx 1.31$ μm. Although increasing the QW thickness h plays a significant role when increasing from 6 nm to 8 nm, little additional benefit is gained by going to a thicker QW thickness with $h = 10$ nm.

In 2003, Tomić *et al* [12] investigated the use of $In_{0.36}Ga_{0.64}As_{0.983}N_{0.017}$/GaAs QW structures for emission at 1.3 μm. Even though the existing structures prepared by Sapienza University of Rome have not achieved emission at telecommunication wavelengths, nevertheless we have shown that there is a scope to design hydrogenated $In_yGa_{1-y}As_{1-x}N_x$/GaAs nanostructures to emit at $\lambda \approx 1.31$ μm. We showed in Sections 6.2 and 6.3 how the hydrogenation process and using a mask leaves an ellipsoid-shaped InGaAsN QD inside the QW. Given the lower band

[1] http://www.physics.lancs.ac.uk/promis/

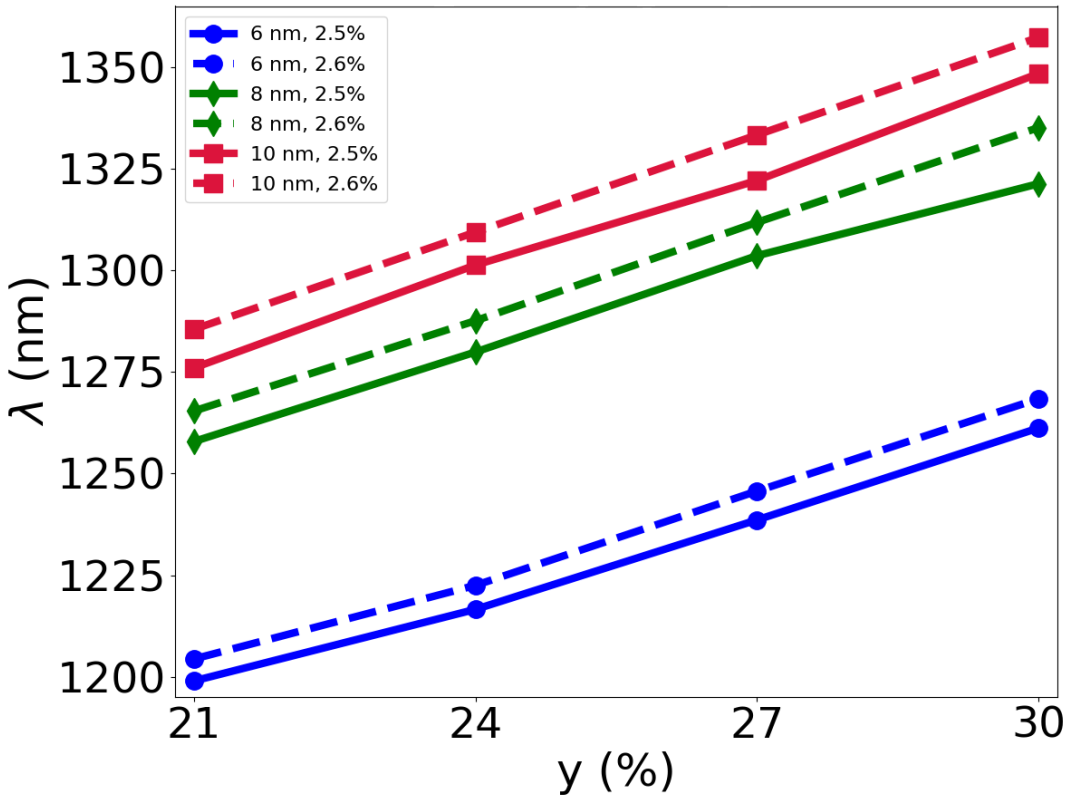


FIGURE 6.7: Design template for $In_yGa_{1-y}As_{1-x}N_x$/GaAs nanostructures emitting at $\lambda \approx 1.31$ μm at $T = 5$ K.

gap energy of QW structures compared to QD structures (essentially using the same material system) due to the quantum mechanical confinement factor, this therefore requires a QW which emits at longer wavelengths. We calculate a transition energy of 0.796 eV, equivalent to 1.55 μm emission, at room temperature for an $In_{0.3}Ga_{0.7}As_{0.974}N_{0.026}$/GaAs QW structure, with h = 10 nm. Fig. 6.7 shows that 1.31 μm QD emission can be achieved using an 8 nm QW with that composition. Given that the room temperature emission wavelength of this 8 nm QW will be at a wavelength that is shorter than 1.5 μm, and also that room temperature laser emission has been achieved from InGaAsN at 1.5 μm and longer wavelengths, we therefore conclude that low temperature 1.31 μm QD emission should therefore be achievable using hydrogenated $In_yGa_{1-y}As_{1-x}N_x$/GaAs nanostructures.

6.6 Summary and conclusions

In this chapter, we have presented a theoretical investigation and optimisation of the electronic properties of InGaAsN:H/GaAs nanostructures for use as single photon emitters operating at telecommunication wavelength λ=1.31 μm. We have considered the existing structures grown

by Sapienza University of Rome to benchmark our theoretical calculations against experimental photoluminescence data. Studying the band structure of $In_{0.21}Ga_{0.79}As_{0.975}N_{0.025}$:H/GaAs nanostructures, we theoretically calculated an emission wavelength $\lambda = 1.199$ μm, showing a very good agreement with experimental data provided by Sapienza University of Rome reporting an emission equal to 1.2 μm.

Having benchmarked our theoretical model against experimental data, we have provided a design template for $In_yGa_{1-y}As_{1-x}N_x$/GaAs nanostructures to emit at telecommunication wavelength $\lambda = 1.31$ μm by varying the composition and geometry of the structure. We have shown there is a wide scope for the proposed material platform and geometry to design single photon emitters to operate at $\lambda = 1.31$ μm at low temperatures. This requires structural and band gap engineering of $In_yGa_{1-y}As_{1-x}N_x$/GaAs nanostructures; showing the existing trade-off between increasing QW height h from 6 nm to 10 nm and N composition x from 2.5% to 2.6%. We concluded that wider QWs, $\geq$ 8 nm , are required to achieve $\lambda = 1.31$ μm. Additionally, we found that designing these $In_yGa_{1-y}As_{1-x}N_x$/GaAs nanostructures to emit at telecommunication wavelength $\lambda = 1.5$ μm to operate at room temperature requires significant increase in N composition which is challenging in growth point of view. Also, laser emission of these nanostructures has been realised to be problematic at room temperature. All in all, our calculations in this chapter provide a design template for single photon light sources operating at telecommunication frequencies.

Chapter 7

Summary, conclusions and outlook

In this final chapter we present our summary, conclusions and outlook. We briefly summarise the main results presented in the thesis in Sec. 7.1. This is followed in Sec. 7.2 by an overview of possible directions for future research, based on the work in this thesis.

7.1 Summary and conclusions

In this thesis we performed theoretical analysis and optimisation of quantum well (QW) light emitting diode (LED) structures emitting at mid-infrared wavelength region, and also investigated quantum ring (QR) intermediate band solar cells (IBSCs), and quantum dot (QD) single photon emitters to operate at the telecommunication wavelength of 1.31 μm.

In Chapter 2 we have presented the theoretical background which will be relevant to the study of the electronic and optical properties of nitrogen-free and dilute nitride III-V semiconductor materials. We then presented in Chapter 3 a theoretical investigation and optimisation of the optical properties of 3.3 μm InAsSb QWs grown on AlInAs metamorphic buffer layers (MBLs). By quantifying the scope offered by this material system to use strain and band structure engineering we demonstrated that there is large scope for the design of QW structures, incorporating compressively strained ternary InAsSb QWs having unstrained or tensile strained ternary AlInAs barriers. Such QWs combine large type-I band offsets with emission wavelengths $\lambda \sim 3.3$ μm, offering the possibility to design devices having high optical efficiency and reduced temperature sensitivity, and making these structures particularly appealing for the development of mid-infrared LEDs. We have defined design criteria to achieve strain-balanced QWs at a desired emission wavelength, thereby providing a general method which can be applied to produce candidate multi-QW or superlattice structures for epitaxial growth and experimental investigation. Via a systematic analysis of strain-balanced structures designed to emit at 3.3 μm we identified key trends in their properties and performance as functions of alloy composition,

QW thickness and epitaxial strain. Overall, our theoretical analysis has identified important trends in the performance of GaAs-based metamorphic QW LEDs operating at mid-infrared wavelength, has provided guidelines for the growth of optimised devices suitable for practical applications, and has confirmed the promise of these novel metamorphic heterostructures for the development of high-performance mid-infrared light emitting sources.

In Chapter 4 we presented a theoretical investigation to guide optimisation of the optical properties of 4.2 μm InNAsSb QWs grown on AlInAs MBLs. Analysing the bulk composition space map of this material system, we have argued that using dilute nitride $InN_y(As_{1-x}Sb_x)_{1-y}$ is key to achieve emission beyond 4 μm. By quantifying the scope offered by this material system to use strain and band structure engineering we demonstrated that there is large scope for the design of QW structures, incorporating compressively strained quaternary $InN_y(As_{1-x}Sb_x)_{1-y}$ QWs having tensile strained ternary $Al_zIn_{1-z}As$ barriers. Such QW structures can combine large type-I band offsets with emission wavelengths $\lambda \sim 4.2$ μm, and hence offering the possibility to design devices having high optical efficiency and reduced temperature sensitivity. We presented design criteria to achieve strain-balanced quaternary QWs at a desired emission wavelength, thereby providing a general method which can be applied to produce candidate quaternary multi-QW or superlattice structures for epitaxial growth and experimental investigation. Via a systematic analysis of strain-balanced structures designed to emit at 4.2 μm we identified key trends in their properties and performance as a function of alloy composition, QW thickness and epitaxial strain, while considering growth on two different metamorphic buffer layers. Overall, our theoretical analysis has identified important trends in the performance of GaAs-based metamorphic QW LEDs operating at $\lambda = 4.2$ μm, providing guidelines for the growth of optimised devices suitable for practical applications, and pointing to the promise of these novel metamorphic heterostructures for the development of high-performance mid-infrared light emitters.

In Chapter 5 we have presented a theoretical investigation of the electronic properties of type-II $GaAs_{1-x}Sb_x$/GaAs QR structures based on analytical and numerical approaches, and identified optimised combinations of QR morphology and alloy composition for the realisation of hole-based IBSCs – in which the intermediate band is formed by the highest energy bound hole state in the QR – offering the maximum theoretical efficiency available via inclusion of an intermediate band (IB) in a GaAs matrix. Analytically, we presented the solution of the time-independent Schrödinger equation for a cylindrical QR of infinite potential depth and derived a transcendental equation which must be satisfied by bound QR eigenstates. The relationship to the solution of the well-known problem of the cylindrical QD was described, and it was demonstrated that (i) the QR eigenstates evolve smoothly from those of the QD, and (ii) the convergence properties of the QR ground state allow the confinement energy to be estimated straightforwardly, and to high accuracy, for realistic QRs having dimensions

typical of those achieved via epitaxial growth. Our analytical analysis demonstrated that type-II $GaAs_{1-x}Sb_x$/GaAs QRs offer significant benefits from the perspective of band structure engineering for IBSC applications, allowing the IB energy in a hole-based IBSC to be tuned across a broad range via changes in QR morphology. Numerically, we used multi-band $\mathbf{k}\cdot\mathbf{p}$ calculations – including full strain and piezoelectric effects – to analyse the electronic properties of $GaAs_{1-x}Sb_x$/GaAs QRs, both as a function of QR dimensions and Sb composition. We further demonstrated that the nature of the carrier confinement in these heterostructures is ideally suited to IBSC applications. Strong hole localisation can be expected to mitigate carrier leakage from the IB via thermionic emission. Additionally, the interplay between strain relaxation and type-II band alignment in these QRs was demonstrated to give rise to electron states which, in the plane of the QR, are strongly localised in the central barrier of the QR. The unusual nature of the carrier localisation in these heterostructures suggests the potential to engineer the trade-off between the electron-hole overlap (which mediates carrier generation via optical absorption) and the radiative lifetime for photo-generated electron-hole pairs (which mediates carrier loss via radiative recombination). Given the sensitivity of the theoretical IBSC efficiency to the IB energy, our analysis suggests that careful control of QR morphology provides a viable route to realising optimised heterostructures suitable for IBSC applications. All in all, we highlighted the suitability of type-II $GaAs_{1-x}Sb_x$/GaAs QRs for applications in hole-based IBSCs, and provided optimised combinations of QR alloy composition and morphology to guide the growth and fabrication of prototype QR-IBSC devices.

In Chapter 6 we have presented a theoretical investigation and optimisation of the electronic properties of InGaAsN:H/GaAs nanostructures for the use as single photon emitters operating at the telecommunication wavelength λ=1.31 μm. We have used the existing structures prepared by Sapienza University of Rome to benchmark our theoretical method against experimental photoluminescence data. Studying the band structure of $In_{0.21}Ga_{0.79}As_{0.975}N_{0.025}$:H/GaAs nanostructures, we theoretically calculated an emission wavelength $\lambda = 1.199$ μm, showing a very good agreement with experimental data provided by Sapienza University of Rome reporting an emission equal to 1.2 μm. Having benchmarked our theoretical model against experimental data, we have provided a design template for $In_yGa_{1-y}As_{1-x}N_x$/GaAs nanostructures to emit at telecommunication wavelength $\lambda = 1.31$ μm by varying the composition and geometry of the structure. Overall, we have shown that with the feasibility of the proposed templates confirmed by comparison with previously demonstrated laser structures the proposed material platform and geometry should provide a viable route to design single photon emitters operating at $\lambda = 1.31$ μm.

7.2 Outlook

We now present some possible directions towards which research presented in this thesis can be extended.

For our analysis of electronic and optical properties of metamorphic QW LEDs emitting at mid-infrared wavelength region, outlined in Chapters 3 and 4, we considered strain-balanced nitrogen-free InAsSb/AlInAs and dilute nitride InNAsSb/AlInAs QW LEDs emitting at 3.3 μm and 4.2 μm, respectively. Identifying key trends in their electronic and optical properties, we calculated their spontaneous emission spectra and the associated radiative current density at a fixed injected carrier density. A possible way to further this research is to calculate their internal photon flux, output power, external quantum efficiency, and responsivity by modelling the entire structure. Our analysis in Chapters 3 and 4 ignored the role of Auger recombination in these mid-infrared LEDs. We justify this by a comparison between one theoretical analysis and a series of experimental structures grown at University of Lancaster and University of Cadiz. This showed that the trends observed in the experimental emission were well reproduced by our radiative emission rate calculations. Nevertheless, it is to be expected that Auger recombination is present in the LED structures, which should be considered in future estimates of the overall optical efficiency achievable in these structures.

In Chapter 5 we designed efficient GaAsSb/GaAs QR-based IBSCs by identifying optimised combinations of QR morphology and alloy composition. We were restricted to electronic band structure engineering of these structures having considered them as supercells. This research can be extended by analysing the effect of separation between QR arrays on the carrier confinement energy and the associated wavefunction. Evolution of wavefunction localisation as a function of this separation can be interesting in a sense that electron and hole wavefunction overlap plays a strong role in determining the overall performance of these devices, more detailed quantitative calculation of the wavefunctions overlap and predicted radiative recombination rate would therefore be useful. Another possible apprach towards extending the research presented in Chapter 5 is to calculate the band to continuum absorption, which is indeed useful to determine the overall efficiency of the device.

Finally, in Chapter 6 our analysis has established the potential of hydrogenated InGaAsN QD-based nanostructures for emission at the telecommunication wavelength $\lambda = 1.31$ μm. Further experimental work is now required to analyse and exploit this material system for single photon emission in this important wavelength range.

Appendix A

Material parameters

In this appendix we present the material parameters used in the calculations of electronic and optical properties of In(N)AsSb/AlInAs quantum well based light emitting diodes discussed in Chapters 3 and 4, Ga(As)Sb/GaAs quantum ring based intermediate band solar cells discussed in Chapter 5, and InGaAsN/GaAs nanostructures discussed in Chapter 6. In Section A.1 we discuss the chosen material parameters for AlAs, InAs, InSb, GaSb, and GaAs binaries. Then we explain the interpolation we have used to obtain the related material parameters for ternary AlInAs, InAsSb and GaAsSb alloys. Finally, in Section A.2 we discuss the chosen material parameters for dilute nitride InNAs and InNSb alloys required for the band-anticrossing model as explained in 2.4.

A.1 Overview of material parameters for nitrogen-free alloys

In this section we outline the material parameters of binary AlAs, InAs, InSb, GaSb and GaAs materials and ternary AlInAs, InAsSb, GaAsSb and InGaAs alloys we have used in our calculations. Most of the material parameters we have used are taken from Ref. [69]. For most of the material parameters used in our calculations, we use a linear interpolation between the binary materials AlAs, InAs, InSb, GaSb, and GaAs to obtain the relevant material parameters for the ternaries. However, for the band gap energy E_g and split-off energy Δ_{SO} of a ternary alloy of the form AB_xC_{1-x} we use the interpolation scheme recommended by Ref. [133]:

$$T_{ABC}(x) = xB_{AB} + (1-x)B_{AC} + x(x-1)C_{ABC}, \tag{A.1}$$

where C_{ABC} is the bowing parameter. Table A.1 presents the material parameters of the AlAs, InAs, InSb, GaSb, and GaAs binaries. We note that the reported band gap energies E_g are the values at $T = 0K$. In cases where we needed to perform the calculations at a finite

Parameter	AlAs	InAs	InSb	GaSb	GaAs
$E_g\ (eV)$	3.099	0.417	0.235	0.812	1.519
$a_l\ (\AA)$	5.661	6.058	6.479	6.096	5.653
$\Delta_{SO}\ (eV)$	0.28	0.39	0.81	0.76	0.341
$\alpha\ (meV/K)$	0.70	0.276	0.32	0.417	0.46
$\beta\ (K)$	530	93	170	94	204
m_e^*	0.15	0.026	0.014	0.039	0.067
γ_1	3.76	20.0	34.8	13.4	6.98
γ_2	0.82	8.5	15.5	4.7	2.06
γ_3	1.42	9.2	16.5	6.0	2.93
$E_P\ (eV)$	21.1	21.5	23.3	27.0	28.8
$a_c\ (eV)$	-5.64	-5.08	-6.94	-7.5	-7.17
$a_v\ (eV)$	-2.47	-1.0	-0.36	-0.8	-1.16
$b\ (eV)$	-2.3	-1.8	-2.0	-2.0	-2.0
$d\ (eV)$	-3.4	-3.6	-4.7	-4.7	-4.8
$c_{11}\ (GPa)$	125	83.29	684.7	884.2	122.1
$c_{12}\ (GPa)$	53.4	45.26	373.5	402.6	56.6
$c_{44}\ (GPa)$	54.2	39.59	311.1	432.2	60.0

TABLE A.1: Material parameters for the binary materials used as input to the **k.p** calculations.

Bowing parameter	AlInAs	InAsSb	GaAsSb	InGaAs
$E_g\ (eV)$	0.70	0.938	1.43	0.477
$\Delta_{SO}\ (eV)$	0.15	0.0	0.60	0.15

TABLE A.2: Bowing parameters for ternary materials used in the **k.p** calculations.

temperature T, we have used the Varshni equation to obtain the relevant value of E_g with the Varshni parameters taken from Ref. [68]. Even though these material parameters are reported and used widely, it appears that the literature lacks a consistent set of bowing parameters for the band gap energy and split-off energy of ternary alloys. Table A.2 shows the band gap energy and split-off energy bowing parameters of AlInAs, InAsSb ,GaAsSb and InGaAs we have used in our calculations. We have found the bowing parameters for AlInAs, GaAsSb and InGaAs ternary alloys recommended by Ref. [69] to be reliable when benchmarking our **k.p** calculations against experimental data. However, for the InAsSb ternary alloy we have used a band gap bowing of 0.938 eV, as recommended by Ref. [134], and have set the bowing of the valence band spin–orbit splitting energy to zero. This choice of material parameters has been benchmarked against experimental measurements, where we find that it quantitatively describes the dependence on Sb composition and temperature of the measured photoluminescence emission peak energy in a range of type-II InAsSb/AlInAs quantum well and superlattices. We also note that the valence band offsets used in our band structure calculations are calculated using model solid theory as outlined in Ref. [135], where (i) the average valence band energies have been chosen to reproduce a natural (unstrained) valence band offset, and (ii) and (ii) the approach of Ref. [133] is used to compute the bowing of the alloy average valence band energy.

Material	ΔE_{Nc} (eV)	β
InAs	0.969	1.212
InSb	0.485	1.97
GaAs	0.187	2.0

TABLE A.3: Band-anticrossing parameters used in our calculations.

A.2 Overview of dilute nitride material parameters

We have used the band-anticrossing model to study the impact of localised nitrogen states on the electronic structure of InNAsSb and InGaAsN alloys. In this section we summarise the material parameters we have used in our electronic band structure calculations of these dilute nitride semiconductors. The values of ΔE_{Nc} and β for isolated, substitutional N impurities used in our calculations are summarised in Table A.3 for InAs, InSb and GaAs semiconductors [37], where ΔE_{Nc} is the energy of the N-related localised states relative to the host matrix conduction band edge energy. We have then used a linear interpolation to calculate the relevant parameters for the InNAsSb and InGaAsN alloys discussed in Chapter 4 and Chapter 6, respectively.

Appendix B

Short guide to running S/PHI/nX

We have used the S/PHI/nX freeware library for the electronic band structure calculations of GaAsSb/GaAs quantum rings and hydrogenated InGaAsN QD-based heterostructures, discussed in Chapter 5 and Chapter 6, respectively. Here we briefly explain the procedure we have used to model the aforementioned heterostructures in S/PHI/nX. Figure B.1 shows a flowchart of how the S/PHI/nX software works.

We can summarise the steps required to undertake electronic band structure calculations of a given nanostructure using S/PHI/nX as follows:

1. The three-dimensional structure (as a geometry file), simulation cell, and material parameters are defined. Grid sizes along the x, y and z directions are defined in the input files "strain.sx" for strain calculations and "input.sx" for band structure calculations so as to ensure to obtain accurate results. Fig. B.2 shows the script we have used to define GaAs material parameters used in our **k.p** calculations. We note that the units in S/PHI/nX software library are defined in the Hartree atomic units system. We have defined the material parameters introduced in Sec. 2.4. We can use a similar approach to define binary zincblende materials. However, for ternary and quaternary zincblende alloys we need to use linear interpolation to define the parameters for the compounds. We note that the band gap energy and the split-off energy are defined with a bowing parameter for the ternary and quaternary alloys.

2. Strain profile and built-in piezoelectric potential are subsequently calculated using continuum elasticity theory [32]. Piezoelectric potential is defined in the input file "peField.pol". Output files are written in "strainXX.dat", "strainYY.dat", "strainZZ.dat", "strainXY.dat", "strainXZ.dat", "strainYZ.dat", and "vPol.dat" that contain the corresponding component of the strain tensor and the polarisation in a format similar to the format of the defined geometry file. The output files are easy-to-interpret in a 3D-visualiser. Nevertheless, "data001.dat" contains a line-scan through the centre of the cell along the (001)-direction of relevant elastic and piezoelectric properties.

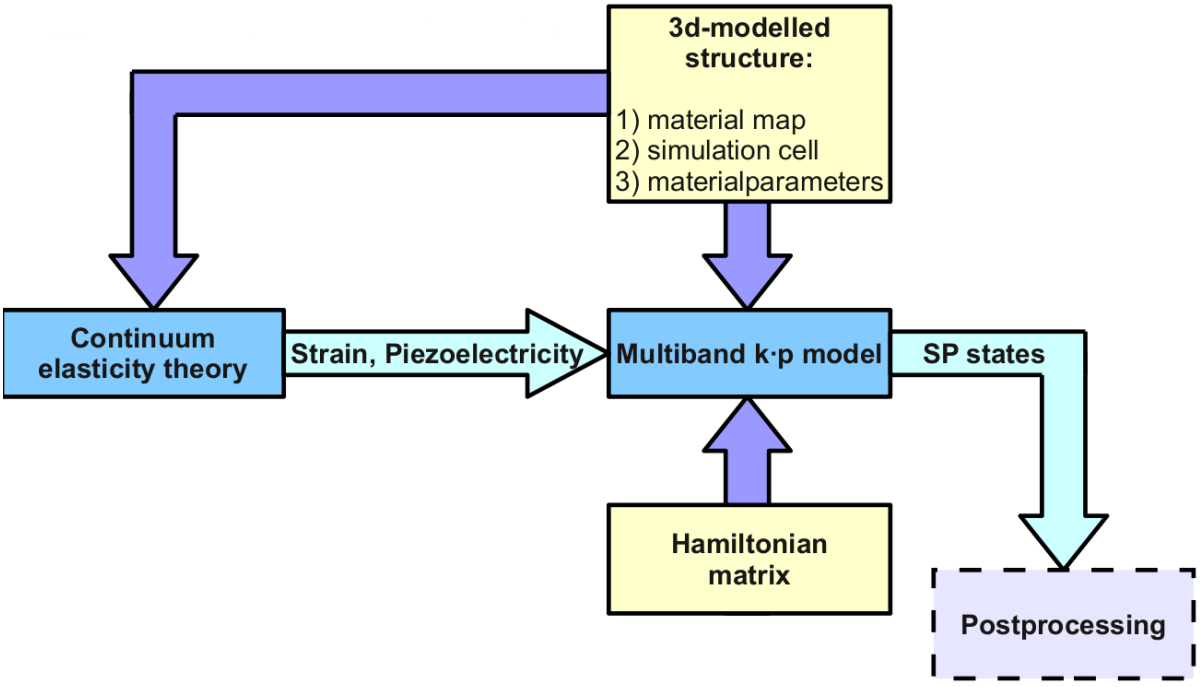


FIGURE B.1: S/PHI/nX flowchart to define a nanostructure and Hamiltonian for electronic band structure calculations.

3. The Hamiltonian matrix is defined. Fig. B.3 shows the script used to define a 10-band **k.p** Hamiltonian as described in Sec. 2.4.2.

4. Finally, the multiband **k.p** method is implemented to calculate the single particle states. When setting up, we can specify how many carrier states to calculate in the input file "hamiltonian.sx". The input file "eTrial.sx" is then defined close to the estimated conduction/valence band edge of the dot in order to calculate electron/hole states. We note that electron and hole states are calculated in separate calculations by properly defining the trial energy in the input file "eTrial.sx". Fig. B.4 shows how the trial energy is defined to solve for electron states in the conduction band of a heterostructure. Similarly, defining the trial energy close to the valence band edge energy solves for hole states in the valence band.

```
T = 300.0;

alpha = 0.0005405;
beta = 204;
Egg  = (1.519 - ( (alpha * T * T) / (T + beta)));
Eg = Egg / HA2EV;
Ep  = 28.8 / HA2EV;
dSO = 0.341 / HA2EV;
mh = 0.377;
me = 0.067;
gC  = 1./me - (Ep/3.) * (2./Eg + 1./(Eg + dSO));
corr = Ep / (3. * Eg + dSO);
VBO = -0.58;

parameterSet{
   material = "GaAs";
   parameter { name = "Ecb"   ; value = (Egg + VBO) /HA2EV;}
   parameter { name = "Evb"   ; value = VBO  /HA2EV;}
   parameter { name = "gammaC" ; value = gC;}
   parameter { name = "gamma1" ; value = 7.1 - corr;}
   parameter { name = "gamma2" ; value = 2.02 - 0.5 * corr;}
   parameter { name = "gamma3" ; value = 2.91 - 0.5 * corr;}
   parameter { name = "SO"; value = dSO;}
   parameter { name = "P0"; value = sqrt(Ep/2);}
   parameter { name = "me"; value = 0.067;}
   parameter { name = "sc"; value = (1/me) - ((Ep/3)*((2/Eg)+(1/(Eg+dSO))));}


   parameter { name = "ac"; value = -7.17/HA2EV;}
   parameter { name = "av"; value = -1.16/HA2EV;}
   parameter { name = "b"; value = -2.0/HA2EV;}
   parameter { name = "d"; value = -4.8/HA2EV;}

   parameter { name = "aLat"; value = 5.653;}
   parameter { name = "cLat"; value = 5.653;}
   parameter { name = "c11"; value = 1221;}
   parameter { name = "c12"; value = 566;}
   parameter { name = "c44"; value = 600;}
   parameter { name = "e14"; value = -0.23;}
   parameter { name = "b114"; value = -0.439;}
   parameter { name = "b124"; value = -3.765;}
   parameter { name = "b156"; value = -0.492;}
   parameter { name = "epsilon"; value = 13.18;}

   useForPreconditioner;
}
```

FIGURE B.2: The script used to define GaAs material parameters for **k.p** calculations using S/PHI/nX.

```
j=1.4142;
f=1.7321;

VNC = beta * sqrt(x);

ggg = 0.5 * (gamma2 + gamma3);
miu = 0.5 * (gamma3 - gamma2);



ECB = Ecb + ac * (eXX + eYY + eZZ) + (0.5 * sc * k2) + Vp;
EHH = Evb + ( av * (eXX + eYY + eZZ)) + ( 0.5 * b * (eXX + eYY - eZZ - eZZ)) - (0.5*gamma1*k2) - (0.5*gamma2*kx2) - (0.5*gamma2*ky2) + (gamma2*kz2) + Vp;
ELH = Evb + ( av * (eXX + eYY + eZZ)) - ( 0.5 * b * (eXX + eYY - eZZ - eZZ)) - (0.5*gamma1*k2) + (0.5*gamma2*kx2) + (0.5*gamma2*ky2) - (gamma2*kz2) + Vp;
Eso = Evb + ( av * (eXX + eYY + eZZ)) - SO - (0.5*gamma1*k2) + Vp;
te = (0.4082 * P0 * eXX * kx) + (0.4082 * P0 * i * eXY * kx) + (0.4082 * P0 * eXY * ky) + (0.4082 * P0 * i * eYY * ky) + (0.4082 * P0 * eXZ * kz) + (0.4082 * P0 * i * eYZ * kz);
tec = (0.4082 * P0 * eXX * kx) - (0.4082 * P0 * i * eXY * kx) + (0.4082 * P0 * eXY * ky) - (0.4082 * P0 * i * eYY * ky) + (0.4082 * P0 * eXZ * kz) - (0.4082 * P0 * i * eYZ * kz);
T = (0.4082 *P0 *kx) + (i * 0.4082 * P0 * ky) + te;
TC = (0.4082 * P0 *kx) - (i * 0.4082 * P0 * ky) + tec;
TT = (0.4082 * P0 * kx) - ( i * 0.4082 * P0 * ky) + tec;
TTC = (0.4082 * P0 * kx) + (i * 0.4082 * P0* ky) + te;
U = 0.5774 * P0 * kz + 0.5774 * P0 * eXZ * kx + 0.5774 * P0 * eYZ * ky + 0.5774 * P0 * eZZ * kz ;
S = (1.2247*gamma3*kxz) - (1.2247*gamma3*i*kyz) -  (0.7071 * d * eXZ) + (0.7071 * d * i * eYZ);
SC = (1.2247*gamma3*kxz) + (1.2247*gamma3*i*kyz) -  (0.7071 * d * eXZ) - (0.7071 * d * i * eYZ);
R = (0.866 * ggg * kx2) - (0.866 * ggg * ky2) - (1.7321 * i * ggg * kxy) - (0.866 * miu * kx2) - (0.866 * miu * ky2) - (1.7321 * i * miu * kxy) - ( 0.866 * b * (eXX - eYY)) + ( i * d * eXY);
RC = (0.866 * ggg * kx2) - (0.866 * ggg * ky2) + (1.7321 * i * ggg * kxy) - (0.866 * miu * kx2) - (0.866 * miu * ky2) + (1.7321 * i * miu * kxy) - ( 0.866 * b * (eXX - eYY)) - ( i * d * eXY);


Q = (1.41*gamma2*kz2) - (gamma2*0.7071*ky2) - (0.7071*gamma2*kx2) - (0.7071 * b * (eXX + eYY - eZZ - eZZ));



Hamiltonian=[[EN, VNC, 0, 0, 0, 0, 0, 0, 0, 0],
             [VNC, ECB, -f*T, j*U, -U, 0, 0, 0, -TT, -j*TT],
             [0, -f*TC, EHH, j*S, -S, 0, 0, 0, -R, -j*R],
             [0, j*U, j*SC, ELH, Q, 0, TC, R, 0, f*S],
             [0, -U, -SC, Q, Eso, 0, j*TC, j*R, -f*S, 0],
             [0, 0, 0, 0, 0, EN, VNC, 0, 0, 0],
             [0, 0, 0, T, j*T, VNC, ECB, -f*TT, j*U, -U],
             [0, 0, 0, RC, j*RC, 0, -f*TTC, EHH, j*SC, -SC],
             [0, -TTC, -RC, 0, -f*SC, 0, j*U, j*S, ELH, Q],
             [0, -j*TTC, -j*RC, f*SC, 0, 0, -U, -S, Q, Eso]];
```

FIGURE B.3: The script used to define 10–band **k.p** Hamiltonian for calculations using S/PHI/nX.

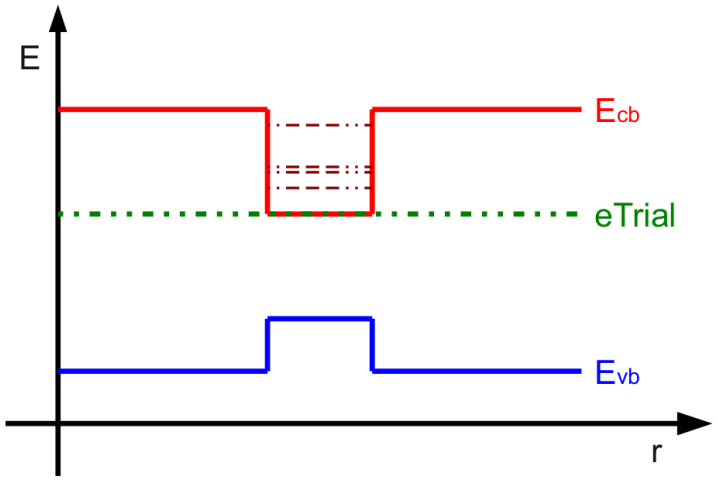


FIGURE B.4: Defining the trial energy close to the conduction band edge energy in order to solve for electron states in the conduction band.

Bibliography

[1] B. E. Saleh and M. C. Teich, eds., "Fundamentals of photonics" (John Wiley and Sons, 2019).

[2] J. Singh, ed., "Electronic and Optoelectronic Properties of Semiconductor Structures" (Cambridge: Cambridge University Press, 2003).

[3] D. Bimberg, M. Grundmann, and N. N. Ledentsov, eds., "Quantum Dot Heterostructures" (Chichester: Wiley, 2001).

[4] S. L. Chuang, "Physics of Photonic Devices" (Wiley, 2009).

[5] E. P. O'Reilly, "Valence band engineering in strained-layer structures," Semicond. Sci. Technol. **4**, 121 (1989).

[6] P. Harrison and A. Valvanis, eds., "Quantum wells, wires and dots: theoretical and computational physics of semiconductor nanostructures" (John Wiley and Sons, 2016).

[7] J. Piprek, ed., "Handbook of Optoelectronic Device Modeling and Simulation (Vol. 1)" (CRC Press, 2017).

[8] M. T. Björk, B. J. Ohlsson, C. Thelander, A. I. Persson, K. Deppert, L. R. Wallenberg, and L. Samuelson, "Nanowire resonant tunneling diodes," Appl. Phys. Lett. **81(23)**, 4458 (2002).

[9] M. Gonschorek, J. F. Carlin, E. Feltin, M. A. Py, and N. Grandjean, "High electron mobility lattice-matched Al In N/ Ga N field-effect transistor heterostructures," Appl. Phys. Lett. **89(6)**, 062106 (2006).

[10] S. J. Choi, D. Kostadin, S. J. Choi, P. D. Dapkus, W. Lin, G. Griffel, R. Menna, and J. Connolly, "Microring resonators vertically coupled to buried heterostructure bus waveguides," IEEE Photon. Tech. Lett. **16(3)**, 828 (2004).

[11] M. Fischer, M. Reinhardt, and A. Forchel, "GaInAsN/GaAs laser diodes operating at 1.52/spl mu/m," Electron. Lett. **36(14)**, 1208 (2000).

[12] S. Tomić, E. P. O'Reilly, R. Fehse, S. J. Sweeney, A. R. Adams, A. D. Andreev, S. A. Choulis, T. J. C. Hosea, and H. Riechert, "Theoretical and experimental analysis of 1.3 μm InGaAsN/GaAs lasers," IEEE J. Sel. Top. Quant. Electron. **9**, 1228 (2003).

[13] C. A. Broderick, S. R. Jin, I. P. Marko, K. Hild, P. Ludewig, Z. L. Bushell, W. Stolz, J. M. Rorison, E. P. O'Reilly, K. Volz, et al., "$GaAs_{1-x}Bi_x/GaN_yAs_{1-y}$ type-II quantum wells: novel strain-balanced heterostructures for gaas-based near- and mid-infrared photonics," Sci. Rep. **7**, 46371 (2017).

[14] R. Arkani, C. A. Broderick, and E. P. O'Reilly, "Computational design of metamorphic In (N) AsSb mid-infrared light-emitting diodes," in the proceedings of IEEE 18th International Conference on Nanotechnology (IEEE-NANO) **89(6)**, 1 (2018).

[15] P. S. Zory, ed., "Quantum Well Lasers" (Academic Press, 1993).

[16] C. A. Broderick, M. Usman, S. J. Sweeney, and E. P. O'Reilly, "Band engineering in dilute nitride and bismide semiconductor lasers," Semicond. Sci. Technol. **27**, 094011 (2012).

[17] N. Zettili, ed., " Quantum mechanics: concepts and applications" (John Wiley and Sons, 2003).

[18] D. Bimberg, M. Grundmann, and N. N. Ledentsov, eds., "Quantum dot heterostructures" (John Wiley and Sons, 1999).

[19] O. Stier, M. Grundmann, and D. Bimberg, "Electronic and optical properties of strained quantum dots modeled by 8-band $\mathbf{k}\cdot\mathbf{p}$ theory," Phys. Rev. B **59(8)**, 5688 (1999).

[20] A. Schliwa, M. Winkelnkemper, , and D. Bimberg, "Impact of size, shape, and composition on piezoelectric effects and electronic properties of in (ga) as/ ga as quantum dots," Phys. Rev. B **76**, 205324 (2007).

[21] S. Schulz, M. A. Caro, E. P. O'Reilly, and O. Marquardt, "Symmetry-adapted calculations of strain and polarization fields in (111)-oriented zinc-blende quantum dots," Phys. Rev. B **84**, 125312 (2011).

[22] L. C. L. Y. Voon and M. Willatzen, eds., "The $\mathbf{k}\cdot\mathbf{p}$ Method" (Springer, 2009).

[23] M. Ehrhardt and T. Koprucki, eds., "Multiband Effective Mass Approximations: Advanced Mathematical Models and Numerical Techniques" (Springer, 2014).

[24] C. A. Broderick, Ph.D. thesis, University College Cork, Ireland (2016).

[25] D. J. Griffiths, "Introduction to Quantum Mechanics (2^{nd} ed.)" (Pearson Prentice Hall, 2004).

[26] J. J. Sakurai, "Modern Quantum Mechanics (Revised ed.)" (Addison Wesley, 1993).

[27] E. P. O'Reilly, "Quantum Theory of Solids" (Taylor and Francis, 2002).

[28] G. L. Bir and G. E. Pikus, "Symmetry and Strain-Induced Effects in Semiconductors" (Wiley, 1974).

[29] L. D. Landau and E. M. Lifshitz, "Theory of Elasticity (3$^{\text{rd}}$ ed.)" (Elsevier, 1986).

[30] M. Povolotskyi, A. A. der Maur, and A. D. Carlo, "Strain effects in freestanding three-dimensional nitride structures," Phys. Status Solidi C **2**, 3891 (2005).

[31] D. Barettin, S. Madsen, B. Lassen, and M. Willatzen, "Comparison of wurtzite atomistic and piezoelectric continuum strain models: implications for the electronic band structure," Phys. Status Solidi C **47**, 134 (2010).

[32] O. Marquardt, S. Boeck, C. Freysoldt, T. Hickel, and J. Neugebauer, "Plane-wave implementation of the real-space **k·p** formalism and continuum elasticity theory," Comp. Phys. Commun. **181**, 765 (2010).

[33] G. Bester, A. Zunger, X. Wu, and D. Vanderbilt, "Effects of linear and nonlinear piezoelectricity on the electronic properties of inas/gaas quantum dots," Phys. Rev. B **74**, 081305 (2006).

[34] G. Bester, X. Wu, D. Vanderbilt, and A. Zunger, "Importance of second-order piezoelectric effects in zinc-blende semiconductors," Phys. Rev. Lett. **96**, 187602 (2006).

[35] S. K. Patra and S. Schulz, "Impact of second-order piezoelectricity on electronic and optical properties of c-plane in x ga1− x n quantum dots: Consequences for long wavelength emitters," Appl. Phys. Lett. **111**, 103103 (2017).

[36] W. Shan, W. Walukiewicz, J. W. A. III, E. E. Haller, J. F. Geisz, D. J. Friedman, J. M. Olson, and S. R. Kurtz, "Band anticrossing in gainnas alloys," Phys. Rev. Lett. **82(6)**, 1221 (1999).

[37] E. P. O'Reilly, A. Lindsay, P. J. Klar, A. Polimeni, and M. Capizzi, "Trends in the electronic structure of dilute nitride alloys," Semicon. Sci. and Tech. **24(3)**, 033001 (2009).

[38] A. Lindsay and E. P. O'Reilly, "Unification of the band anticrossing and cluster-state models of dilute nitride semiconductor alloys," Phys. Rev. Lett. **93(19)**, 196402 (2004).

[39] E. O. Kane, "The **k·p** method," Phys. Rev. **1**, 75 (1967).

[40] T. B. Bahder, "Eight-band **k·p** model of strained zinc-blende crystals," Phys. Rev. B **41**, 11992 (1990).

[41] A. T. Meney, B. Gonul, and E. P. O'Reilly, "Evaluation of various approximations used in the envelope-function method," Phys. Rev. B **50**, 10893 (1994).

[42] C. Y. Chao and S. L. Chuang, "Spin-orbit-coupling effects on the valence-band structure of strained semiconductor quantum wells," Phys. Rev. B. **46**, 4110 (1992).

[43] P.-O. Löwdin, "A note on the quantum mechanical perturbation theory," J. Phys. Chem. **19**, 1396 (1951).

[44] S. Tomić, "Electronic structure of $In_yGa_{1-y}As_{1-x}N_x$/GaAs(N) quantum dots by ten-band **k.p** theory," Phys. Rev. B **73(12))**, 125348 (2006).

[45] F. Szmulowicz, "Derivation of a general expression for the momentum matrix elements within the envelope-function approximation," Phys. Rev. B **51**, 1613 (1995).

[46] S. Bogusevschi, Ph.D. thesis, University College Cork, Ireland (2018).

[47] M. Asada, Y. Miyamoto, and Y. Suematsu, "Theoretical gain of quantum-well wire lasers," Japan. Journ. of Appl. Phys. **24(2A)**, L95 (1985).

[48] A. Krier, ed., "Mid-Infrared Semiconductor Optoelectronics" (Springer, 2006).

[49] A. Bauer, K. Rößner, T. Lehnhardt, M. Kamp, S. Höfling, L. Worschech, and A. Forchel, "Mid-infrared semiconductor heterostructure lasers for gas sensing applications," Semicond. Sci. Technol. **26**, 014032 (2011).

[50] J. Hodgkinson and R. P. Tatam, "Optical gas sensing: a review," Meas. Sci. Technol. **24**, 012004 (2013).

[51] D. Jung, S. Bank, M. L. Lee, and D. Wasserman, "Next-generation mid-infrared sources," J. Opt. **19**, 123001 (2017).

[52] A. N. Baranov and R. Teissier, "Quantum cascade lasers in the InAs/AlSb material system," IEEE Journ. of Selec. Topics in Quant. Elec. **21(6)**, 85 (2015).

[53] Y. Yao, A. J. Hoffman, and C. F. Gmachl, "Mid-infrared quantum cascade lasers," Nature Photonics **6(7)**, 432 (2012).

[54] E. Tournie and L. Cerutti, "Mid-infrared Optoelectronics: Materials, Devices, and Applications" (Woodhead Publishing, 2019).

[55] K. Vizbaras and M.-C. Amann, "3.6 μm GaSb-based type-I lasers with quinternary barriers, operating at room temperature," Electron. Lett. **47**, 980 (2011).

[56] K. Vizbaras and M.-C. Amann, "Room-temperature 3.73 μm GaSb-based type-I quantum-well lasers with quinternary barriers," Semicond. Sci. Technol. **27**, 032001 (2012).

[57] S. D. Sifferman, H. P. Nair, R. Salas, N. T. Sheehan, S. J. Maddox, A. M. Crook, and S. R. Bank, "Highly strained mid-infrared type-I lasers on GaSb," IEEE J. Sel. Topics Quantum Electron. **21**, 1502410 (2015).

[58] L. Shterengas, G. L. Belenky, J. G. Kim, and R. U. Martinelli, "Design of high-power room-temperature continuous-wave GaSb-based type-I quantum-well lasers with $\lambda > 2.5$ μm," Semicond. Sci. Technol. **19**, 655 (2004).

[59] K. O'Brien, S. J. Sweeney, A. R. Adams, B. N. Murdin, A. Salhi, Y. Rouillard, and A. Jouillé, "Recombination processes in mid-infrared InGaAsSb diode lasers emitting at 2.37 μm," Appl. Phys. Lett. **89**, 051104 (2006).

[60] K. S. Gadedjisso-Tossou, S. Belahsene, M. A. Mohou, E. Tournié, and Y. Rouillard, "Recombination channels in 2.4 – 3.2 μm GaInAsSb quantum-well lasers," Semicond. Sci. Technol. **28**, 015015 (2013).

[61] T. D. Eales, I. P. Marko, B. A. Ikyo, A. R. Adams, S. Arafin, S. Sprengel, M.-C.Amann, and S. J. Sweeney, "Wavelength dependence of efficiency limiting mechanisms in type-I mid-infrared GaInAsSb/GaSb lasers," IEEE J. Sel. Topics Quantum Electron. **23**, 1500909 (2017).

[62] A. Bismuto, S. Riedi, B. Hinkov, M. Beck, and J. Faist, "Sb-free quantum cascade lasers in the 3 – 4 μm spectral range," Semicond. Sci. Technol. **27**, 045013 (2012).

[63] E. Tournié and A. N. Baranov, "Mid-infrared semiconductor lasers: a review," Semicond. Semimet. **86**, 183 (2012).

[64] I. Vurgaftman, W. W. Bewley, C. L. Chadwick, C. S. Kim, M. Kim, C. D. Merritt, J. Abell, and J. R. Meyer, "Interband cascade lasers with low threshold powers and high output powers," IEEE J. Sel. Topics Quantum Electron. **19**, 1200210 (2013).

[65] I. Vurgaftman, R. Weih, M. Kamp, J. R. Meyer, C. L. Canedy, C. S. Kim, M. Kim, W. W. Bewley, C. D. Merritt, J. Abell, et al., "Interband cascade lasers," J. Phys. D: Appl. Phys. **48**, 123001 (2015).

[66] M. S. Vitiello, G. Scalari, B. Williams, and P. D. Natale, "Quantum cascade lasers: 20 years of challenges," Opt. Express **23**, 5167 (2015).

[67] M. Razeghi, Q. Y. Lu, N. Bandyopadhyay, W. Zhou, D. Heydari, Y. Bai, and S. Slivken, "Quantum cascade lasers: from tool to product," Opt. Express **23**, 8462 (2015).

[68] Y. P. Varshni, "Temperature dependence of the energy gap of semiconductors," Physica **34**, 149 (1967).

[69] I. Vurgaftman, J. R. Meyer, and L. R. Ram-Mohan, "Band parameters for iii-v compound semiconductors and their alloys," J. Appl. Phys. **89**, 5815 (2001).

[70] J. W. Matthews and A. E. Blakeslee, "Defects in epitaxial multilayers," Journ. of Cryst. Growth **32(2)**, 265 (1976).

[71] R. People and J. C. Bean, "Calculation of critical layer thickness versus lattice mismatch for Ge_xSi_{1-x}/Si strained-layer heterostructures," Appl. Phys. Lett. **47(3)**, 322 (1985).

[72] P. Voisin, "Heterostructures of lattice mismatched semiconductors: fundamental aspects and device perspectives," Proc. SPIE **861**, 88 (1988).

[73] R. Arkani, C. A. Broderick, and E. P. O'Reilly, "Design of 3.3 and 4.2 μm mid-infrared metamorphic quantum well light-emitting diodes," In proceedings of 2018 International Conference on Numerical Simulation of Optoelectronic Devices (NUSOD) pp. 119–120 (2018).

[74] R. Arkani, C. A. Broderick, and E. P. O'Reilly, "Theory and design of type-I In(N)AsSb/AlInAs metamorphic quantum wells for applications in mid-infrared light-emitting diodes," submitted (2019).

[75] E. P. O'Reilly and A. R. Adams, "Band-structure engineering in strained semiconductor lasers," IEEE J. Quantum Electron. **30**, 366 (1994).

[76] A. R. Adams, "Strained-layer quantum well lasers," IEEE J. Sel. Top. Quantum Electron. **17**, 1364 (2011).

[77] D. Ahn and S.-L. Chuang, "Optical gain and gain suppression of quantum-well lasers with valence band mixing," IEEE J. Quantum Electron. **26**, 13 (1990).

[78] C.-S. Chang, S. L. Chuang, J. R. Minch, W. W. Fang, Y. K. Chen, and T. Tanbun-Ek, "Amplified spontaneous emission spectroscopy in strained quantum-well lasers," IEEE J. Sel. Top. Quant. Electron. **1**, 1100 (1995).

[79] J. Hader, J. V. Moloney, and S. W. Koch, "Beyond the ABC: carrier recombination in semiconductor lasers," Proc. SPIE **6115**, 61151T (2006).

[80] A. B. Foreman, "Effective-mass hamiltonian and boundary conditions for the valence bands of semiconductor microstructures," Phys. Rev. B **48**, 4964 (1993).

[81] A. R. Adams, "Band-structure engineering for low-threshold high-efficiency semiconductor lasers," Electron. Lett. **22**, 249 (1986).

[82] E. Yablonovitch and E. O. Kane, "Band structure engineering of semiconductor lasers for optical communications," Phys. Rev. B **6**, 1292 (1988).

[83] M. Silver and E. P. O'Reilly, "Band structure engineering of semiconductor lasers for optical communications," IEEE Jour. of Quant. Elect. **31**, 1193 (1995).

[84] S. Tomić, E. P. O'Reilly, P. J. Klar, H. Gruning, W. Heimbrodt, W. M. Chen, and I. A. Buyanova, "Influence of conduction-band nonparabolicity on electron confinement and effective mass in $GaN_xAs1-x/GaAs$ quantum wells," Phys. Rev. B **69**, 245305 (2004).

[85] M. K. Haigh, G. R. Nash, S. J. Smith, L. Buckle, M. T. Emeny, and T. Ashley, "Mid-infrared $Al_xIn_{1-x}Sb$ light-emitting diodes," Appl. Phys. Lett. **90(23)**, 231116 (2007).

[86] J. A. Barker, R. J. Warburton, and E. P. O'Reilly, "Electron and hole wave functions in self-assembled quantum rings," Phys. Rev. B **69(3)**, 035327 (2004).

[87] J. R. Jarzynka, Ph.D. thesis, Heriot-Watt University, Scotland (2016).

[88] Ph.D. thesis, Heriot-Watt University, Scotland (2012).

[89] S.-H. Wei and A. Zunger, "Calculated natural band offsets of all II–VI and III–V semiconductors: chemical trends and the role of cation *d* orbitals," Appl. Phys. Lett. **72**, 2011 (1998).

[90] G. Liu, C. Shun-Lien, and P. Seoung-Hwan, "Optical gain of strained GaAsSb/GaAs quantum-well lasers: A self-consistent approach," Journ. of Appl. Phys. **88(10)**, 5554 (2000).

[91] Y. S. Chiu, M. H. Ya, W. S. Su, and Y. F. Chen, "Properties of photoluminescence in type-II GaAsSb/GaAs multiple quantum wells," Journ. of Appl. Phys. **92(10)**, 5810 (2002).

[92] Y. Hinuma, A. Grüneis, G. Kresse, and F. Oba, "Band alignment of semiconductors from density-functional theory and many-body perturbation theory," Phys. Rev. B **90**, 155405 (2014).

[93] P. Würfel and U. Würfel, "Physics of solar cells: from basic principles to advanced concepts" (John Wiley & Sons, 2009).

[94] W. Shockley and H. J. Queisser, "Detailed balance limit of efficiency of p-n junction solar cells," J. Appl. Phys. **32**, 510 (1961).

[95] S. Tomić, "Intermediate-band solar cells: Influence of band formation on dynamical processes in InAs/GaAs quantum dot arrays," Phys. Rev. B **82(19)**, 195321 (2010).

[96] A. Luque and A. Martí, "Increasing the efficiency of ideal solar cells by photon induced transitions at intermediate levels," Phys. Rev. Lett. **78**, 5014 (1997).

[97] Y. Okada, N. J. Ekins-Daukes, T. Kita, R. Tamaki, M. Yoshida, A. Pusch, O. Hess, C. C. Phillips, D. J. Farrell, K. Yoshida, et al., "Intermediate band solar cells: recent progress and future directions," Appl. Phys. Rev. **2**, 021302 (2015).

[98] A. Luque, A. Martí, and C. Stanley, "Understanding intermediate-band solar cells," Nat. Photon. **6(3)**, 146 (2012).

[99] I. Ramiro, A. Martí, E. Antolín, and A. Luque, "Review of experimental results related to the operation of intermediate band solar cells," IEEE Journ. of Photovol. **4(2)**, 736 (2014).

[100] Y. Okada, N. J. Ekins-Daukes, T. Kita, R. Tamaki, M. Yoshida, A. Pusch, O. Hess, C. C. Philips, D. J. Farrell, K. Yoshida, et al., "Intermediate band solar cells: recent progress and future directions," Appl. Phys. Rev. **2**, 021302 (2015).

[101] A. Luque and A. Martí, "The intermediate band solar cell: progress towards the realization of an attractive concept," Adv. Mater. **22**, 160 (2010).

[102] I. Ramiro, J. Villa, C. Tablero, E. Antolín, A. Luque, A. Martí, J. Hwang, J. Philips, A. J. Martin, and J. Millunchick, "Analysis of the intermediate-band absorption properties of type-ii gasb/gaas quantum-dot photovoltaics," Phys. Rev. B **96(12)**, 125422 (2017).

[103] A. Martí, E. Antolín, P. G. Linares, I. Ramiro, I. Artacho, E. López, E. Hernández, M. J. Mendes, A. Mellor, I. Tobías, et al., "Six not-so-easy pieces in intermediate band solar cell research," J. Photonics Energy **3**, 031299 (2013).

[104] R. Kudrawiec, A. V. Luce, M. Gladysiewicz, M. Ting, Y. J. Kuang, C. W. Tu, O. D. Dubon, K. M. Yu, and W. Walukiewicz, "Electronic band structure of $GaN_xP_yAs_{1-x-y}$ highly mismatched alloys: suitability for intermediate-band solar cells," Phys. Rev. Applied **1**, 034007 (2014).

[105] I. Ramiro, J. Villa, P. Lam, S. Hatch, J. Wu, E. López, E. Antolín, H. Liu, A. Martí, and A. Luque, "Wide-bandgap InAs/InGaP quantum-dot intermediate band solar cells," IEEE J. Photovolt. **5**, 840 (2015).

[106] A. M. Kechiantz, L. M. Kocharyan, and H. M. Kechiyants, "Band alignment and conversion efficiency in Si/Ge type-II quantum dot intermediate band solar cells," Nanotechnology **18**, 405401 (2007).

[107] T. Tayagaki, N. Usami, W. Pan, Y. Hoshi, K. Ooi, and Y. Kanemitsu, "Enhanced carrier extraction from Ge quantum dots in Si solar cells under strong photoexcitation," Appl. Phys. Lett. **101**, 133905 (2012).

[108] A. Kechiantz, A. Afanasev, and S. L. Lazzari, "Impact of spatial separation of type-II GaSb quantum dots from the depletion region on the conversion efficiency limit of GaAs solar cells," Prog. Photovoltaics **23**, 1003 (2015).

[109] T. Takeshi and T.Sugaya, "Type-II InP quantum dots in wide-bandgap InGaP host for intermediate-band solar cells," Appl. Phys. Lett. **108**, 153901 (2016).

[110] L. Cuadra, A. Martí, and A. Luque, "Type II broken band heterostructure quantum dot to obtain a material for the intermediate band solar cell," Physica E **14**, 162 (2002).

[111] K. Nishikawa, Y. Takeda, T. Motohiro, D. Stao, J. Ota, N. Miyashita, and Y. Okada, "Extremely long carrier lifetime over 200 ns in GaAs wall-inserted type II InAs quantum dots," Appl. Phys. Lett. **100**, 113105 (2012).

[112] S. Tomić, A. Martí, E. Antolín, and A. Luque, "On inhibiting Auger intraband relaxation in InAs/GaAs quantum dot intermediate band solar cells," Appl. Phys. Lett. **99**, 053504 (2011).

[113] S. Tomić, "Effect of Sb induced type II alignment on dynamical processes in InAs/GaAs/-GaAsSb quantum dots: implication to solar cell design," Appl. Phys. Lett. **103**, 072112 (2013).

[114] M. C. Wagener, P. J. Carrington, J. R. Botha, and A. Krier, "Evaluation of the two-photon absorption characteristics of GaSb/GaAs quantum rings," J. Appl. Phys. **116**, 044304 (2014).

[115] Y. Shoji, R. Tamaki, and Y. Okada, "Multi-stacked GaSb/GaAs type-II quantum nanostructures for application to intermediate band solar cells," AIP Adv. **7**, 065305 (2017).

[116] J. Hwang, A. J. Martin, J. M. Millunchick, and J. D. Phillips, "Thermal emission in type-II GaSb/GaAs quantum dots and prospects," J. Appl. Phys. **111**, 074514 (2012).

[117] C.-P. Tsai, S.-C. Hsu, S.-Y. Lin, C.-W. Chang, L.-W. Tu, K.-C. Chen, T.-S. Lay, and C.-C. Lin, "Type-II GaSb quantum ring solar cells under concentrated sunlight," Opt. Express **22**, A359 (2014).

[118] H. Fujita, P. J. Carrington, M. C. Wagener, J. R. Botha, A. R. J. Marshall, J. S. James, A. Krier, K. Lee, and N. J. Ekins-Daukes, "Open-circuit voltage recovery in type-II GaSb/GaAs quantum ring solar cells under high concentration," Prog. Photovoltaics **23**, 1896 (2015).

[119] D. Montesdeoca, P. J. Carrington, I. P. Marko, M. C. Wagener, S. J. Sweeney, and A. Krier, "Open circuit voltage increase of gasb/gaas quantum ring solar cells under high hydrostatic pressure," Sol. Energy Mater. Sol. Cells **187**, 227 (2018).

[120] A. A. Khan, M. Herrera, N. Fernandez-Delgado, D. Montesdeoca, P. J. Carrington, H. Fujita, J. S. James, M. Wagener, R. Botha, A. J. Marshall, et al., "Structural analysis of GaSb/GaAs quantum rings for solar cells," Proc. European Microscopy Congress (2016).

[121] R. Arkani, C. A. Broderick, and E. P. O'Reilly, "Band structure engineering of type-II GaSb/GaAs quantum rings for intermediate band solar cells," Proc. 19$^{\text{th}}$ International Conference on Numerical Simulation of Optoelectronic Devices (NUSOD) (2019).

[122] A. D. Andreev, J. R. Downes, A. D. Faux, and E. P. O'Reilly, "Strain distributions in quantum dots of arbitrary shape," J. of Appl. Phys. **86(1)**, 297 (1999).

[123] M. C. Wagener, P. J. Carrington, J. R. Botha, and A. Krier, "Photocapacitance study of type-II GaSb/GaAs quantum ring solar cells," J. Appl. Phys. **115**, 014302 (2014).

[124] R. Timm, A. Lenz, H. Eisele, L. Ivanova, M. Dähne, G. Balakrishnan, D. L. Huffaker, I. Farrer, and D. A. Ritchie, "Quantum ring formation and antimony segregation in GaSb/GaAs nanostructures," J. Vac. Sci. Technol. B **26**, 1492 (2008).

[125] P. J. Carrington, A. S. Mahajumia, M. C. Wagener, J. R. Botha, Q. Zhuang, and A. Krier, "Type II GaSb/GaAs quantum dot/ring stacks with extended photoresponse for efficient solar cells," Physica B **407**, 1493 (2012).

[126] M. Felici, G. Pettinari, F. Biccari, M. Capizzi, and A. Polimeni, "Spatially selective hydrogen irradiation of dilute nitride semiconductors: a brief review," Semicon. Sci. and Tech. **33(5)**, 053001 (2018).

[127] G. C. (Ed.), ed., "Hydrogenated Dilute Nitride Semiconductors: Theory, Properties, and Applications" (CRC Press, 2017).

[128] J. I. Pankove and N. M. Johnson, "Introduction to hydrogen in semiconductors. in semiconductors and semimetals," Elsevier **34**, 1 (1991).

[129] J. Chevallier, W. C. Dautremont-Smith, C. W. Tu, and S. J. Pearton, "Donor neutralization in gaas (si) by atomic hydrogen," Appl. Phys. Lett. **47(2)**, 108 (1985).

[130] I. Buyanova and W. C. (Eds.), eds., "Physics and applications of dilute nitrides" (CRC Press, 2004).

[131] S. Younis, Ph.D. thesis, Sapienza University of Rome, Italy (2019).

[132] J. Misiewicz, P. Sitarek, K. Ryczko, R. Kudrawiec, M. Fischer, M. Reinhardt, and A. Forchel, "Influence of nitrogen on carrier localization in InGaAsN/GaAs single quantum wells," Microelectron. Journ. **34(5-8)**, 737 (2003).

[133] M. P. C. M. Krijn, "Heterojunction band offsets and effective masses in III-V quaternary alloys," Semicond. Sci. Technol. **6**, 27 (1991).

[134] P. T. Webster, N. A. Riordan, S. Liu, E. H. Steenbergen, R. A. Synowicki, Y.-H. Zhang, and S. R. Johnson, "Measurement of InAsSb bandgap energy and InAs/InAsSb band edge positions using spectroscopic ellipsometry and photoluminescence spectroscopy," J. Appl. Phys. **118**, 245706 (2016).

[135] C. G. Van de Walle, "Band lineups and deformation potentials in the model solid theory," Phys. Rev. B **39**, 1871 (1989).